Title

Multi-Scale Optical Metrology of Biomaterials and Nanomaterials for Medical and Industrial Applications

Author

Reiber Kyle, Jennifer Lynn

Publication Date

2012

UNIVERSITY OF CALIFORNIA
RIVERSIDE

Multi-Scale Optical Metrology of Biomaterials and Nanomaterials for Medical and Industrial Applications

A Dissertation submitted in partial satisfaction
of the requirements for the degree of

Doctor of Philosophy

in

Electrical Engineering

by

Jennifer Lynn Reiber Kyle

March 2012

Dissertation Committee:
Dr. Mihrimah Ozkan, Chairperson
Dr. Cengiz Ozkan
Dr. Kambiz Vafai

The Dissertation of Jennifer Lynn Reiber Kyle is approved:

Committee Chairperson

University of California, Riverside

Acknowledgements

I would like to acknowledge Dr. Ravi Raghavan and Dr. Michael Kyle at Loma Linda University Medical Center for help in tissue processing and interpretation of images collected from tissue samples. I would also like to acknowledge Dr. David Carter at the Center for Plant and Cell Biology (CEPCEB) at the University of California, Riverside for help designing and performing fluorescence imaging experiments.

The text of this dissertation, in part, is a reprint of the material as is appears in “Centimeter-Scale High-Resolution Metrology of Entire CVD-Grown Graphene Sheets”, (*Small* 2011, 7, 18, 2599-2606) and the pre-peer reviewed version of “Analysis of Light Scattering from Human Breast Tissue Using a Custom Dual-Optical Scanning Near-Field Optical Microscope” (*Journal of Biophotonics* 2011, 4, 3, 193-205). The co-authors (Mihrimah Ozkan and Cengiz Ozkan) listed in these publication directed and supervised the research which forms the basis for this dissertation. Ali Guvenc assisted with developing image processing algorithms while Wei Wang, Maziar Ghazinejad, Jian Lin, and Shirui Guo assisted with growth and processing of the graphene samples. Michael Kyle assisted with tissue preparation and tissue image interpretation, while Ravi Raghavan assisted with tissue image interpretation, and Gurer Budak provided expertise.

Dedication

This work is dedicated to all the great scientists who inspired me to ask questions and seek answers, the people in this world who inspired me to work hard to make a positive impact on our world, and, most importantly, to my family and friends who supported me emotionally, intellectually, and financially during this time. I have truly “stood on the shoulders of giants” and am forever grateful and humbled.

ABSTRACT OF THE DISSERTATION

Multi-Scale Optical Metrology of Biomaterials and Nanomaterials for Medical and Industrial Applications

by

Jennifer Lynn Reiber Kyle

Doctor of Philosophy, Graduate Program in Electrical Engineering
University of California, Riverside, March 2012
Dr. Mihrimah Ozkan, Chairperson

Nanotechnology is a promising field that is focused on working at the atomic and nanoscale. Many helpful materials and imaging techniques have been developed in nanotechnology. Graphene, a nanomaterial consisting of a single atomic layer of carbon atoms arranged in a hexagonal lattice, exhibits excellent optical, electrical, and thermal properties and has many applications in the semiconductor, energy, and thermal management industries. Additionally, iron oxide nanoparticles are excellent candidates for drug delivery and labeling applications in medicine due to their high biocompatibility and customizable size and surface chemistry. Near-field microscopy is a nanoscale imaging technique with the capability of providing the label-free tissue diagnostics medical field with information about the intrinsic optical properties of tissue that cannot be probed by any other techniques. Despite the benefits that near-field microscopy offers for medicine, its use in imaging biomaterials has been limited due to the large topographic variations that these samples exhibit. This gap between the nanoscale and the scales of interest for industry and medicine also presents an obstacle in the application of iron oxide nanoparticles in medicine and graphene in industry. In this work, I develop multi-scale optical metrology techniques for characterizing graphene at the industrial scale, identifying unlabeled nanoparticles within cultured human cells, and studying the intrinsic optical properties of tissue with near-field microscopy. Through fluorescence quenching microscopy (FQM), I map the layer thickness and uniformity of entire centimeter-scale graphene sheets and identify fluorine-doped regions. I utilize scanning near-field optical microscopy (SNOM) to identify iron oxide nanoparticles in cultured human cells through their scattering behavior, and I develop SNOM for label-free tissue diagnostics, quantifying image creation in SNOM of large biological samples and then revealing the cause of scattering dependence on the hydration state of fixed human breast tissue. This work contributes knowledge to the graphene growth, nanoparticle design, and label-free tissue diagnostics fields and facilitates the integration of nanotechnology with medicine and industry.

Table of Contents

List of Figures

List of Tables

Abbreviations

AFM – Atomic Force Microscopy

CMOS – Complementary Metal Oxide Semiconductor

CVD – Chemical Vapor Deposition

DI – Deionized

DCM – 4(Dicyanomethylene)-2-methyl-6-(4-dimethylaminostyryl)-4H-pyran

FQM – Fluorescence Quenching Microscopy

FRET – Förster Resonant Energy Transfer

FSA – Frozen Section Analysis

FTIR – Fourier Transform Infrared

FWHM – Full-Width Half-Maximum

H&E – Hematoxylin and Eosin

IPA – Isopropyl Acetate

PMMA – Poly(methyl methacrylate)

rGO – Reduced Graphene Oxide

RIE – Reactive Ion Etching

SEM – Scanning Electron Microscopy

SNOM – Scanning Near-Field Optical Microscopy

STM – Scanning Tunneling Microscopy

STS – Scanning Tunneling Spectroscopy

TEM – Transmission Electron Microscopy

XPS – X-ray Photoemission Spectroscopy

XTEM – Cross-Section Transmission Electron Microscopy

1 Introduction

Nanotechnology is an exciting new field with the potential to revolutionize industry and medicine. The power of nanotechnology is its ability to build nanomaterials from the ground up, engineering them for specific applications. A two-dimensional nanomaterial which is particularly promising for industry is graphene. Graphene is a single sheet of sp^2-hybridized carbon atoms arranged in a hexagonal lattice structure. Due to its unique structure, graphene exhibits electrical, optical, and thermal properties which make it an ideal material for semiconductor, energy, and thermal industries. In the medical field, nanotechnology is improving the disease detection and treatment process through novel nanomaterials and nanoscale imaging techniques. For nanomedicine, nanoparticles are being developed to selectively attach to cell membranes, serving as disease detection labels, or deliver embedded drugs to the interior of target cells by crossing the cell membrane. The ability to design nanoparticles from the ground up allows precise engineering of their properties, such as size, shape, and surface functionalization, for efficient uptake, high selectivity, and biocompatibility. In addition to developing new detection labels, nanotechnology introduces new nanoscale imaging techniques that can improve diagnostics by increasing our understanding of the optical properties of tissue. Label-free tissue diagnostics is a promising new medical field concerned with achieving disease detection through the intrinsic optical properties of tissue, forgoing the need for histological stains and greatly increasing the speed and efficacy of disease detection while reducing cost. However, label-free tissue diagnostics requires detailed knowledge about the intrinsic optical properties of tissue, which is difficult to obtain through conventional imaging techniques. Near-field optical imaging, a nanoscale imaging technique, exhibits improved optical resolution over conventional imaging, high sensitivity to scattering, and simultaneous optical and topography image collection. These capabilities make near-field optical imaging a promising technique for label-free tissue diagnostics. Despite the great potential of nanotechnology, the fundamental obstacle that complicates its use in medicine and industry is the incredibly small scale in which nanotechnology operates. Nanomaterials are generally 1-100 nanometers, much smaller than the scale of biomaterials, such as tissue and cells, which are measured in micron- to millimeters. Furthermore, nanomaterials are too small to be resolved by standard optical techniques, which have a diffraction resolution limit of ~0.5 micrometers. On the other hand, nanoscale imaging techniques are sensitive to sample size, making imaging of biomaterials nontrivial. This research bridges this gap in scales through multi-scale optical metrology of nanomaterials and biomaterials to provide significant contributions to the fields of industrial graphene metrology, nanomedicine, and label-free tissue diagnostics.

In this research, we use two optical characterization techniques to bridge the gap between nanotechnology and medicine and industry, scanning near-field optical microscopy (SNOM) and fluorescence quenching microscopy (FQM). SNOM is a new tool for optical microscopy that breaks the diffraction barrier that limits the resolution of far-field imaging techniques by retaining the high-resolution evanescent information that exists only very near to the sample. When near-field (evanescent) light is scattered by the sample, it is transformed into propagating far-field light.[1,2] By retaining the information in the near-field light, SNOM achieves an optical imaging resolution that is up to 5 times greater than achievable with far-field microscopy. Furthermore, SNOM's dependence on scattering to transform near-field to far-field light makes it highly sensitive to scattering within the sample. In addition to offering high-resolution optical imaging and being sensitive to scattering, SNOM combines topography measurements with optical measurements. Therefore it is the ideal nanoscale optical metrology technique for nanomedicine applications such as studying the interaction between nanoparticles and cells and revealing the intrinsic optical properties of unlabeled tissue. FQM, on the other hand, is a far-field optical technique that exploits the near-field phenomena of fluorescence quenching to enable large-scale visualization of graphene. Fluorescence quenching is detected by spin-coating a solution of polymer mixed with fluorescent dye onto the graphene then viewing the sample under a fluorescence microscope. FQM offers improvements over alternative graphene imaging techniques such as atomic force microscopy, Raman spectroscopy, transmission electron microscopy, and optical reflection and transmission techniques because it can be performed on arbitrary substrates, imaging time is short, large areas can be measured, and the imaging equipment (a fluorescent microscope) is widely available.

The versatility of SNOM and FQM introduces the possibility of multi-scale optical metrology, which we fully utilize in this dissertation research. In Chapter 2, we introduce optical imaging mechanisms, summarizing the theory behind the SNOM and FQM techniques. In Chapter 3, we develop a technique for metrology of graphene utilizing

FQM. We first develop a technique for identifying graphene layers on entire large-area CVD graphene samples. Next, we extend this technique to visualization of chemical doping of graphene. In Chapter 4, we demonstrate SNOM transmission measurements of cells and develop a method for detecting iron oxide nanoparticles in cells based on the scattering profile. In Chapter 5, we develop dual-optical SNOM, which simultaneously collects SNOM reflection and SNOM transmission images, and utilize it to study scattering from unlabeled human tissue. In this study, we investigate the cause of scattering variation between non-desiccated and desiccated fixed tissue. To improve dual-optical SNOM from a characterization technique to a metrology technique, we utilize modeling, theory, and experiments to quantify image formation in reflection SNOM to allow prediction of topology-induced artifacts which complicate reflection SNOM image interpretation.

In this dissertation research, we further graphene development for industry by creating the first industrial metrology technique for measuring graphene layer thickness, uniformity, and chemical doping. Additionally, we contribute to the nanomedicine, label-free tissue diagnostics, and SNOM fields by extending the capability of SNOM to imaging cells and tissue, developing a technique for identifying unlabeled nanoparticles in cells, and revealing the effect of dehydration on the optical properties of unlabeled tissue.

2 Optical Imaging Mechanisms

2.1 Light Interaction with Materials

Light interacts with any material through absorption/emission of photons (light as a particle) or scattering of the electromagnetic wave (light as a wave). Absorption occurs when the incident light has an energy that matches a possible electronic transition within the material and a photon is annihilated to promote the energy state of an electron. Similarly, emission is the creation of a photon by the transition of an electron in the material to a lower energy state. Scattering, on the other hand, occurs with light at any energy. Scattering is due to the electric field of the incident light inducing an oscillation of the electronic charges in the material (electrons in the case of individual atoms), which in turn causes these charges to emit radiation in the form of scattered light.

When a molecule absorbs a photon, it is excited from the ground state to an excited state. Energetically favored electron promotion is from the highest occupied molecular orbital (HOMO), usually the singlet ground state, S_0, to the lowest unoccupied molecular orbital (LUMO), and the resulting species is called the singlet excited state S_1. The longest wavelength absorption band corresponds to the energy difference between these two states, given by the following expression:

$$\Delta E = E_{\mathrm{LUMO}} - E_{\mathrm{HOMO}} = \frac{h^2}{8mL^2}\left(n_{\mathrm{LUMO}}^2 - n_{\mathrm{HOMO}}^2\right) \tag{1}$$

The energy required for this electronic transition can be supplied by a photon of the appropriate frequency, given by the Planck relationship:

$$E = hv = hc/\lambda \tag{2}$$

where h is Planck's constant, n is the frequency, c is the speed of light, and λ is the wavelength.[3] After absorbing a photon, the molecule eventually returns to the ground state either by emitting another photon through photoluminescence or through non-radiative decay, such as internal conversion to heat. Photoluminescence occurs through fluorescence or phosphorescence. The Jablonski diagram in Figure 1 shows the energy transfer process for photon absorption and photoluminescence. As indicated in Figure 1, absorption usually excites electrons to higher vibrational energy levels (1, 2, etc.) of the singlet excited electronic energy states (S_1, S_2). These electrons generally relax to the lowest vibrational level of the first singlet excited state within picoseconds. Fluorescence emission, the transition from the singlet excited state to the ground state, occurs within tens of nanoseconds, after internal conversion. Therefore, a photon emitted through fluorescence has a longer wavelength than the absorbed photon. Photoemission also occurs at a longer wavelength, but takes place from the first triplet excited state, T_1. Transition from the first triplet excited state to the singlet ground state is forbidden; therefore lifetimes for photoemission are several orders of magnitude greater than those for fluorescence, making fluorescence and non-radiative de-excitation pathways more favorable.[3,4]

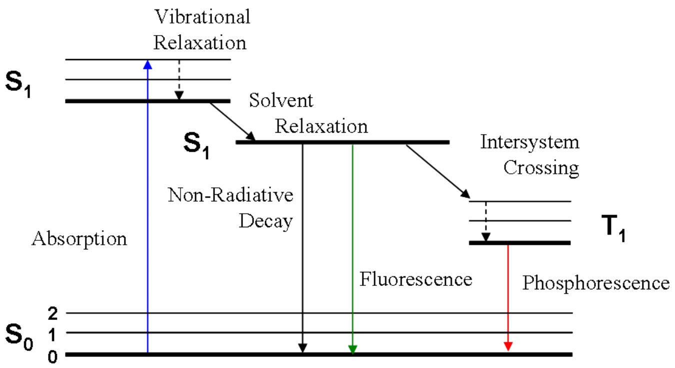

Figure 1 Jablonski diagram for photon absorption and photoluminescence showing fluorescence and phosphorescence.

The scattering of light, as a result of its interaction with matter, can be classified as elastic or inelastic. In elastic scattering, the photon propagation direction is changed but its energy is conserved. On the other hand, inelastic scattering occurs when both the photon propagation direction and energy is altered. Inelastic scattering is caused by the transfer of energy between the photon and a molecular bond and produces a scattered spectrum. Elastic scattering is divided into three domains based on the size of the particle relative to the wavelength of incident light. These three domains are Rayleigh scattering (particle is much smaller than the wavelength), Mie scattering (particle is about the same size as the wavelength), and Geometric scattering (particle is much larger than the wavelength). Inelastic scattering is also divided into domains, based on the types of molecule motions involved, vibrational and rotational (Raman scattering) or translational (Brillouin scattering). Brillouin scattering produces very small frequency shifts and has not yet yielded important applications.[5] The Jablonski diagram for Rayleigh and Raman scattering in Figure 2 shows the source of the wavelength shift observed in Raman spectroscopy is the molecules not returning to their original vibrational state after being excited by incident photons. These molecules either return to a higher vibrational state, which results in Stokes Raman scattering, or they return to a lower state, which results in Anti-Stokes Raman scattering. The intensity of Stokes Raman scattering, where energy is lost by the photon, is much less than Rayleigh scattering, while the intensity of Anti-Stokes Raman scattering, where energy is gained by the photon, is even less than Stokes Raman scattering.[5] The attenuated Anti-Stokes Raman scattering is due to the population state of molecules being principally in their ground vibrational state at room temperature, while Anti-Stokes Raman scattering requires that the molecules start in a higher vibrational state.

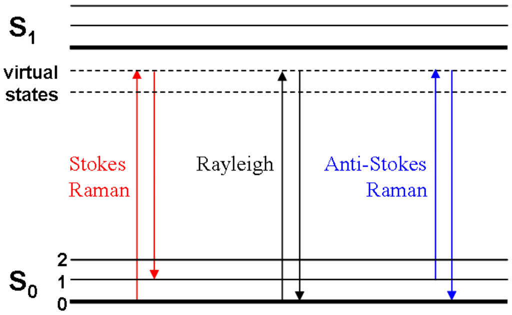

Figure 2 Jablonski diagram for Raman and Rayleigh light scattering.

In this work, we focus on two interaction mechanisms between light and matter, fluorescence and elastic scattering of light. Fluorescence, and its quenching through non-radiative decay, is the basis of fluorescence quenching microscopy and elastic scattering is the basis of scanning near-field optical microscopy. Both of these imaging techniques are described in detail in the following sections. Because elastic scattering is the dominant scattering mechanism, generally the term 'scattering' refers to elastic scattering. This dissertation will follow this convention, substituting 'scattering' for elastic scattering and using the term ‘inelastic scattering’ to differentiate the two scattering mechanisms.

2.2 Fluorescence Quenching Microscopy

2.2.1 Fluorescence Emission

Fluorophores are molecules that absorb light at a specific wavelength, re-emit light at a longer specific wavelength, and primarily de-exite through fluorescence radiation. The intensity and wavelength of the emitted light depend on both the fluorophore and the chemical environment. The two primary properties that describe steady-state and transient fluorescence by a fluorophore are quantum yield and fluorescence lifetime, respectively. These properties are based on the dynamics of de-excitation of the fluorophore.

For an initial concentration of excited state fluorophores [$A*$], the fluorophores return to the ground state through fluorescence according to

$$A^{*} \xrightarrow{k_f} A + hv \tag{3}$$

and through non-radiative decay according to

$$A^{*} \xrightarrow{k_{nr}} A \tag{4}$$

where k_f and k_{nr} are the fluorescence and non-radiative decay rate constants, respectively. The rate equation for de-excitation is

$$\frac{d[A^*]}{dt} = -\left(k_f + k_{nr}\right)[A^*]. \tag{5}$$

Integrating the rate equation gives the concentration of excited fluorophores,

$$[A^*] = [A^*]_0 e^{-\left(k_f + k_{nr}\right)/t}, \tag{6}$$

where t is time and $[A*]_0$ is the initial excited-state fluorophore concentration at t = 0. The fluorescence lifetime is a measure of the time required for the fluorescence intensity to decay to 1/e of its initial value and is given by

$$\tau = 1/\left(k_f + k_{nr}\right). \tag{7}$$

The fluorescence intensity observed for a fluorophore is proportional to its concentration in the excited state. Therefore, the fluorescence emitted by an excited fluorophore is described by

$$F(t) = F_0 e^{-t/\tau} \tag{8}$$

where t is time and F_0 is the initial fluorescence intensity at $t = 0$.

Quantum yield (Q) determines the fluorescence emission efficiency of the fluorophore and is the ratio of the emissive rate of the fluorophore (k_f) to the rate of non-radiative decay (k_{nr}).[4] In terms of decay rates, Q is given by:

$$Q = \frac{k_f}{k_f + \mathrm{k_{nr}}} \tag{9}$$

The lifetime of a fluorophore in the absence of non-radiative processes (intrinsic lifetime) is given by

$$\tau_n = \frac{1}{k_f} \tag{10}$$

and is related to the quantum yield and the fluorescence lifetime by

$$\tau_n = \frac{\tau}{\mathrm{Q}} \tag{11}$$

2.2.2 Quenching Mechanisms

Fluorescence quenching is caused by non-radiative energy transfer between the fluorophore (donor) and an energy acceptor, which decreases the fluorescence intensity. There are two types of non-radiative energy transfer: static and dynamic. Static fluorescence quenching is caused by the donor binding to the fluorophore, which creates a ground state complex that has a different absorption spectrum or is non-fluorescent. Static fluorescence quenching occurs when both the donor and acceptor molecules are in the ground state and does not does not affect fluorescence lifetime measurements since the only fluorescence that is observable comes from the unquenched, uncomplex fluorophores.

Dynamic fluorescence quenching is caused by additional non-radiative de-excitation processes for the fluorophore. In the general case, the fluorescence lifetime of a fluorophore depends on the decay rates of all possible decay pathways and is given by

$$\frac{1}{\tau} = \sum_i k_i. \qquad (12)$$

When non-radiative transfer mechanisms are introduced to the system, the lifetime of the fluorophore is decreased and the fluorescence radiation is effectively quenched. The two primary non-radiative energy transfer mechanisms between a donor in the excited state and an accepter are Förster resonant energy transfer (FRET) and Dexter electron transfer (also called exchange or collisional energy transfer). In both of these processes, the energy is transferred to the acceptor from the donor in its excited state before a photon is emitted. These processes are illustrated in the Jablonski diagram in Figure 3 and are described below.

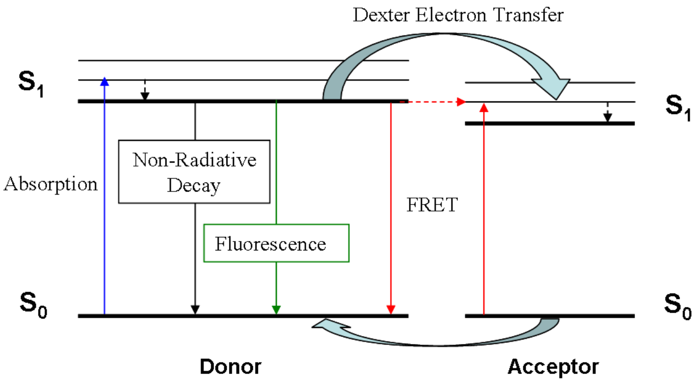

Figure 3 Jablonski diagram showing Dexter electron transfer and FRET.

2.2.2.1 Dexter Electron Transfer

Dexter electron transfer occurs when the donor and acceptors come into molecular contact and their electron wave-functions overlap, allowing electron exchange.[6] The Dexter electron transfer rate constant k_{ET} is given by

$$k_{ET} \propto J e^{[-2r/L]} \tag{13}$$

where r is the distance between the donor and acceptor, L is the sum of the van-der Waals radii of the donor and acceptor, and $J = \int q_{d,\lambda} \varepsilon_{a,\lambda} \lambda^4 d\lambda$ is the spectral overlap integral. This transfer rate has an e^{-r} dependence on the distance between the donor and acceptor. Because electron transfer requires an overlap of the electron clouds, it only occurs at short distances, typically 15-20Å.[4]

The decrease in fluorescence intensity due to Dexter electron transfer is described by the Stern-Volmer equation:

$$\frac{F_0}{F} = 1 + K[Q] = 1 + k_q \tau_n [Q]. \tag{14}$$

Here, K is the Stern-Volmer quenching constant, k_q is the bimolecular quenching constant, τ_n is the intrinsic lifetime of the fluorophore, and $[Q]$ is the quencher concentration. The Stern-Volmer quenching constant indicates the sensitivity of the fluorophore to a quencher. K depends strongly on the diffusion rate. Therefore, it is small for a fluorophore buried in a macromolecule and large for a fluorophore that is free in solution or on the surface of a biomolecule. Because electron transfer is facilitated by diffusion, fluorescence quenching caused by electron transfer depends on temperature, increasing in effectiveness at higher temperatures.[4]

2.2.2.2 Förster Resonant Energy Transfer

FRET is a long-distance quenching mechanism, occurring when the emission spectrum of the fluorophore (donor) overlaps the absorption spectrum of the acceptor. Unlike Dexter electron transfer, FRET does not require molecular contact between the donor and acceptor and therefore is not sensitive to the electrostatic interaction between the molecules.[7] In FRET, the donor and acceptor are coupled through a dipole-dipole interaction. FRET efficiency is based on three factors: (1) distance between the donor and the acceptor, (2) spectral overlap of the donor emission and the acceptor absorption spectra, and (3) relative orientation of the donor emission dipole moment and the acceptor absorption dipole moment.[3,4,7] The FRET rate between two molecules is given by[4]

$$k_T = \frac{1}{\tau_n}\left(\frac{R_0}{d}\right)^6 \tag{15}$$

where R_0 is the Förster distance, d is the distance between the donor and acceptor, and τ_n is the intrinsic lifetime of the donor. The Förster distance is given (in nm) by

$$\mathrm{R_0} = (\mathrm{c_0}\kappa^2\mathrm{J}\mathrm{n}^{-4}Q_0)^{1/6} \tag{16}$$

where $c_0 = 8.8 \times 10^{-11}$ is a constant, κ_2 is the dipole relative orientation factor, $J(\lambda) = \int q_{d,\lambda}\varepsilon_{a,\lambda}\lambda^4 d\lambda$ ($\mathrm{M^{-1}\ cm^{-1}\ nm^4}$) is the overlap integral for the donor emission spectrum and the acceptor absorption spectrum, λ is the wavelength in nm, n is the refractive index of the surrounding medium, and Q_0 is the intrinsic quantum yield of the donor.[3,4,8]

FRET is sensitive to the relative orientation between the donor emission dipole and the acceptor absorption dipole. The dependence of FRET on relative dipole orientation is represented by the dipole relative orientation factor κ^2, which varies from 0 to 4. When the donor and acceptor dipoles are perpendicular $\kappa^2=0$, while $\kappa^2=1$ for side-by-side parallel dipoles and $\kappa^2=4$ for head-to-tail parallel dipoles. For extended systems, where the ensemble average can be used and dipoles orientations are random, $\kappa^2=2/3$ is used for dipoles with fast rotational diffusion[7] and $\kappa^2=0.476$ is used for dipoles with static orientations.[4,7] Determining the actual value of κ^2 for any system is a complex problem where many factors must be considered.[3,9]

The distance dependence of FRET depends on the dimensionality of the acceptor. For an N-dimensional acceptor, FRET dependence is d^{N-6}, where d denotes distance.[10] In classical FRET, the acceptor is a 0-dimensional dipole, which leads to the classical d^{-6} distance dependence. Graphene is a 2-dimensional material, which results in d^{-4} distance dependence.[11–14] This relationship holds true for nanowires (1-dimensional with d^{-5} distance dependence)[14,15] and half-space materials (3-dimensional, with d^{-3} distance dependence).[16]

The intrinsic quantum yield is related to the fluorescence decay rate by

$$Q_0 = k_f \tau_n. \tag{17}$$

Therefore, the relationship between the FRET rate and the fluorescence rate is given by

$$\frac{k_T}{k_f} = \frac{c_0 \kappa^2 J n^{-4}}{d^{\mathrm{N}-6}}. \tag{18}$$

The FRET efficiency E is defined as the fraction of excited molecules that undergo energy transfer from the donor to the acceptor and is expressed in terms of the rate constants as

$$E_{FRET} = \frac{k_T}{k_T + k_f} \tag{19}$$

and in terms of the distance between the donor and acceptor as[4,7,13]

$$E_{FRET} = \frac{{R_0}^6}{{R_0}^6 + d^{\mathrm{N}-6}}. \tag{20}$$

2.3 Scanning Near Field Optical Microscopy

SNOM is based on the concept of positioning a light source with dimensions much smaller than the wavelength of light close to the sample, producing a subwavelength illumination spot on the sample. The image that is produced by scanning this illumination spot along the sample surface and recording the transmitted or reflected light exhibits optical resolution greater than allowed by the diffraction limit. This concept was first proposed in 1928 by E.H. Synge.[17] However, due to the technical difficulty of maintaining a distance between the source and sample that is smaller than the light wavelength, the first experimental application wasn't reported until 1972, when Ash and Nicholls demonstrated the realization of Synge's concept in the microwave range.[18] The first experimental realizations in the visible range, reported in 1984 by Lewis et al.[19] and Pohl et al.,[20] were made possible by the development of Scanning Tunneling Microscopy (STM). Today, most SNOM setups use Atomic Force Microscopy (AFM) to maintain the source-sample distance.

2.3.1 Near-Field Regime

SNOM breaks the diffraction barrier by detecting the evanescent waves that are lost in far-field optical techniques. Evanescent waves are produced when light is confined to a sub-wavelength dimension. When scattered, these evanescent waves are converted to propagating waves which can be detected in the far-field. Evanescent waves can be produced by a SNOM tip and scattered by the sample surface or they can be produced by the sample and scattered by the tip.[2] Evanescent waves are defined by the near-field regime of the optical field.

The near-field regime can best be explained using angular spectrum representation of the optical field. Angular spectrum representation is the series expansion of an arbitrary field in terms of plane and evanescent waves with variable amplitudes and spatial frequencies (k vectors). The angular spectrum representation of an electric field, E_s, at a plane transverse to the z-axis a distance $z=z_0$ from the origin plane is given by[21,22]

$$E_s(x,y;z_0) = \int_{-\infty}^{\infty}\int_{-\infty}^{\infty} \hat{E}_s(k_x,k_y;0)e^{i(k_x x+k_y y)}e^{ik_z z_0}dk_x dk_y, \tag{21}$$

where k_x , k_y , and k_z are the wavenumbers related to the Cartesian coordinates *x*, *y*, and *z*, respectively. $\hat{E}_s(k_x, k_y; 0)$ are the Fourier amplitudes of the electric field at $z = 0$. The difference between the near-field and the far-field regimes lies in the exponential term $e^{ik_z z_0}$ in Equation 21. The relationship between the k-vector (k_x, k_y, k_z) and the angular frequency $\omega = 2\pi c/\lambda$ is

$$k_x^2 + k_y^2 + k_z^2 = \frac{\omega}{\gamma_g}. \tag{22}$$

where γ_g is the group phase velocity and is related to the speed of light in a vacuum, *c*, by $\gamma_g = c/n$ where *n* is the index of refraction of the medium. Solving Equation 22 for k_z and introducing the transverse wavenumber $k_t \equiv \sqrt{{k_x}^2 + {k_y}^2}$, we obtain

$$k_z = \sqrt{(2\pi n/\lambda)^2 - k_t^2}. \tag{23}$$

For $k_t \leq 2\pi n/\lambda$, k_z is a real number and the exponential term $e^{ik_z z_0}$ indicates that E_s propagates along the z-axis, oscillating with $e^{i|k_z|z_0}$. This is the far-field component of the optical field. For $k_t > 2\pi n/\lambda$, k_z is an imaginary number and the exponential term $e^{ik_z z_0}$ indicates that E_s decays exponentially along the z-axis according to $e^{-|k_z|z_0}$. This evanescent field is the near-field component of the optical field.

For the near-field component, the absolute value of the transverse wavenumber depends on the characteristic dimension of the source structure, *d*, according to[21]

$$k_t \approx j(n\pi/d) \ \ (j = 1,2,\ldots). \tag{24}$$

where n is the index of refraction of the source structure. Evanescent fields are produced when light is sufficiently laterally confined to satisfy $k_t > 2\pi n/\lambda$. This leads to an equation for the characteristic dimension requirement for producing near-field light

$$d < j(n\lambda/2) \ \ (j = 1,2,\ldots). \tag{25}$$

When the light is laterally confined to a dimension smaller than $(n\lambda/2)$, all of the light is evanescent.

2.3.2 Resolution Limits

The resolution limits of near-field and far-field components of the optical field can be determined by adapting Heisenberg's uncertainty principle to the angular spectrum representation of the electromagnetic field, giving

$$\Delta r \Delta k_t \geq 2\pi, \tag{26}$$

where $\Delta r = \sqrt{\Delta x^2 + \Delta y^2}$ is the width of the field in direct space and Δk_t is the width of the field Fourier transform in the frequency space. For the far-field component, $k_{t,\max} = 2\pi n/\lambda$, leading to $\Delta k_{t,\max} = 4\pi n/\lambda$. This limits the minimum width of the field in direct space to $\Delta r_{\min} = \lambda/2n$. When we consider the limited collection angle of optics, n is replaced by NA to give the far-field resolution limit

$$\Delta r_{min} = \frac{\lambda}{2NA}. \tag{27}$$

The transverse wavenumber in the near-field produced by an aperture with diameter a is found from Equation 24 to be $k_{t,\max} = \pi n / a$, leading to $\Delta k_{t,\max} = 2\pi n / a$.[23] Thus, the resolution limit for near-field light is

$$\Delta r_{min} = \frac{a}{n}. \tag{28}$$

When imaging is performed in air, the typical case, n=1 [24] and the resolution limit is

$$\Delta r_{min} = a. \tag{29}$$

Because $a \ll \lambda$, the achievable resolution in the near-field is much greater than in the far-field. However, as the lateral confinement increases, the evanescent field decays faster in the z-direction. Similar to skin depth in alternating electric current, we define the near-field zone limit by the $1/e$ decay length of the electric field strength ($|E_s|^2$) of the evanescent field, given by[21]

$$\delta_{nf} = \frac{1}{2k_z}. \tag{30}$$

Using $k_{t,max}$ in Equation 30, we find that the decay length for the maximum-resolution evanescent field is

$$\delta_{nf,r_{max}} = \frac{\lambda}{2\pi}\frac{1}{\sqrt{(\pi n\lambda/a)^2 - 4}}. \quad (31)$$

Conversely, we can define the maximum resolution obtainable at a distance z_0 away from the sample, first solving for $k_{t,\max}$, then finding $\Delta r_{\min}$

$$k_{t,max}(x,y) = 2\sqrt{(1/2z_0)^2 + (2\pi/\lambda)^2}, \quad (32)$$

$$\Delta r_{min} = \frac{\pi}{\sqrt{(1/2z_0)^2 + (2\pi/\lambda)^2}}. \quad (33)$$

We see here that the achievable resolution in near-field imaging is defined by both the aperture diameter and the distance from the aperture. The practical resolution limit of confocal microscopy is ~250nm. In contrast, in aperture-SNOM, the practical resolution achievable is 50nm, a 5x resolution improvement over confocal microscopy.

2.3.3 Nanometer-Confined Light Source

The nanometer-confined light source for SNOM imaging can be implemented either by an aperture technique or an apertureless technique. In aperture-SNOM, near-field light is produced by confining the light within the probe to a small aperture at the probe tip. As the aperture size is decreased from much larger than the light wavelength to much smaller than the light wavelength, less light is transmitted through the probe until only evanescent waves are emitted from the aperture. Additionally, the directionality of the light emitted from the probe is decreased until the light is emitted nearly uniformly in all directions.[25] In apertureless-SNOM, near-field light is produced by focusing light onto a sharp metal tip. When the incident light is polarized parallel to the tip shaft, the incident electric field causes free electrons to oscillate along the tip shaft. At the tip apex, the surface area is very small. Therefore when the electrons are moved into the tip apex, the resulting surface charge density at the tip end is very large. These charges generate a secondary electric field that is more intense than the incident field, effectively enhancing the incident electromagnetic field at the apex of the tip, and producing near-field light at the tip that is brighter than the incident far-field light.[22]

Although both aperture-SNOM and apertureless-SNOM illuminate the sample with evanescent waves, they are best suited for different applications. In aperture-SNOM, the confinement in the probe causes a large portion of the intensity of the far-field light source to be lost, thus limiting the intensity of near-field light that can illuminate the sample. Apertureless-SNOM is not subject to this limit and produces near-field light intensity that is greater than the intensity of the far-field light source. However, aperture-SNOM is easier to implement and interpret because only near-field light illuminates the sample. In contrast, in apertureless-SNOM, both near-field light and the far-field light from the original source illuminate the sample. A complex detection scheme must be implemented to isolate the near-field light and post-processing may be required to deconvolve the resulting signal.

3 Centimeter-Scale Metrology of CVD Graphene

3.1 Introduction

Graphene is currently a rock star material in nanotechnology, stealing center stage from its nano-carbon sibling, the carbon nanotube, with a Nobel Prize win (Physics 2010, awarded to Andre Geim and Konstantin Novoselov) and riding high on a landslide of publications dedicated to its study. However, to successfully graduate from the laboratory and fulfill its promised destiny as a revolutionary of the energy, semiconductor, and thermal management industries, graphene needs to become relevant at larger scales. This requires increasing the size of graphene itself and developing large-scale industrial metrology techniques. Graphene is a two-dimensional sheet of graphite, consisting of one to ten layers of carbon atoms arranged in hexagonal lattices. It was first synthesized as micron-sized flakes through mechanical exfoliation of highly ordered graphite. Although the size limitation of mechanically exfoliated graphene inhibits its industrial application, many promising alternative synthesis techniques have been developed that can create larger graphene sheets. These techniques include chemical reduction of graphene oxide (rGO) and growth of graphene through chemical vapor deposition (CVD) of carbon atoms on metallic substrates, among many others. A recent review by Singh et al. provides an in-depth analysis of the current state-of-the-art techniques for synthesizing graphene.[26] Currently, CVD-growth of graphene appears to be the most promising synthesis technique for industrial applications, allowing high-throughput production of large graphene sheets.

With the addition of high-throughput synthesis to graphene's repertoire, the only remaining obstacle for widespread industrial use is large-scale industrial metrology. There are many techniques for characterizing graphene that measure a wide range of properties. In industry, the primary need is for characterization of specific properties against metrics of interest. For the energy, semiconductor, and thermal management industries, the most important metrics are: layers, edge structure, defects, Fermi level, and thermal conductivity. When a characterization method measures one of these metrics, it can be considered a metrology technique. Layer thickness and uniformity of a graphene sample are important parameters that affect the performance and properties of the sample. Additionally, cracks and wrinkles in the graphene sample cause variations in the electronic properties that are unrelated to the quality or thickness of the graphene. These defects are difficult to completely avoid due to complicated growth and processing procedures. Chemical doping, a major approach for tuning electronic properties, has been consistently applied in semiconductor technologies to control the type and density of charge carriers. Well-developed methods for graphene doping can produce n- and p-type conductions, which are required for complementary metal oxide semiconductor (CMOS) technology and, accordingly, logic circuits. Therefore, a high-throughput metrology technique that characterizes layer thickness and chemical doping of an entire CVD graphene sample is necessary for industrial applications.

The challenge in graphene metrology is mainly due to the dimensionality of the graphene sheet. Although the topic of whether nanomaterials should be officially defined is highly-contested,[27,28] the widely-accepted definition states that materials with at least one dimension smaller than 100nm can be considered nanomaterials. Graphene qualifies as a nanomaterial because the height of a single sheet is ~0.4nm. However, the width and length of a graphene sheet can vary drastically. Production of CVD graphene sheets up to nearly 1m has been reported,[29] although centimeter- to inch-scale sheets are more common. The large discrepancy between the height and the expanse of CVD graphene makes the task of graphene metrology very challenging. Currently, most metrology techniques focus on the small scale, where they can resolve the chemical structure of graphene. However, some large-scale metrology techniques that detect enhanced optical contrast of graphene have been introduced.

For industrial applications, metrology techniques must be quick, repeatable, and conclusive. Additionally, they should allow measurement of the entire region of interest on the substrate required for the given industrial application (e.g. glass substrates for solar cells). Therefore an industrial metrology technique should be high-throughput, scalable to allow characterization of entire large-area CVD graphene samples, insensitive to environmental factors or substrate interactions, and quantified for automated decision making in addition to measuring the metrics of interest.

In the next section, we summarize the current graphene metrology techniques, describing which metrics they measure and their suitability for an industrial metrology technique. Although each technique has benefits, none of the current metrology techniques can be considered industrial. In this work, we develop and demonstrate the first industrial metrology technique for graphene. Our metrology technique is based on FQM and allows repeatable, quick, and easy identification of layer thickness and uniformity and visualization of chemically-doped regions of large-area CVD graphene sheets on arbitrary substrates.

3.1.1 Current Graphene Metrology Techniques

In this section, we review the current graphene metrology techniques, providing some insight into the experimental setup and indicating which industrial metrics they study. A convenient summary of the metrics studied by each technique is included in Table 1 at the end of this section.

3.1.1.1 Electron Microscopy

Electron microscopy employs an electron beam and is performed in a vacuum chamber to minimize random electron scattering. There are two forms of electron microscopy, transmission electron microscopy (TEM) and scanning electron microscopy (SEM). In TEM, electrons passing through sample are detected. TEM offers a sensitive, atomic-resolution imaging solution for characterizing graphene at the cost of extensive sample preparation. Due to the sensitivity of this technique, graphene must be suspended over a gap or hole in the imaging substrate. TEM imaging of graphene is further complicated because the electron energy must be reduced to avoid damaging the graphene sample. This has lead to many creative TEM imaging solutions, such as aberration-corrected TEM,[30–32] and high-angle annular dark-field scanning TEM.[33]

TEM has been used to show the atomic structure of suspended exfoliated graphene,[34] rGO,[35] and CVD graphene[36] membranes and can study edge structure.[37] Further, TEM can investigate defects in graphene[32,38] and even reveal charge-transport effects of doping.[39] Combining image processing techniques with TEM imaging has enabled the effect of nitrogen doping on CVD graphene to be studied.[39] TEM can identify graphene layers by imaging a cross-section of the graphene sheet (XTEM). XTEM is achieved by imaging a fold in the graphene sheet[34] or cutting the graphene sheet (e.g. using a focused ion beam).[40,41] XTEM is considered the most dependable method for identifying graphene layer thickness. Electron diffraction, a TEM technique performed by shifting the imaging focus from the sample to the back focal plane of the microscope, allows observation of the lattice structure through the interference pattern.[32,34,42] Interestingly, it has been discovered that graphene makes an excellent support substrate to enable high-resolution TEM investigation of other samples.[38]

In SEM, the electron beam is raster-scanned over the sample surface and the backscattered or secondary electrons are detected. SEM is a simple and relatively fast imaging technique and is primarily used to visualize graphene sheets and measure their size and uniformity.[43–46] When graphene was first discovered, SEM was used to identify few-layer graphene, which was not distinguishable from single-layer graphene by optical characterization methods available at the time.[47] SEM has also been used to identify edge structure in high-quality exfoliated graphene sheets.[48] SEM imaging of graphene requires a conductive support substrate. Although it cannot identify layer thickness, SEM is an excellent technique for measuring the size of exfoliated graphene sheets and identifying cracks in the sample due to its fast image formation.

3.1.1.2 Scanning Probe Microscopy

Scanning probe microscopy (SPM) refers to any microscopy technique that utilizes a probe scanned over the surface of the sample. The most widely-used SPM technique is AFM. Although the lateral resolution of AFM is limited by the probe dimensions (practical limit ~10nm), the vertical resolution can reach 0.1nm and atomic-scale height variations can be detected. AFM is commonly used to identify individual layers in exfoliated[47,49] and CVD[46,50] graphene. However, drift in the probe height feedback and height variations in the substrate can introduce measurement error over large areas. Additionally, it has been discovered that graphene does not always lay flat against the substrate, with the gap between graphene and the substrate reaching 5-10Å. This height is significant given that a single layer graphene is ~4Å and bi-layer graphene is ~8Å.[47] Therefore, AFM identification of layers is most reliable at edges, where sharp height variations are easily discernable. In addition to measuring layer height, AFM is also a helpful tool in studying the surface structure of functionalized graphene, through both height and phase measurements.[51–53] For the most part, AFM is slower than SEM and therefore only used over SEM when layer thickness is of interest.

Another SPM technique that is used for high-resolution imaging of graphene is STM. STM is the famous older sibling of AFM. The inventors of STM (Ernst Ruska and Heinrich Rohrer) shared their 1986 Nobel Prize win with the inventor of the electron microscope (Gerd Binnig) and went on to develop the first AFM. In STM, a conductive tip is kept at a constant bias voltage as it is scanned over the sample. Electrons that tunnel through the vacuum between the probe and the surface are detected as the tunneling current. This tunneling current is sensitive to the surface work function and density of states.[54,55] Like TEM, the resolution offered by STM allows direct study of the structure of exfoliated graphene,[56,57] CVD-grown graphene,[36,40] and graphene oxide.[51] Since STM current depends on density of states,[58–60] it has become a very useful technique for studying defects in epitaxial-grown graphene,[61] CVD-grown graphene,[36,40,62] and rGO[51] and for studying defects at the edge.[63] STM can also be used to measure dopant concentration on the graphene sheet.[62] Additionally, scanning tunneling spectroscopy (STS), where the bias voltage is scanned, allows direct measurement of the Fermi level[61,64] and determination of edge structure.[65]

3.1.1.3 Raman Spectroscopy

Raman spectroscopy, which measures inelastic Raman scattering, is a characterization technique with fame to match graphene, having won the Nobel Prize in Physics in 1930 (awarded to Sir C. V. Raman). In Raman spectroscopy, laser light is shone onto the sample and the wavelength shift in the reflected light is recorded as the Raman spectrum. In the case of a homogeneous sample, peaks appear in the Raman spectrum that correlate to bond energies.

Raman spectroscopy has become a gold-standard for graphene characterization. This is due to the sheer quantity and quality of the chemical information given by a Raman spectrum. Raman spectroscopy of graphene was first described by Ferrari et al. in 2006.[66] There are a number of thorough reviews on the applications and basics of Raman spectroscopy of graphene.[67–72] Raman spectroscopy is nearly the perfect tool for graphene metrology because it is sensitive to all of the industrial metrics. Raman can be used to study the change in the Fermi level due to chemical or electrical doping[62,73–76] and study edge structures.[77,78] Primarily, however, Raman is used study the structure of the graphene sheet and the layer thickness.[66,79–83] The ability to quantify defects through Raman has made it an essential tool for studying the quality of CVD-grown graphene, where defects are a common problem.[40,43,84–87] Finally, Raman can be used to study the thermal conductivity of graphene.[88,89] Recently, it was discovered that the sensitivity of Raman spectroscopy can be extended by incorporating graphene into the experimental setup. Single- and few-layer graphene was found to enhance the Raman signal from molecular adsorbates.[90]

Raman is largely insensitive to substrate and temperature effects (large temperature shifts slightly affect the G peak position).[79,91,92] The only limitation that keeps Raman from becoming the gold standard for graphene metrology is the low throughput of the technique. While the excitation laser used in Raman spectroscopy can be scanned over the sample to collect spatial Raman maps,[43–45,80,82,93,94] scanning Raman measurements take a long time because at each collection point 0.5-1 minute is required to collect the Raman spectrum. Mapping a $20x20\mu m^2$ exfoliated graphene flake at 1μm resolution requires nearly 7 hours of continuous Raman scanning. In this sense, Raman is the slowest characterization technique for graphene and cannot adequately characterize an entire large-area CVD graphene sheet.

3.1.1.4 X-ray Photoemission Spectroscopy

X-ray Photoemission Spectroscopy (XPS) measures the kinetic energy of the sample surface. From the kinetic energy, binding energies can be calculated. XPS joined the rank of distinguished metrology techniques in 1981, when Kai Siegbahn, the inventor of XPS, won the Nobel Prize in Physics. Through the presence and relative height of peaks in the XPS spectrum, the relative composition of elements and electronic structure of graphene can be determined.[95] Because the type and concentrations of chemical impurities can readily be measured, XPS is an excellent tool for studying the chemical state of doped CVD graphene[29,62,96] and rGO.[53,97,98] In the case of doped graphene, the Fermi level can be determined from the dopant type and concentration.[62] Generally, spatial maps are not generated from XPS data. Instead, one to three studies on a graphene sample are considered adequate to characterize the chemical state.

3.1.1.5 Optical Reflection

Optical reflection is used to identify graphene through differences in refractive index between the graphene and substrate. It is an excellent visualization tool, with the ability to study large areas quickly, and played a key role in the experimental discovery of graphene.[47] The imaging substrate used to discover graphene is still the most popular – a silicon (Si) wafer covered with a 300nm-thick silicon-dioxide (SiO_2) layer. This oxide layer is instrumental in creating a Fabry-Perot type cavity which maximizes the visibility of graphene through optical interference. Studies on the color contrast between graphene and the Si/SiO_2 substrate and between graphene layers measured the maximum contrast between layers to be 12%.[46,82,99–101] Color contrast in the optical reflection has been used to segment images of exfoliated graphene according to layer thickness[100] and to statistically determine the uniformity of CVD graphene.[46] In optical reflection, the thickness of the oxide layer is a critical parameter for enhancing contrast, with a change of a few nanometers rendering graphene nearly invisible.[102,103] The silicon wafer also has an impact on the reflected contrast and replacing it with another material changes the contrast.[103–105]

Although some industrial applications, such as semiconductors, utilize Si/SiO_2, many require different substrates, such as glass substrates for solar energy. There have been a few studies on characterizing graphene layers through reflection using different substrates, including glass[106] and the copper growth substrate.[107] These studies demonstrate the promise of reflectance microscopy on alternate substrates, but still fall short of being suitable for reliable layer identification, with only 1% contrast between graphene layers on copper and 7% contrast on glass.

Table 1 Industrial metrics measured by graphene characterization techniques.

	Layers	**Edge Structure**	**Defects**	**Fermi Level**	**Thermal Conductivity**
TEM	Cross section of cut or fold[34,40,41]	Atomic edge structure imaged directly[37]	Variations in lattice structure imaged directly[32,38]	-	-
SEM	-	Identified in extended edges of high-quality exfoliated flakes[48]	-	-	-
AFM	Sharp height variations at edges[46,47,49,50]	-	-	-	-
STM	-	Scanning bias voltage[65]	Density of state measurements[36,40,59,61,62]	Scanning bias voltage[61,64]	-
Raman Spectroscopy	Relative peak height (G and 2D) and location (2D) [66,79–8366,80–83]	D peak height using horizontal polarization[77,78]	D peak height[43,84–87]	G peak position[62,73–76]	Relationship between G peak position and dissipated power[88,89]
XPS	-	-	Relative peak height / positions[4,30,39,73–75]	Determined from dopant type and concentration[62]	-
Reflection Microscopy	Color contrast, depends on substrate[46,82,99–101]	-	-	-	-
FQM	Intensity contrast, customized by dye layer thickness	-	Intensity contrast of the layer decreases	Intensity contrast of the layer decreases	-

3.1.2 Fluorescence Quenching for Industrial Graphene Metrology

3.1.2.1 Industrial Metrology

In industrial applications, graphene will be embedded as a component of a wide variety of devices, from semiconductor devices to solar cells. Therefore, graphene metrology must be performed in-line with production and on arbitrary substrates. To fit into the production workflow, an industrial metrology technique must be: (1) high-throughput, (2) scalable to allow characterization of entire large-area CVD graphene samples, (3) insensitive to environmental factors or substrate interactions, and (4) quantified for automated decision making. The suitability of the current metrology techniques for industrial metrology according to these criteria is summarized in Table 2.

Of the techniques covered thus far, optical reflection is the only high-throughput metrology technique. Recognizing the benefit of high-throughput optical reflection metrology, Nolen et al. developed a technique for segmenting the optical reflection image according to layer thickness to provide quantified results.[100] The small size and uniformity of exfoliated flakes simplifies the task of identifying layers, allowing even Raman mapping to achieve layer identification of the entire flake.[80] However, the small size of exfoliated graphene also means that industrial interest in the material is limited. Reina et al. were the first to expand quantified optical reflection metrology to CVD graphene, bringing the technique one step closer to industrial use.[46] The characterized region was still limited to a subset of the CVD graphene sheet and they did not attempt to segment the image according to layer thickness, instead limiting their analysis to statistical determination of uniformity. This decision may have been due to the difficulty in identifying CVD graphene layers with high confidence. Although it is high-throughput, optical reflection metrology is limited by the achievable contrast between graphene layers, which makes layer identification difficult on a large scale. Furthermore, it is highly sensitive to the imaging substrate, which limits its usefulness in industrial applications.

In this work, we develop a new graphene metrology technique which is based on FQM, a novel visualization technique that detects fluorescence quenching by graphene. Fluorescence quenching was first utilized to visualize graphene immobilized on a fluorescent dye-functionalized substrate.[108] Kim et al. built on this concept, introducing the fluorophores in the form of a fluorescent dye-polymer layer deposited on the graphene and substrate by spin-coating and introduced the term "fluorescence quenching microscopy" to describe this technique. FQM allows the contrast of fluorescence quenching to be customized by controlling the dye-polymer layer thickness and can be performed on arbitrary substrates.[109,110] Around the same time, Sagar et al. used quenching of the intrinsic fluorescence in PMMA to create a hybrid graphene visualization/fabrication technique, demonstrating the applicability of a fluorescence-based graphene metrology technique in industry.[3]

By quantifying the contrast measured by FQM, we achieved high-throughput metrology of graphene on arbitrary substrates. We then obtained quantified results by employing image processing techniques. The resulting metrology technique is well suited to industrial applications (Table 2) and has the following capabilities:

1 Identification of layer thickness and uniformity and visualization of chemical doping
2 Characterization of entire large-area CVD graphene sheets
3 Repeatable across imaging microscopes and imaging sessions
4 Fast collection time

In the following section we provide a brief introduction to fluorescence quenching by graphene and give an overview of the industrial graphene metrology technique we developed that relies on this property.

Table 2 Industrial metrology capabilities provided by graphene metrology techniques

	Throughput	Characterization Area	Substrate/Environment Requirements	Quantified Results
TEM	Very low, a great deal of sample preparation is required and image formation is slow	Very Small	Support substrate with large holes / Vacuum environment	-
SEM	Mediocre, sample preparation required but image formation is fast	500x500μm^2 regions demonstrated.[43] Limited by desired resolution	Conductive substrate / Vacuum environment	-
AFM	Low, data acquisition speed limited by probe scanning control	Small. Limited by throughput, scan size, and feedback drift	Atomically flat substrate	-
STM	Very low, data acquisition speed limited by probe scanning control	Small	Atomically flat, conductive substrate / Vacuum, low temperature environment	-
Raman Spectroscopy	Very low, 0.5-1 minute per collection point	Small. Limited by throughput	Very low substrate and environment sensitivity	-
XPS	Extremely low, usually only one or two points are measured	-	Vacuum environment	-
Reflection Microscopy	Very fast, thousands of data points collected simultaneously	120x120μm^2 regions demonstrated.[100] Limited by contrast	Substrate stacking and refractive index determine contrast	Image segmentation according to layers (exfoliated graphene, calibration required)
FQM	Very fast, thousands of data points collected simultaneously	1cm^2 regions demonstrated.[111] Unlimited due to high contrast	Very low substrate and environment sensitivity	Highly repeatable image segmentation according to layers (CVD graphene, no calibration required)

3.1.2.2 Fluorescence Quenching by Graphene

Due to its unique electronic properties, graphene has some similarities with metal, a known fluorescence quencher, making it a promising material for fluorescence quenching studies. Electrons in the sp^2-hybridized p_z orbitals of the carbon atoms that make up graphene are easily excited and have π-π* transition energies that fall within the energy range of visible light, making graphene an excellent energy acceptor.[3]

The two primary mechanisms through which energy is transferred to graphene from a fluorophore in the excited state are Dexter electron transfer and FRET. There have been many studies on fluorescence quenching by graphene through Dexter electron transfer[112,113] and FRET.[11,12,14] Although these studies do not compare the quenching rates of these processes to determine which is dominant, FRET can be considered to be the dominant process for distances greater than 2nm due to the short-range interaction required for Dexter electron transfer. Classical FRET theory is concerned with the dipole-dipole interaction between two dye molecules, which exhibits the d^{-6} distance dependence. Because graphene is a 2D material, this distance dependence is reduced to d^{-4} between a dye molecule and graphene, as explained in Chapter 2.[7,8,14] Therefore, while classical FRET is usually restricted to 10nm, FRET involving graphene can occur up to distances of 30nm.[12]

Dexter electron transfer depends heavily on diffusion,[4] therefore its efficacy is severely attenuated when the fluorophores are immobilized, as is the case in the polymer-dye layer used in FQM. Additionally, fluorescence quenching was observed in FQM even when a 20nm-thick non-fluorescent spacing layer was added between the graphene and the dye layer.[109] Therefore we conclude that FRET is the dominant quenching process in FQM.

In FQM, the fluorescence throughout the entire dye layer is recorded for each point. Therefore, the fluorescence intensity from quenched dye regions depends on acceptor-donor distances ranging from zero at the graphene surface to the dye layer thickness at the surface of the dye layer. Over the substrate, where no quenching occurs, the measured intensity is proportional to the dye layer thickness. Over the graphene, fluorophores in the dye layer are quenched by the graphene, with the quenching efficacy depending strongly on the distance between the fluorophore and graphene. Therefore, contrast between the graphene and the substrate can be controlled by varying the dye layer thickness. The quenching of the dye layer is also limited by the concentration of acceptor states. In samples where the number of donors far-outnumber the number of acceptors, as is the case in FQM, quenching is proportional to the density of acceptor states. Therefore, another way of controlling the contrast between graphene and the substrate is by varying the number of graphene layers, which changes the number of acceptor states. This effect is the basis of first application of FQM, large-scale industrial quantification of the thickness and uniformity of large-area CVD graphene sheets and also contributes to reduced quenching by doped graphene.

While graphene is an excellent energy acceptor due to extended sp^2-hybridized carbon bonds,[4,8,109] graphene oxide does not quench fluorescence as effectively due sp^3 bonds with the oxygen functional groups. In sp^3-hybridized orbitals, all of the valence electrons are in σ bonds, which have high excitation energies (~200nm).[3] Therefore, electrons in sp^3-hybridized orbitals don't absorb visible light, making them poor energy acceptors from the fluorophores. This effect has been shown experimentally, where quenching was greatly increased when graphene oxide was reduced, restoring the sp^2-hybridized orbitals.[109] Similarly, when graphene is chemically doped by adding functional groups to the surface, the number of acceptor electrons in sp^2 orbitals is reduced. In this case, the reduction in quenching efficiency is expected to be proportional to the reduction in sp^2 orbitals. However, there is also another effect of changing the bonds – changing the distribution of acceptor states. While pristine graphene has a 2-dimensional acceptor state geometry, many of the acceptor states are removed during the doping process, which could cause the remaining acceptor states to become isolated and could, in turn, change the acceptor state geometry and the resulting FRET distance dependence.

Doping can also affect fluorescence quenching in FQM due to the shift in the Fermi level. In pristine graphene, the Fermi surface is a set of six points known as the K-points and the density of states at the Fermi level is zero. Through chemical and electrical doping, the Fermi level is shifted, causing a non-zero density of states at the Fermi level. A theoretical study on the effect of Fermi level shift on FRET transfer found that, for large z (outside Dexter electron transfer distance, ~2nm), there are two different distance dependence functions, depending on the relationship between the dye emission energy and the Fermi level shift. For a Fermi level shift less than one-half of the dye emission energy, the distance dependence of FRET is d^{-4}, similar to pristine graphene. However, if the Fermi level shift is greater than one-half of the dye emission energy, distance dependence is exponential, resulting in reduced quenching.[114]

Due to the highly effective, long-distance quenching of fluorescence by graphene, it is a promising acceptor material for fluorescence-intensity based biosensors[115,116] developed to detect DNA,[117–119] proteins,[120–122] and other biomolecules.[123–126] Additionally, resonant energy transfer to graphene has been used to harvest energy from fluorescent quantum dots[127–129] and dye molecules.[130,131] Because it is capable of near-absolute quenching of the fluorescence signal that interferes with Raman measurements, graphene can also be used as a substrate to enable Raman measurements of fluorescent materials.[132] Recently, however, it has been discovered that a powerful application of fluorescence quenching by graphene is visualizing the graphene itself.

Due to its high throughput and controllable contrast, FQM had great potential to be extended beyond the state of other metrology techniques and become truly relevant for industry. To develop FQM into an industrial metrology technique, we made four major improvements: (1) quantification of quenching contrast to identify graphene regions, (2) large-scale image collection to measure entire CVD graphene sheets, (3) mapping of doped regions of graphene, and (4) image segmentation for quick and easy graphene layer identification.[111]

3.2 Methods

3.2.1 Graphene Growth

CVD graphene films were grown using a 25µm-thick copper foil (Alfa Aesar, item No. 13382) as a catalyst.[43] The copper foils were pretreated with acetic acid and deionized (DI) water to ensure the surfaces were completely clean and free from oxidation. Next, the pretreated copper foils were loaded into a quartz-tube furnace chamber and heated to 1000^{o}C in a 2-Torr Ar/H_2 (200:200 sccm) atmosphere and thermally annealed for 30 minutes. For the growth of graphene, methane (100 sccm) was introduced into the chamber under 20 Torr for 20 minutes and the chamber temperature was cooled down to 25^{o}C at a cooling rate of 20^{o}C/minute. The graphene samples were removed from the growth chamber and covered with poly(methyl methacrylate) (PMMA) by drop-coating and heated at 120^{o}C for 10 minutes to dry the PMMA layer. The copper foil was then etched in iron(III) chloride ($FeCl_3$) aqueous solution (0.5M) and rinsed thoroughly with hydrochloric acid (3%) and DI water, respectively.

Glass substrates were prepared by cutting microscope slides into 1in^2 squares and cleaning by gently rubbing with a clean gloved finger and liquid detergent, followed by sonication for 10 minutes each in DI water, toluene, acetone, and isopropyl alcohol (IPA) and finally blowing dry with a nitrogen stream. Floating graphene samples were fished onto the substrate and allowed to dry overnight. To remove the transfer PMMA from the graphene, the samples were soaked in heated acetone for 30 minutes, soaked in heated IPA for 10 minutes, and dried under a nitrogen stream. The samples were stored in a vacuum desiccator.

3.2.2 Graphene Doping

For patterned fluorine doping, a CVD graphene sheet immobilized on a glass substrate was spin-coated with a photoresist layer. Next, photolithography was performed using a patterned mask having circular and stripe windows to define the areas to be doped. Upon development of the mask, graphene sheets were selectively fluorinated using a reactive ion etching (RIE) machine. The plasma treatment was carried out at room temperature with the CF_4 gas pressure fixed at 10 mTorr, while the CF_4 flow rate was kept constant at 50 sccm. Graphene fluorination was performed with 10 seconds of plasma exposure at an RF power level of 25W. After dissolving the photoresist in acetone overnight, selectively doped graphene was dried and prepared for dye coating.

3.2.3 Dye-Doped Polymer Preparation and Coating

The dye mixture was prepared by adding 0.01wt% 4-(Dicyanomethylene)-2-methyl-6-(4-dimethylaminostyryl)-4H-pyran (DCM, Sigma Aldrich) to 10mL 1.0wt% PMMA (Mw ~120,000) dissolved in toluene (>99.5%, Fisher Chemical). This dye-polymer solution provides complete dispersion and low evaporation during spin-coating due to the low vapor pressure of toluene, allowing formation of a uniform layer with repeatable thickness. Additionally, the excitation energy of DCM is well below the absorption energy of PMMA and the spin-coating behavior of PMMA dissolved in toluene has been well-studied.[133–135] Finally, PMMA is already used as a protection layer during CVD graphene transfer and as the protection film during photolithography. Therefore, it is well known that PMMA does not damage the graphene sample, it is easily washed away with acetone, and many advanced techniques have been developed to ensure complete contaminant removal, if necessary.[57,136]

The solution was stirred and heated overnight to dissolve the polymer, then continuously stirred until used to prevent agglomeration of the dissolved polymer. Before coating the graphene sample, the dye was placed in a water bath and heated gradually from room temperature to 85°C. The dye was then held at this temperature for 1 hour before being gradually cooled back down to room temperature. This process of heating and cooling the dye was then repeated once more to further prevent agglomeration and create a homogenous dye. Immediately before the solution was spun onto the substrate, it was sonicated for 15 minutes. To ensure that any bright spots seen in the FQM image of graphene were due to contamination on the surface, the dye solution was passed through a 0.22µm filter before being deposited on the substrate. The dye layer was formed by flooding the substrate with the dye mixture then spinning the substrate at 3000rpm for 60 seconds with a 2-second ramp. Next, the sample was stored in a vacuum desiccator for one hour to completely evaporate the solvent. This step is necessary to achieve consistent contrast measurements for the graphene layers. As the solvent evaporates, the layer thickness decreases which alters the quenching of the dye layer and the contrast between graphene layers and the substrate. The dye layer thickness was determined by forming scratches in the polymer layer with plastic tweezers and measuring the height difference with a Veeco Dektak 8 surface profilometer.

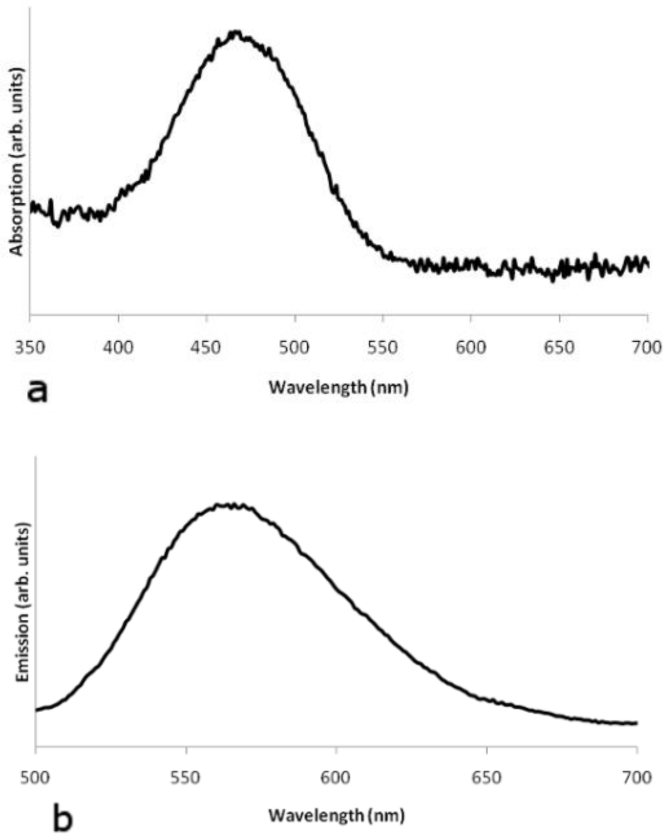

Figure 4 Dye-doped polymer absorption and fluorescence emission spectra.

The fluorescence spectrum of dyes depends on the solvent used to dissolve the dye powder. Because the spectra for DCM dissolved in toluene with PMMA have not been previously recorded, we measured the absorption and emission spectra of our polymer dye solution after it was spin-coated onto glass slides. The measured spectra are shown in Figure 4. The fluorescence collection and emission optics were determined from the peaks in the absorption and emission spectra. The measured absorption and emission peaks for the dye polymer mixture are 470nm and 560nm, respectively.

3.2.4 Fluorescence Microscopy

Fluorescence images of the dye-coated graphene were collected using a BD Pathway 855 HT Confocal microscope. An arc lamp was used as the light source. The illumination light was filtered through a 470nm (+/-40nm) bandpass filter and a dichroic filter (520nm) and focused on the sample using an Olympus 20x objective with a 0.75 numerical aperture. The emitted light was passed through a 542nm (+/-27nm) bandpass filter and detected with a CCD camera. BD AttoVision software, which is provided with the Pathway microscope, was used to control the mechanical stage and collect montage images. Photobleaching of the dye-polymer layer was avoided by limiting the illumination intensity of the light source (~10%), enabling consistent fluorescence contrast for multiple measurements of the same sample.[109]

3.2.5 Fluorescence Characterization

Steady-state emission spectra were recorded using a Fluorolog-3-22 spectrofluorometer (Horiba Jobin-Yvon), with slit widths between 2nm and 5nm. Absorption spectra were recorded using a JASCO V-670 UV/Vis/NIR spectrophotometer. All measurements were performed at ambient temperature. Fluorescence spectra of dye (original and quenched by pristine/doped graphene), were obtained in response to 406nm light excitation.

Time-resolved emission measurements were conducted with a TBX single-photon-counting detector and a NanoLED laser source. For recording the profile of the excitation pulse (i.e., the instrument response function), we used an aqueous solution of bovine serum albumin as a scatterer, setting $\lambda_{em} = \lambda_{ex}$. The fluorescence decay, *D(t),* collected at emission wavelength λ_{em}= 566nm, was fit to a convolution integral:

$$D(t) = L(t) \otimes F(t) \tag{34}$$

where the recorded profile of the laser pulse was adopted for the instrument response function, L(t). The decay function, F(t), is the Laplace transform of α(t), which represents the distribution of the amplitudes of the exponential decays with different lifetimes, τ,

$$F(t) = \int_0^\infty \alpha(\tau) \exp\left(-\frac{t}{\tau}\right) d\tau^{-1} \tag{35}$$

Reported lifetimes were obtained from bi-exponential data fits.

3.2.6 Raman Characterization

Raman spectra were collected with a Thermo-Fisher Scientific micro-Raman equipped with DXR 532nm Excitation Laser Set.

3.2.7 Image Processing

All image processing was performed on a standard laptop using Matlab (Mathworks, Natick, MA).

3.3 Results

3.3.1 Large-Area, High-Throughput Identification of CVD Graphene Layers on Arbitrary Substrates

High-throughput production of graphene can be achieved by growing graphene via CVD of carbon atoms on metallic substrates.[43,46,50,137] Graphene creation using mechanical exfoliation is labor intensive and only produces a few small graphene samples whereas the size of CVD-grown graphene is only limited by the size of the growth chamber.[138] CVD graphene has been developed for many different industrial applications, such as electronic devices,[139–141] solar cells,[142,143] and energy storage.[144] The layer thickness and uniformity of a graphene sample are important parameters that affect the performance and properties of the sample. Additionally, cracks and wrinkles in the graphene sample cause variations in the electronic properties that are unrelated to the quality or thickness of the graphene. These defects are difficult to completely avoid due to complicated growth and processing procedures. Therefore, a high-throughput metrology technique that characterizes an entire CVD graphene sample is necessary for industrial applications.

In this work, we advance FQM by introducing a method for identifying and counting graphene layers using histogram-based segmentation. Our large-area graphene metrology technique is illustrated in Figure 5. Briefly, we coat the graphene sample with a dye-polymer solution and image using a fluorescence microscope. To characterize an entire CVD graphene sample, we collect a large-scale, high-resolution montage image and process the image to remove the effects of non-uniform illumination. Next, we analyze the histogram of the resulting image to identify the unquenched fluorescence intensity. The intensity ranges within the histogram that correspond to graphene layers are then calculated from the known contrast ranges. Finally, the image is segmented by mapping pixels to different colors depending on their intensity values. Utilizing this technique, we achieve high-throughput thickness and uniformity metrology of entire CVD-grown graphene samples on a glass substrate. Because the contrast provided by FQM does not depend on the substrate or sensitivity of the microscope, this method does not require additional calibration, allowing for fully-automated metrology measurements. This work introduces a new method for graphene metrology that allows quick and easy identification of graphene layers in a large area on arbitrary substrates.

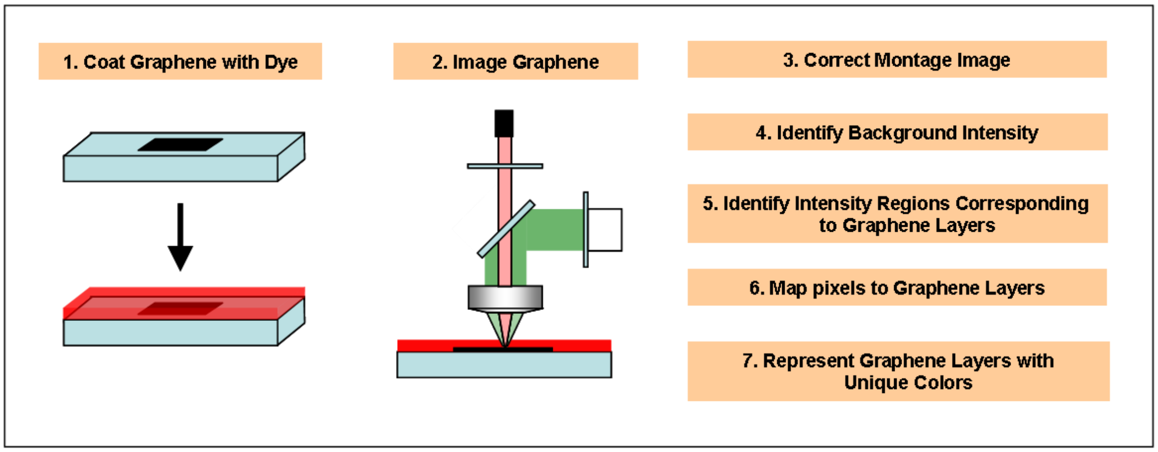

Figure 5 Schematic of our large-area, high-contrast graphene metrology technique.

3.3.1.1 Large-Area High-Contrast Fluorescence Imaging

The contrast between graphene and the substrate can be customized by controlling the thickness of the dye layer, from complete quenching with a dye monolayer[108,132] to negligible quenching with a thick dye layer. In this study, we coated the graphene with a 30nm-thick dye layer to provide optimal contrast for few layer graphene. Contrast between graphene layers is reduced with a thinner dye layer, while contrast between graphene and the substrate is reduced with a thicker dye layer. After dying the graphene sample, we imaged the graphene with a fluorescence microscope equipped with a mechanical stage. To achieve high-resolution imaging, a 20x (0.75 N.A.) imaging objective was used. With this objective, an image covers a 417x318μm^2 area. To image the entire graphene sample, which covers approximately 1cm^2, a montage of individual images was collected. This objective can achieve a resolution of 380nm, however to reduce the noise in the image and keep the size of the montage image file reasonable, we averaged a 4x4 segment of pixels into one final pixel. This resulted in an effective pixel size of 1.24x1.24μm^2. The final image is free from noise and does not need to be further filtered.

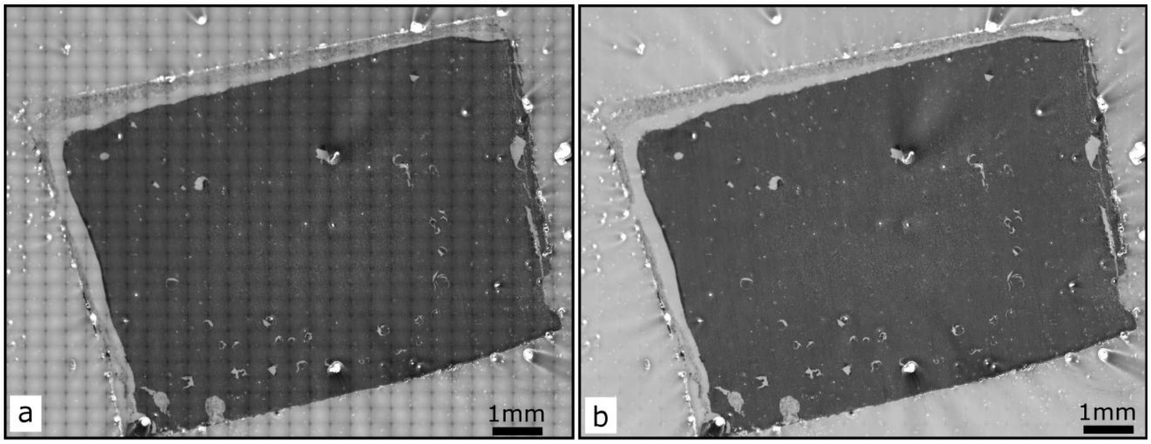

Figure 6 Fluorescence image of dyed CVD graphene sample (a) before and (b) after background correction.

The fluorescence montage image of single-layer CVD graphene is shown in Figure 6a. The montage consists of 34x46 individual images. Because the illumination across one image is not completely uniform, individual images in the montage image can be identified by their dark outlines. This non-uniform illumination can be corrected using the standard microscopy flatfield correction technique. Briefly, a correction image is created by imaging a uniform fluorescence sample such as a dye layer covering a bare substrate. This image should be created using the same imaging pathway used to create the montage image but only needs to be created once every few months as the illumination source ages. Each area in the montage image that represents an individual image is corrected using

$$I_{flat}(x,y) = \frac{I_{original}(x,y)}{I_{correction}(x,y)} \cdot \overline{I_{correction}} \tag{36}$$

The flattened image is shown in Figure 6b. The non-uniform illumination has been entirely corrected. In the flattened FQM image the graphene can be clearly seen and some folds and cracks are apparent.

3.3.1.2 Identification of Graphene Layers

Identification of the graphene layers is achieved by histogram-based segmentation based on contrast relative to the substrate. The fluorescence intensity, I_f, of the dye layer coating the graphene sample is given by

$$I_f = (1 - f_Q) \cdot I_{f0} \tag{37}$$

where I_{f0} is the original fluorescence intensity of the dye and f_Q is the fluorescence quenching factor which depends on the number of graphene layers and the thickness of the dye layer. Because the glass substrate does not quench the dye fluorescence, the quenching factor is for the substrate is equal to 0 and the fluorescence intensity of the substrate is equal to I_{f0}. Contrast between graphene layers and the background is given by the equation

$$C = \frac{I_{background} - I_{graphene}}{I_{background}} \tag{38}$$

Substituting I_{f0} for $I_{background}$ and I_f for $I_{graphene}$ in Equation 38 gives the relationship between the quenching factor and the contrast between the graphene layer and the substrate,

$$C = f_Q. \tag{39}$$

The fluorescence intensity of the graphene layers and the substrate can vary between images due to variations in the illumination intensity. However, the contrast between the graphene layers and the substrate is determined by the quenching factor, which is constant across samples and microscopes and depends only on the dye layer thickness.

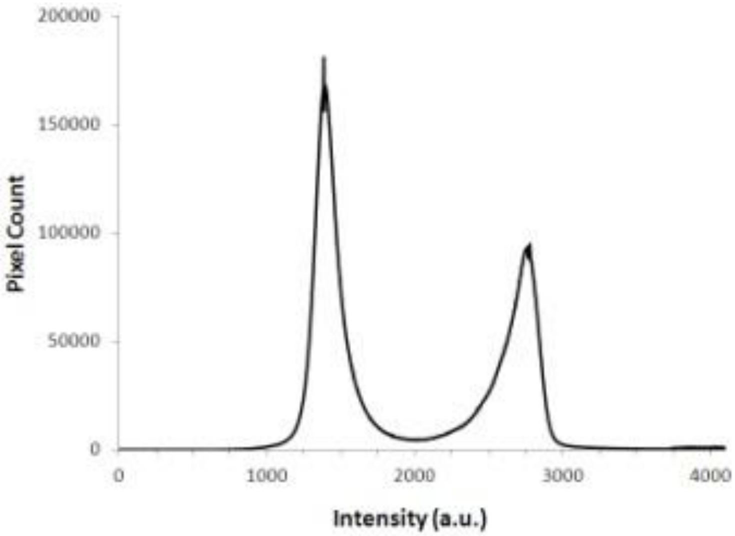

Figure 7 Histogram of the corrected fluorescence image of CVD graphene.

The first step in our segmentation algorithm is measuring $I_{background}$. This is achieved by analyzing the image histogram. Two major peaks are apparent in the histogram of the corrected fluorescence image of the CVD graphene sample (Figure 7). The peak at higher fluorescence intensities represents the substrate while the peaks at lower intensities represent the graphene. $I_{background}$ is the intensity value that correlates to the apex of the substrate peak in the histogram. Once $I_{background}$ is determined, the contrast value for each pixel is calculated according to

$$C(x,y) = \frac{I_{background} - I(x,y)}{I_{background}}. \tag{40}$$

Next, the image is segmented according to the pixel contrast value. Our measurements on multiple graphene samples found that for a 30nm-thick dye layer, the contrast range for single-layer graphene is 0.35-0.58 and the contrast range for two-layer graphene is 0.58-0.75. These ranges indicate that the contrast per layer decreases as the layer count increases. This decrease in quenching by subsequent layers was also predicted theoretically and observed experimentally in a study on the quenching of fluorescent nanocrystals by graphene.[127] Ideally, the contrast for different layers would be discrete values instead of value ranges. This would be the case for exfoliated graphene samples. CVD samples, however, have variations on the nanometer scale which cannot be adequately resolved due to the resolution limit of light. The signal from these regions is averaged to obtain the intensity value for each pixel in the collected image. Therefore the intensity peaks in the fluorescence image histogram resemble Gaussian peaks and represent the low-passed version of the ideal discrete peaks.

In addition to identifying graphene layers, our segmentation algorithm identifies contamination on the graphene surface. This is possible because the contamination particles obstruct the distribution of dye as it is spun onto the graphene sample, causing the dye to build up around the particles which results in regions where the fluorescence intensity is brighter than the fluorescence of the flat substrate. Very large contamination blocks the flow of dye, which creates regions with a thinner layer of dye. This can lead to incorrect identification of the graphene layers. Therefore, detecting contamination in the segmentation algorithm is important for accurate interpretation of the segmentation results. The contrast range for pixels darker than the substrate is 0-1 while pixels brighter than the substrate (part of the Gaussian peak representing the substrate and surface contamination) have negative contrast values. The segmentation algorithm maps pixels to graphene layers, L_n, according to

$$L_n(x,y) = \begin{cases} 3 & 0.75 \le C(x,y) < 0.8 \\ 2 & 0.58 \le C(x,y) < 0.75 \\ 1 & 0.35 \le C(x,y) < 0.58 \\ 0 & -0.2 \le C(x,y) < 0.35 \\ -1 & C(x,y) < -0.2, C(x,y) \ge 0.8 \end{cases} \tag{41}$$

where *-1* indicates surface contamination, *0* indicates the substrate, and *3* indicates 3 or more graphene layers. Applying this segmentation algorithm to the flattened montage fluorescence image in Figure 6b produces the segmented image shown in Figure 8. In this image, the graphene layers are portrayed using unique colors. The segmented image shows that the graphene sample is entirely single-layer graphene with some easily identifiable cracks and folds that create two-layer graphene. The light blue arrows in Figure 8 indicate regions where large contamination affected the distribution of the dye layer.

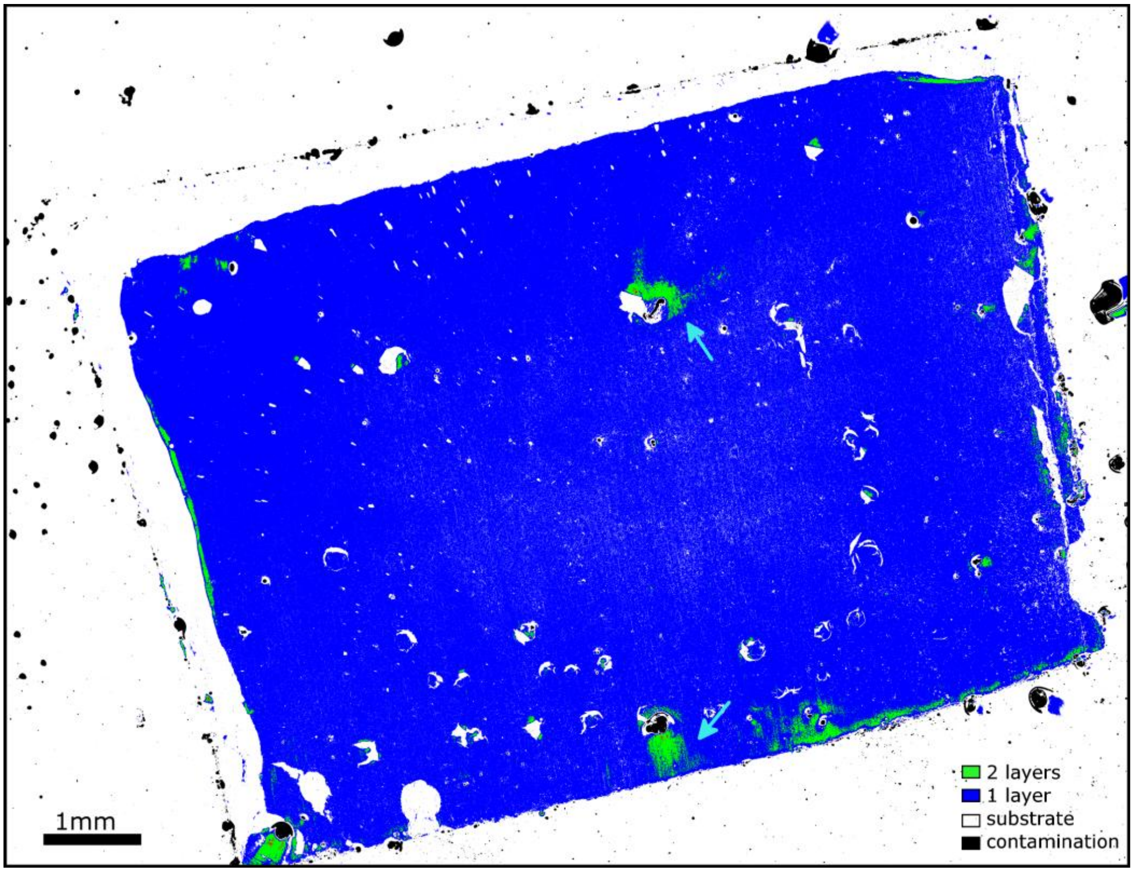

Figure 8 Segmented image of dyed CVD graphene sample showing different graphene layers and surface contamination.

Although quenching contrast is determined by the dye layer thickness, its sensitivity to layer thickness is attenuated by the large contrast between graphene layers. Multiple measurements of a single graphene sheet with different dye layer thicknesses found the quenching contrast of single layer CVD graphene increases from 39% to 74% when the dye layer thickness is reduced from 30nm to 18nm, resulting in an average contrast dependence of ~3%/nm. Alternatively, when the dye layer thickness is increased to 39nm, contrast is reduced to 33%, or ~1%/nm on average. The contrast range of single layer graphene is 35-58%, therefore these results indicate that single layer graphene would be correctly identified for a dye layer thickness within 24-35nm. This is well within the accuracy of the spin-coating technique; therefore contrast sensitivity to thickness does not induce measurement error or impose strict dye layer preparation procedures.

To compare the results of our segmentation algorithm with Raman microscopy measurements, we consider a small region from the large-area fluorescence image where the graphene sample exhibits a large crack and a fold. The fluorescence image of this region is shown in Figure 9a and the segmented image is shown in Figure 9b. In the histogram of the fluorescence image (Figure 9c) intensity ranges mapped to different graphene layers during the segmentation process are indicated. Raman measurements were taken in the areas corresponding to the colored dots in the fluorescence and segmented images. The resulting spectra (Figure 9d) indicate that the graphene sample is mostly single-layer graphene (green dot and spectrum) with two-layer graphene at the fold (blue dot and spectrum) and no graphene in the crack (red dot and spectrum).[40,66,79,92] Profiles taken along the lines in the fluorescence and segmented images are compared to the graphene layer thickness measured by Raman microscopy in Figure 9e. Raman microscopy measurements, indicated by the colored dots in the line profile, agree with the layer thickness identified by the segmentation algorithm. Therefore, Raman microscopy confirms that our segmentation technique accurately measures graphene layer thickness.

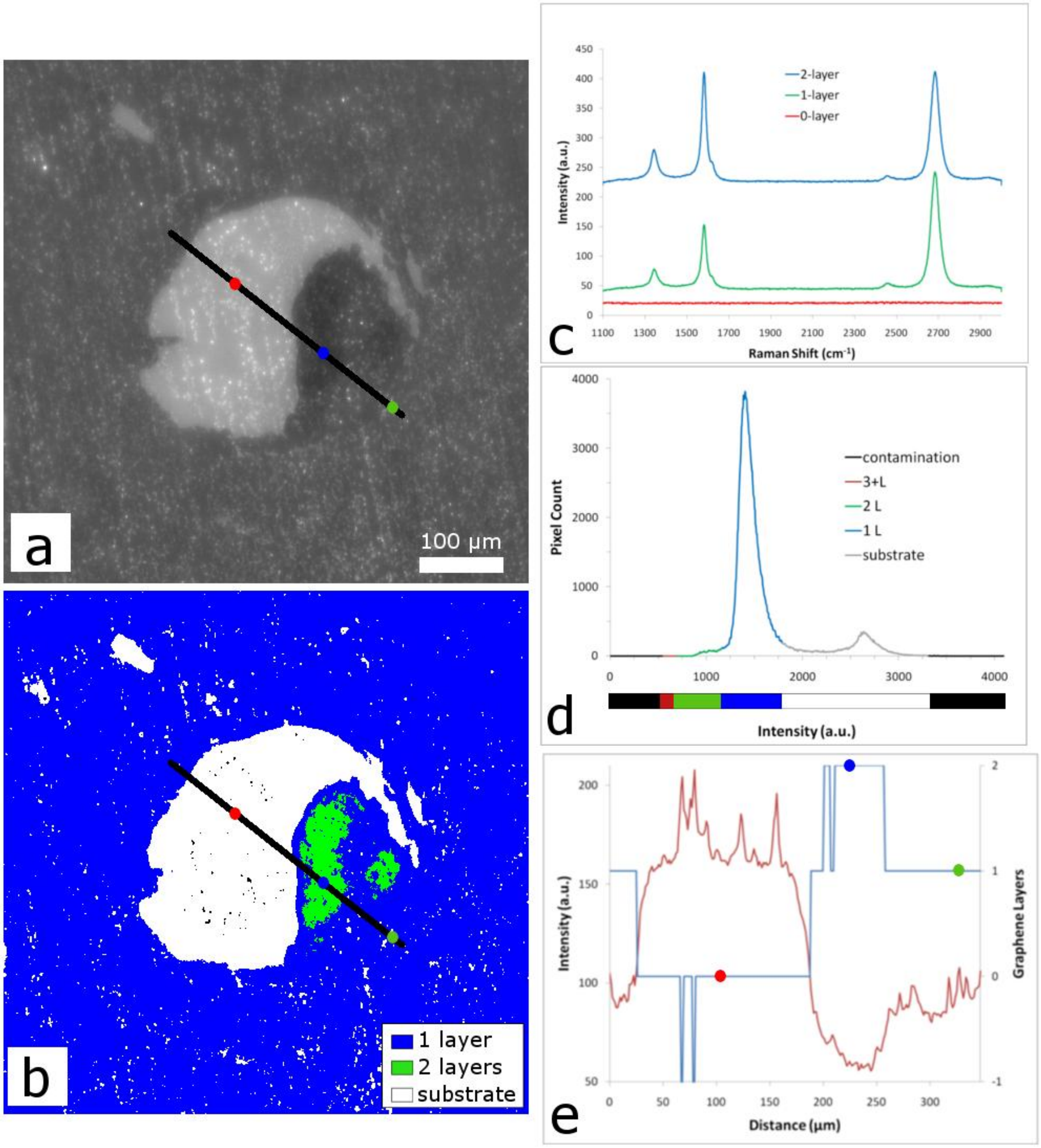

Figure 9 (a) FQM and (b) segmented images of CVD graphene. (c) Raman spectra recorded at colored dots in a and b. Spectra have been offset for visibility. (d) Histogram of FQM image. Colored regions indicate intensity ranges mapped to different graphene layers in segmentation algorithm. (e) Line profile from a and b showing FQM signal (red line), layer count from segmented image (blue line), and layer count from Raman measurements (colored dots).

3.3.1.3 Graphene Quality Comparison

To illustrate the usefulness of this metrology technique for applications such as optimizing graphene growth procedures, we compare the quality of graphene samples prepared using different transfer techniques. An important step in the transfer of graphene is dissolving the cured PMMA layer that is used to protect the graphene during the etching and transfer steps. The basic technique is to completely dissolve the PMMA by dipping the entire sample in acetone.[145] Recently it was shown that the quality of the CVD graphene sample is improved when a drop of liquid PMMA is added on top of the transfer PMMA and allowed to slowly dissolve the transfer PMMA for 30 minutes before the acetone soak.[45] The authors suggested that dissolving the transfer PMMA with liquid PMMA allowed the graphene to relax on the substrate. We propose that similar results can be obtained by adding a drop of acetone instead of liquid PMMA.

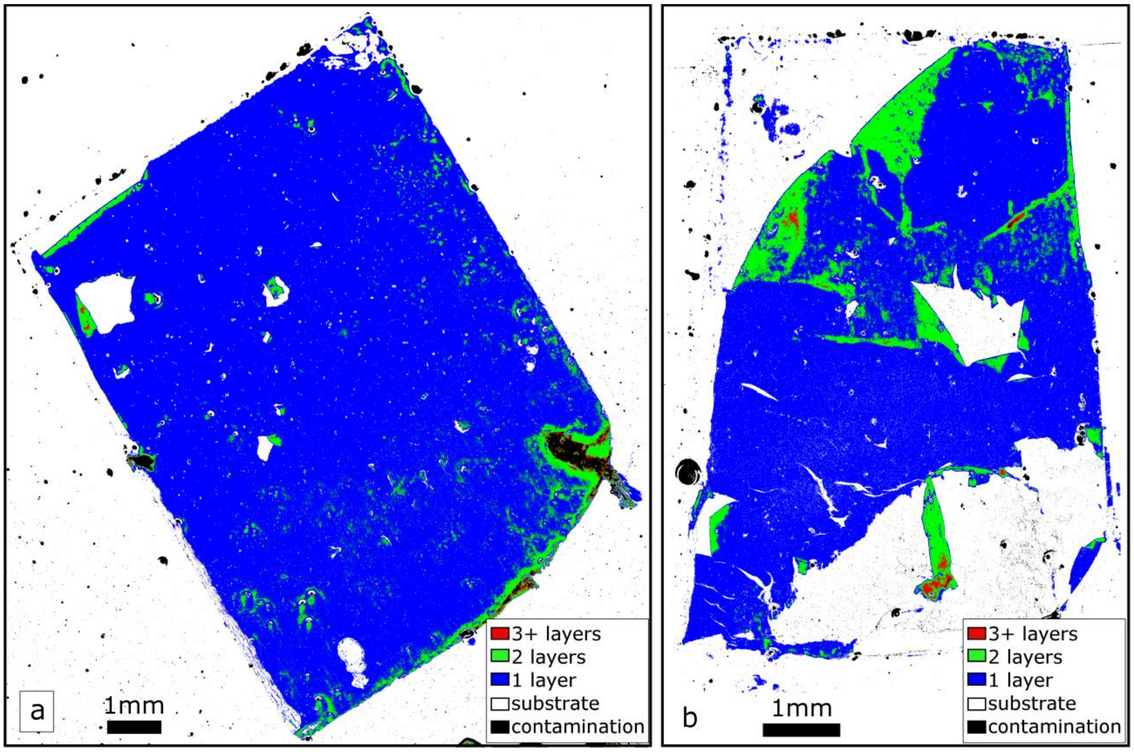

Figure 10 Segmented image of dyed CVD graphene samples prepared using different transfer techniques. (a) Modified technique where a drop of liquid PMMA is added to the transfer PMMA and (b) unmodified technique where the transfer PMMA is directly dissolved by dipping the sample in acetone.

The graphene sample shown in Figure 8 was prepared by adding one drop of acetone onto the transfer PMMA and allowing it to dry for 30 minutes before soaking the sample in acetone. For the graphene sample shown in Figure 10a, we added one drop of liquid PMMA onto the transfer PMMA and allowed it to dry for 30 minutes. As a control, the graphene sample in Figure 5b was prepared by following the unmodified basic transfer technique, where the sample is directly dipped into acetone to dissolve the PMMA. All three CVD graphene samples were grown on the same copper foil substrate and underwent the same etching process. The segmented images of the graphene samples clearly show that the quality of the graphene sample is improved by both the acetone drop and the PMMA drop methods. The presence of numerous folds and large cracks in the sample prepared using the unmodified method indicates that the graphene did not adequately relax onto the substrate and was torn when the transfer PMMA was dissolved in the acetone bath. The graphene samples prepared using the acetone drop and PMMA drop methods are of similar quality. Both samples still contain some cracks and folds, indicating an opportunity for further improvement of the transfer method.

Figure 11 shows 417x318µm^2 sections of each graphene sample which represent ‘good’ and ‘bad’ regions in the samples. The size of these sections is approximately the size of a single image collected using a 20x objective. Although the large-scale images of the graphene samples show that the modified transfer methods produce graphene samples with improved quality compared to the unmodified transfer method, the small-scale ‘good’ images indicate that the samples are all of equal quality. It is easy to see how a comparison that only uses small-scale images could be comparing ‘good’ regions to ‘bad’ regions in different samples, resulting in incorrect conclusions. Therefore, a large-scale metrology technique is required to accurately compare the quality of CVD graphene samples.

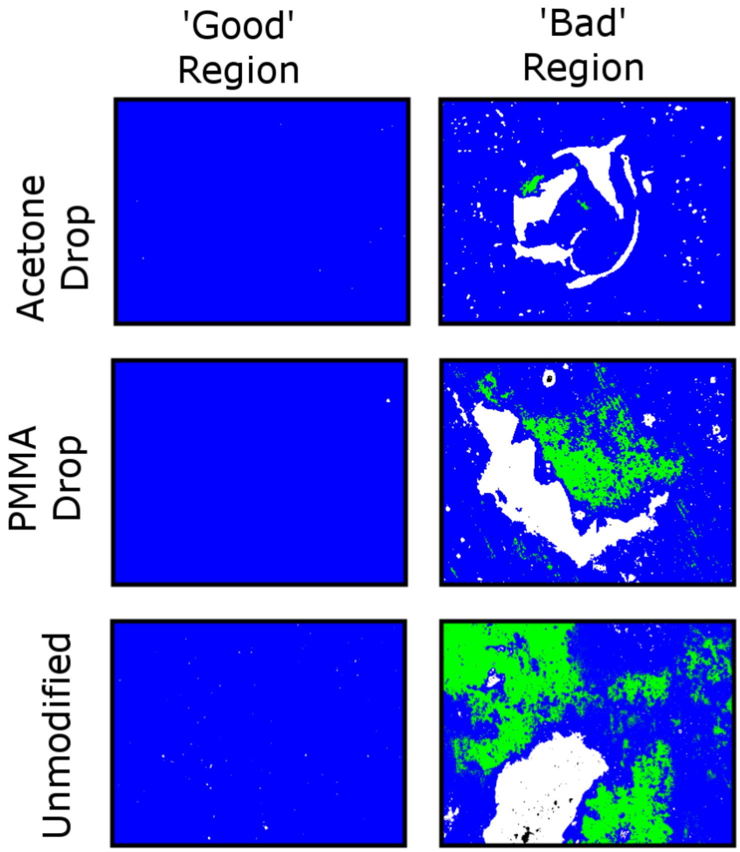

Figure 11 Comparison of different regions in the segmented images of graphene samples. Each region covers a 417x318µm^2 area.

3.3.2 Non-Invasive Visualization of CVD Graphene Doping

In this work we develop an industrial fluorescence quenching microscopy technique for CVD-grown graphene with the ability to visualize chemical doping of large graphene regions quickly and noninvasively. We first perform patterned p-type doping of CVD graphene with fluorine using reactive ion plasma etching, then coat the sample with a DCM dye-doped PMMA polymer solution, creating a fluorescent dye layer. A large-scale high-resolution fluorescence image of the dye-coated graphene sample is collected. In the fluorescence image, doped regions are detected by their reduced quenching compared to pristine graphene. Through Gaussian curve fitting of the fluorescence image histogram, we automatically and dynamically segment the fluorescence image into different graphene regions.

3.3.2.1 Visualization of Doped Regions

Chemical fictionalization of graphene often results in disruption of sp^2-hybridization of carbon atoms, change in Fermi level, and, accordingly, change in the excitation energy of graphene.[146,147] Therefore, we expect FQM to allow identification of chemically doped graphene through reduced quenching.

Fluorine doping of graphene via reactive ion plasma etching has been adopted as p-type chemical doping technique since it allows creation of complex doping patterns through lithography techniques. Previously, CF_4 plasma functionalization of graphene has been introduced as a feasible and more convenient technique to produce fluorine doped graphene.[148] Following the doping procedure outlined in the published study, we doped selected areas of CVD-grown graphene sheets with fluorine. Next, we coated the selectively doped graphene samples with a dye-doped polymer solution. A large-scale high-resolution montage fluorescence image was then obtained and processed.

The FQM images of CVD graphene fluorine-doped using a striped mask to regions of the graphene are shown in Figure 12. Flat-field correction was used to remove the effect of uneven illumination in the individual images and yielded a very uniform large-area image (Figure 12a). In FQM, regions are identified by their contrast relative to the intensity of the unquenched fluorescence in the image histogram. Contrast between two regions in fluorescence quenching is given by

$$C_{2-1} = \frac{I_1 - I_2}{I_1}. \tag{42}$$

when region 1 represents unquenched fluorescence intensity of the dye (over the substrate), contrast is equal to the fluorescence quenching factor of graphene in region 2. To segment the FQM image, pixels are assigned to different graphene regions based on their contrast relative to the background fluorescence intensity peak in the image histogram. In the original FQM image segmentation algorithm, fixed contrast ranges were determined experimentally and applied universally to fluorescence images. In this work, we improve upon the FQM image segmentation algorithm by utilizing Gaussian curve fitting to automatically and dynamically determine the contrast regions corresponding to graphene regions. To perform Gaussian curve fitting, the user enters the rough location of the image histogram peaks and the height, width, and location parameters of the histogram-fitted Gaussian curves are automatically determined. Our algorithm utilizes the ‘fminsearch’ function provided by Matlab to fit the Gaussian curves to the histogram peaks. The ‘fminsearch’ function implements the Nelder-Mead simplex method.[149,150] The Nelder-Mead algorithm is an iterative function-minimization method, in our case employed to minimize the error function measured between the Gaussian curve to be fitted and the image histogram.

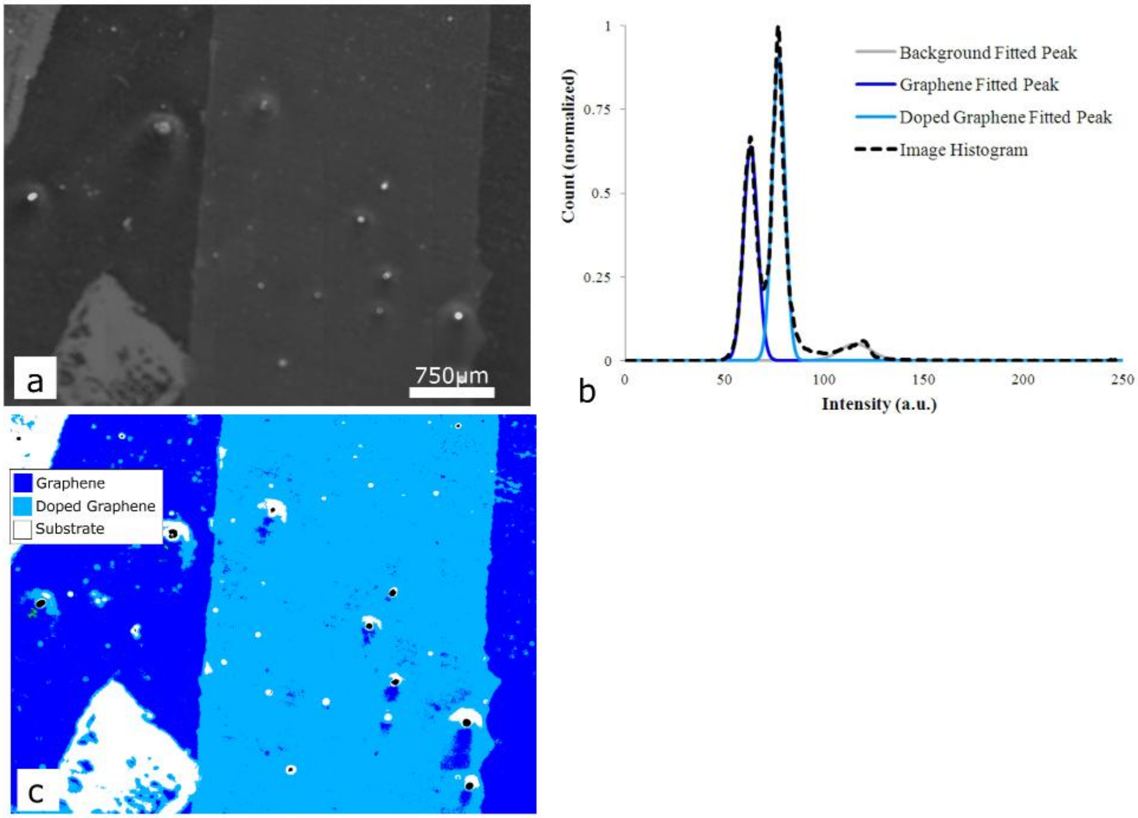

Figure 12 Flat-field corrected fluorescence image of CVD graphene fluorine-doped with a striped mask (a). The fluorescence image histogram and fitted Gaussian peaks corresponding to the substrate (grey), doped graphene (light blue), and pristine graphene (dark blue) (b). Fluorescence quenching metrology segmented image (c) showing the pristine graphene regions (dark blue) and doped graphene regions (light blue).

Image segmentation was performed by mapping pixels within the image to segmented regions according to their intensity contrast relative to background signal, taken as the location of the Gaussian curve fitted to the substrate peak in the image histogram. The fluorescence image histogram and fitted Gaussian curves used to identify graphene regions and segment the fluorescence image are shown in Figure 12b. The contrast ranges corresponding to segmented regions were bounded at the intensity values where the fitted Gaussian curves overlap. The resulting segmented image of the corrected fluorescence image, shown in Figure 12c, identifies regions corresponding to pristine graphene, doped graphene, and the glass substrate, as well as contamination (black). The contrast (*C*) ranges determined from Gaussian curve fitting are:

- $-0.2 \leq C < 0.217$ – substrate,
- $0.217 \leq C < 0.391$ – doped single-layer graphene,
- $0.391 \leq C < 0.58$ – pristine single-layer graphene,
- $C < -0.2$, $C > 0.58$ – contamination

Contrast between pristine graphene and the substrate, measured between the peaks of the fitted Gaussian curves, is 48%. This value is in agreement with the results from the original FQM segmentation algorithm. Contrast between doped graphene and the substrate is reduced to 32% and contrast between doped graphene and pristine graphene is 23%.

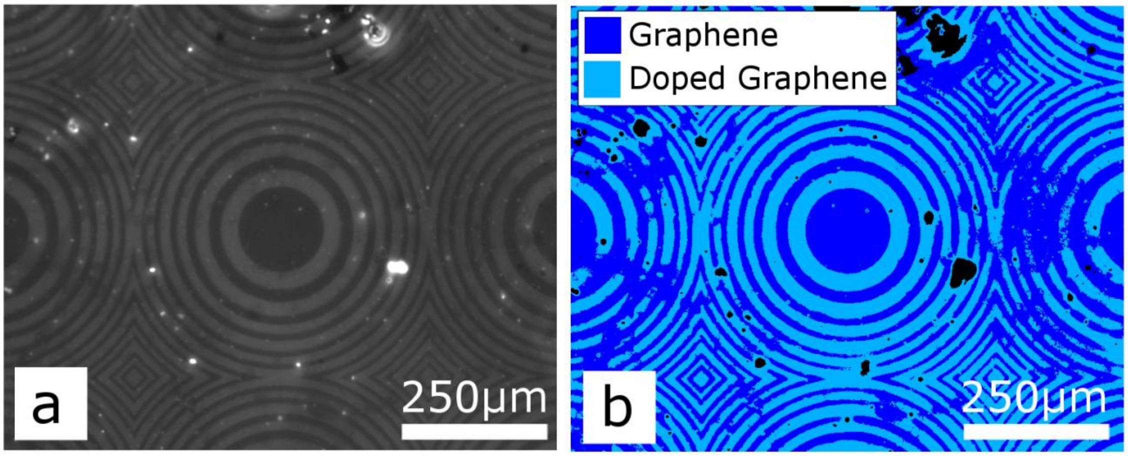

Figure 13 Flat-field corrected fluorescence (a) and fluorescence quenching metrology segmented (b) images of CVD graphene fluorine-doped using a circle mask.

The capability of FQM for visualizing complex doping patterns is demonstrated in Figure 13. The fluorescence image was collected from CVD graphene fluorine-doped using a complex circular photolithography mask. The flat-field corrected fluorescence image is shown in Figure 13a and the segmented image showing doped and pristine regions is shown in Figure 13b. In this sample, contrast between doped graphene and pristine graphene (determined from fitted Gaussian curve locations) is only 17%, a smaller difference than the 23% contrast observed in the CVD graphene doped using the simple striped mask (Figure 12). However, because Gaussian curve fitting is used to automatically determine dynamic contrast ranges, the doped regions are accurately identified in the segmented image (Figure 13b). This demonstrates the significant ability of our FQM technique to dynamically visualize complex doping patterns.

3.3.2.2 Characterizing Fluorescence Quenching

The fluorescence emission of the dye layer over the bare substrate, doped graphene, and pristine graphene is given in Figure 14. The peak emission locations and values are indicated in the figure. In FQM, not all of the fluorophores in the dye layer are quenched by graphene. Therefore, the measured fluorescence emission is a combination of signals from quenched and unquenched fluorophores. As quenching increases, the ratio of quenched fluorophores to unquenched fluorophores increases. The emission peak height attenuation indicates this ratio. Comparing fluorescence emission peak heights, we find that peak height attenuation by doped graphene is 31% of attenuation by pristine graphene. Therefore, while both doped and pristine graphene quench fluorescence emission, quenching is reduced for doped graphene.

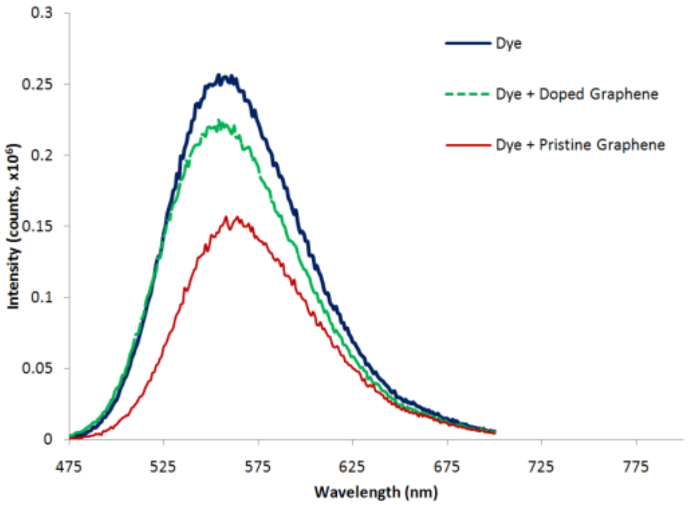

Figure 14 Fluorescence emission of the unquenched dye layer (blue, solid), dye layer over doped graphene (green, dashed), and dye layer over pristine graphene (red, solid).

Peak locations in Figure 14 indicate a blue-shift of the emission peak as fluorescence quenching increases. This behavior is consistent with wavelength-dependent quenching by graphene, proposed in a recent theoretical study. Theoretical calculations indicate that the distance dependence of resonant energy transfer to graphene depends on the ratio between the emission wavelength (λ) and the donor-acceptor distance (d). For $d \ll \lambda$, as is the case in our study, quenching is proportional to (λ^4/d^4).[114] This leads to greater quenching at longer donor-acceptor distances for longer wavelengths. In our sample, where fluorophores are located throughout the depth of the dye-polymer layer, greater quenching at longer donor-acceptor distances leads to greater quenching overall. Therefore, fluorescence emission is quenched more effectively at longer wavelengths, leading to a blue-shift of the quenched emission peak.

A typical Raman spectrum collected from our CVD-grown graphene sheet is shown in Figure 15. The G band, centered on 1580cm^{-1}, is the first-order Raman mode induced by in-plane vibration of carbon atoms in sp^2-hybridized graphene sheets. As a result, the intensity and sharpness of G band signify the presence of crystalline graphitic phase in the synthesized material. The D band at $1335cm^{-1}$ is the defect-originated second-order Raman band which indicates the level of disorder in graphitic sp^2 structures. The nature of this band is related to one-phonon elastic scattering and it is interpreted as a measure of the quantity of sp^3 or dangling sp^2 bonds that are causing structural disorders. The 2D-band at $2600cm^{-1}$, on the other hand, is originated by an inelastic scattering processes that involve phonons. This band is sensitive to the number of layers and is more pronounced in single- to few-layer graphene. The collected Raman spectra verify that the CVD-grown graphene sheet has a very low defect level and is primarily single- to bi-layer.

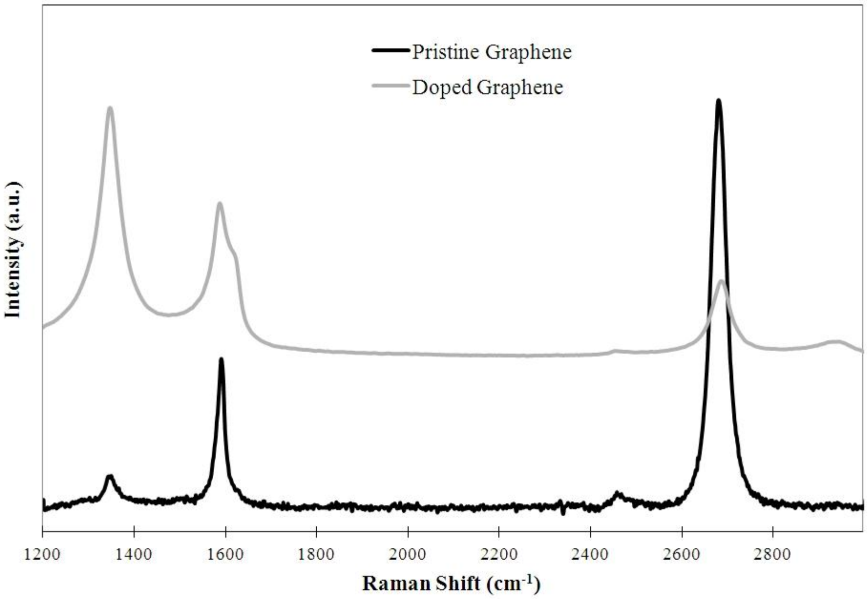

Figure 15 Raman spectra of pristine and fluorine-doped graphene.

Raman bands of graphene can be modified substantially by electron phonon interactions, and therefore, by p- and n-type doping. To further examine the effect of fluorine doping on our CVD-grown graphene, we collected Raman spectra from the fluorine-doped graphene sheet. From Figure 15 it is clear that the intensity of the D peak of fluorinated graphene is much larger than that of the G and 2D peaks. As discussed earlier, the D resonance requires a defect for its activation; hence, its presence is associated with an increased degree of disorder. Several studies on carbon nanotube and carbon bulk materials showed that formation of sp^3 bonds, which are produced from breaking of the sp^2 network in graphene, contributes to an increase in the D peak intensity. Therefore, any type of doping, or process in general, that yields such a "disturbance" in hybridization of carbon atoms would affect the ratio of D band and G band peak intensities, I_D/I_G. The ratio of 2D band and G band peak, $I_{2D}/I_{G,}$ is also susceptible to doping, as it generally reduces 2D band intensity. Thus, while I_{2D}/I_G increases with doping, I_{2D}/I_G usually decreases with doping. This behavior is consistent with our Raman spectrum measurements from pristine and fluorine-doped CVD graphene.

To obtain fluorescence lifetime, we utilized the least-squares method to fit the emission decay data to exponential functions. Collected lifetime decays do not follow a mono-exponential law. As a result multi-exponential mathematical models were utilized to fit the emission decay data.[4]

Figure 16 shows that the measured fluorescence lifetimes consistently follow a bi-exponential damping pattern. The bi-exponential kinetic behavior of the DCM sample in PMMA accords with previous investigations on fluorescence properties of DCM in different solvents and polymer matrices.[151] Weighted averages of decay time for bare glass coated with DCM-PMMA solution is 2.38ns, which is in satisfactory agreement with published results.[151] The average lifetimes for fluorine-doped CVD graphene and pristine CVD graphene are 1.59ns and 2.03ns, respectively.

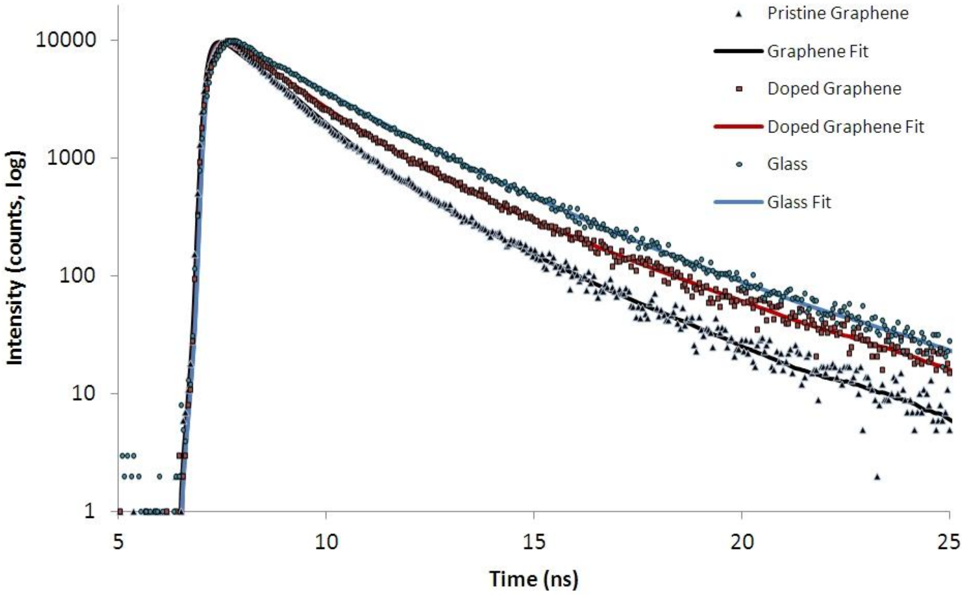

Figure 16 Fluorescence lifetime measurements of DCM dye-polymer layer over bare glass, doped graphene, and pristine graphene substrates.

The degree of fluorescence quenching of the DCM dye is revealed by the decrease in the fluorescence lifetime of samples from dye-coated doped graphene to dye-coated pristine graphene, as the lifetime of the doped graphene sample has increased by 28% over the lifetime of the pristine graphene sample. This reflects the compromise in quenching power of graphene that is caused by fluorine doping. Expectedly, the measured lifetime decays demonstrate an incremental trend from dyed pristine graphene to dyed doped graphene, and finally to dyed bare glass.

3.4 Conclusion

In the first part of this work, we have introduced a large-scale metrology method for measuring the thickness and uniformity of entire CVD graphene samples. This method utilizes FQM to increase the contrast between the graphene layers and the substrate and histogram-based segmentation to identify the graphene layers. Unlike methods based on color contrast created using a Si/SiO_2 substrate, this method does not require calibration but is consistent across different samples and microscopes. The contrast ranges for different graphene layers depends on the dye thickness. In this study, we utilized a dye thickness optimized for few-layer graphene. It is easy to see that this method can be extended to thicker graphene samples by increasing the thickness of the dye layer.

Utilizing the large-scale metrology method described in this work, we have evaluated the effect of different transfer methods. We found that adding a drop of acetone to the sample to dissolve the PMMA layer before dipping the sample in acetone yields graphene samples that are of similar quality to samples where a drop of liquid PMMA was added. Both methods improved the quality of the graphene compared to the basic transfer technique, in which the sample is immediately soaked acetone. Comparing small-scale images of the different graphene samples revealed that these images do not adequately describe the samples and can lead to incorrect conclusions about the quality of the CVD graphene samples.

In the second part of this work, we augment FQM with the ability to accurately visualize doped regions in CVD graphene sheets. First, we successfully show the functionality of large-scale FQM in mapping of fluorine-doped regions in graphene sheets. To determine the method's resolution and scalability strength, we increase the complexity of the doping pattern and successfully reproduce the mapping results. Next, we perform a comparative investigation on steady-state and time-resolved fluorescence parameters of dye coated graphene, fluorinated graphene, and bare glass as control sample. The fluorometry results support the increasing trend observed in quenching level of DCM dye, from control sample to doped graphene to pristine graphene. Finally we improve our image processing technique by employing Gaussian fitting to determine the contrast regions corresponding to graphene regions.

This work introduces a new method for graphene quantification that can quickly and easily identify graphene layers and visualize chemical doping in a large area on arbitrary substrates. This metrology technique is well-suited for many industrial applications due to its repeatability and flexibility.

4 Near-Field Optical Metrology of Cultured Human Cells with Iron Oxide Nanoparticles

4.1 Introduction

Nanomedicine, the application of nanotechnology to treat and diagnose diseases, promises a revolution of medical drug delivery through engineered nanoparticles. The use of nanoparticles to deliver drugs can reduce the amount of the drug that must be administered to reach treatment dosage in target cells and also reduce collateral dosage of surrounding non-target cells.[152] This is achieved by optimizing the characteristics of the nanoparticles, such as size, shape, and surface properties, to maximize their uptake and selectivity. Selectivity, the ability to have a sufficient concentration infiltrate the target cell while avoiding surrounding non-target cells, is an important parameter that determines the efficacy of nanoparticles for drug delivery. Selectivity is best determined by incubating nanoparticles with target and non-target cells and measuring their uptake. Therefore, an important step in the development of nanoparticles for nanomedicine is the detection of nanoparticles within cells. Due to the small size of nanoparticles and relatively large size of cells, detection is difficult with conventional imaging methods. However, because of its excellent optical resolution and sensitivity to scattering, SNOM shows great potential for detecting nanoparticles within cells, thus giving nanomedicine the feedback it needs to develop optimized drug delivery nanoparticles.

SNOM provides essential imaging capabilities that are not available with other imaging methods. The most widely used detection methods are confocal microscopy, flow cytometry, and TEM. All of these methods require compromises that keep them from building a complete and accurate picture. TEM requires that the sample thickness be much smaller than 1µm; therefore, it requires extensive sample preparation and can only image cell cross-sections. Confocal microscopy and flow cytometry overcome the ~250nm optical resolution diffraction limit by requiring that fluorescence labels be attached to the nanoparticles. Although this method allows for detection of nanoparticles anywhere inside the cell, the fluorescence labels change the surface properties and size of the nanoparticles under study, potentially altering the interaction between the nanoparticle and the cell. In contrast, by retaining the high-resolution optical information carried by evanescent waves that decay quickly and are only present when the source or detector are within nanometers of the sample, SNOM is capable of building a picture that is both accurate and complete. When light is transmitted through the cell from the SNOM probe to the detector, high-resolution optical images can be obtained. These images allow for identification of the nanoparticles through their unique optical properties. SNOM has been used to image a wide variety of biological samples including entire cells,[153,154] cell membrane domains,[155,156] and individual molecules,[157] but the technique has not yet been applied to imaging nanoparticles within cells.

The goal of this work is to extend the capabilities of SNOM to identifying iron oxide nanoparticles in cultured human cells using only their intrinsic optical contrast. For this study, our model system was cultured human breast normal (MCF-10A) and carcinoma

(MCF-7) cells incubated with unaltered magnetic iron oxide nanoparticles (γ- Fe_2O_3) and F3 peptide-conjugated iron oxide nanoparticles (Fe_3O_4) labeled with fluorescent tags. To image the cells, we set up our SNOM to illuminate the top of the sample with light emitted from the SNOM probe and detect the transmitted light with a 50x (NA 0.45) collection objective.

4.1.1 Scanning Near-field Optical Microscope

Our SNOM system consists of a MV-1000 scanner head (Nanonics Imaging, Jerusalem, Israel) mounted on the stage of a dual-head microscope (BXFM, Olympus, Japan). The entire microscope system is housed in a custom metal enclosure to eliminate optical noise from the environment and is set on a vibration-isolation table (63-562, Technical Manufacturing Corporation, Peabody, Massachusettes). This system can implement both aperture-SNOM and apertureless-SNOM. Because a large portion of photons interacting with a sample are scattered elastically, we do not require the signal enhancement offered by apertureless-SNOM. Therefore, to minimize the complexity of the SNOM setup and facilitate interpretation of the SNOM signal, we utilize aperture-SNOM imaging.

Light generated at 457nm, 488nm, or 514nm by an argon ion laser (150MSelect, Laser Physics, West Jordan, UT) is coupled into multimode fiber-optic cable (core diameter 50nm), confined in a bent, Au/Cr-coated SNOM probe (Nanonics Imaging) and emitted from a 50nm, 100nm, or 150nm aperture. The probe is scanned over the surface of the sample while the aperture is kept within nanometers of the surface by tappingmode, normal-atomic-force optical feedback control. An x,y,z scanner at the bottom of the SNOM head scans the sample under the tip and adjusts the sample height so the tip traces the surface.

4.2 Methods

4.2.1 Nanoparticle Synthesis

F3 peptide-conjugated dextran-coated iron oxide nanoparticles (Fe_3O_4) were synthesized using a protocol described previously.[158] Briefly, $FeCl_3 \bullet 6H2O$ and $FeCl_2 \bullet 4H2O$ were mixed with dextran (Sigma) in Millipore water. Concentrated aqueous ammonia was added dropwise under vigorous stirring and a steady purge of nitrogen. The solution was then heated at ~70°C for 1 hour and purified. Next, the iron oxide colloid was cross-linked with epichlorohydrin (Sigma) in aqueous NaOH solution for 24 hours. The colloidal solution was then dialyzed against water for 24 hours and filtered through a 0.1-mm-pore-diameter membrane (Millipore). Particles were separated in a magnetic cell sorting (MACS) midi column (Miltenyi Biotec). Small particles that passed through the magnetic column were collected, functionalized with amines by mixing with aqueous ammonia at room temperature for 48 hours, and rinsed with the desalting column (GE healthcare). The F3 peptide (KDEPQRRSARLSAKPAPPKPEPKPK-KAPAKK) with cysteine residue added for conjugation and FITC label was synthesized and conjugated to the aminated particles via the short crosslinker Sulfo-SMCC (Pierce). The resulting nanoparticles were described and characterized previously. Five to ten iron oxide nanoparticles form the core of the nanoparticle, with dextran coating the core, and FITC-labeled F3-conjugated peptide attaching to the dextran. The particle size, determined from SEM imaging, is 50nm while the iron oxide core is approximately 20nm.[158]

Magnetic iron oxide nanoparticles (γ-Fe_2O_3) were used as-purchased from Alfa Aesar. The average diameter for these nanoparticles is 30nm.

4.2.2 Cell Culturing

Human breast epithelial cancer (MCF-7) and normal (MCF-10A) cells were purchased from American Type Culture Collection (Rockville, MD). These cells were grown on thin borosilicate-glass coverslips (Marienfeld GmbH & Co.KG, Lauda-Königshofen, Germany) in cell culture medium in an incubator cabinet that maintained a fixed temperature at 37°C and a humidified atmosphere with 5% CO_2. MCF-7 cells were cultured in Dulbecco's modified Eagle's medium supplemented with 10% fetal bovine serum, 5% penicillin streptomycin glutamine, and 5% sodium pyruvate. MCF-10A cells were cultured in Mammary Epithelial Cell Medium supplemented with 100ng/mL cholera toxin. Once the cells reached the desired confluence (~30%), they were incubated with the nanoparticles.

4.2.3 Cell/Nanoparticle Incubation

For fluorescence-labeled nanoparticles studies, MCF-7 cells were incubated with 40µg/mL F3 peptide-conjugated iron oxide nanoparticles for 30 minutes in the incubation hood. After incubation, cells were washed three times with 1x Dulbecco's phosphate buffered saline (DPBS) and then fixed with 1% formaldehyde for 30 minutes at room temperature. Zeta-potential and confocal microscopy measurements have found that by

30 minutes the MCF-7 cells have already internalized the F3 peptide-conjugated iron oxide nanoparticles. Uptake is thought to occur through nucleolin, which binds to F3, acts as a shuttle protein between the membrane, cytoplasm, and nucleus, and is over-expressed on the MCF-7 cell surface.[158]

For unlabeled magnetic nanoparticle studies, MCF-10A cells were incubated with 50µg/mL magnetic iron oxide nanoparticles for 24 hours. The uptake behavior of these nanoparticles with MCF-10A cells has been studied previously. TEM imaging revealed successful uptake after 24 hours through vesicle formation. A large number of nanoparticles were agglomerated in the vesicles, which were 1-3µm in size.[159]

4.2.4 Image Processing

SNOM images were collected using Quartz Software (Cavendish Instruments Ltd.), which is bundled with the MV-1000 scanner. Images were converted to matrices using WSxM 4.0 Develop 11.2.[160] These matrices were imported to Matlab (Mathworks, Natick, MA) for display and processing.

To calculate the absorption coefficient image, we rearrange the Lambert law for optical absorbance to solve for the position-dependent absorption coefficient, $\alpha(x,y)$

$$\alpha(x,y) = \frac{\log\left(\frac{I_{max}}{I(x,y)}\right)}{z(x,y)} \tag{43}$$

where I_{max} is the maximum measured intensity from light passing through the glass, $I(x,y)$ is the measured near-field transmitted light, and $z(x,y)$ is the measured topography.[161]

The surface angle image was calculated in two steps. First, we calculated the derivatives of the topography image in the *x*- and *y*-directions, *Fx* and *Fy*, respectively, then filtered these images using the lowpass filter, *h*, given by

$$h = \frac{1}{16}\begin{bmatrix} 1 & 1.5 & 1 \\ 1.5 & 2.25 & 1.5 \\ 1 & 1.5 & 1 \end{bmatrix} \tag{44}$$

The surface angle image, S_{angle}, was calculated from the lowpass-filtered topography derivative values, *hFx(x,y)* and *hFy(x,y)* according to

$$X_{angle}(x,y) = \tan^{-1}\left(hF_x(x,y)\right) \tag{45}$$

$$Y_{angle}(x,y) = \tan^{-1}\left(hF_y(x,y)\right) \tag{46}$$

$$S_{angle}(x,y) = \left|X_{angle}(x,y)\right| + \left|Y_{angle}(x,y)\right| \tag{47}$$

4.3 Results

4.3.1 SNOM Transmission Imaging of Human Cells

The purpose of this study is to demonstrate high-resolution, near-field imaging of biological cells and determine the cause of optical contrast in the transmitted near-field image. Optical contrast in near-field imaging of samples with large topographic variations is not necessarily caused by the optical properties of the sample. Because evanescent waves decay exponentially with distance between the probe and sample, the variation in tip-sample separation that results when the tip is scanned over a surface induces an optical signal in the near-field image. This optical signal is independent of the optical properties of the sample and therefore represents an artifact. The artifact in the recorded optical signal due to topography is represented by

$$\left.\frac{\partial S_{NFO}}{\partial z}\right|_{\bar{z}} \cdot \partial z \tag{48}$$

where S_{NFO} is the actual near-field optical signal and z is the height.[21] Therefore, a steep surface slope may cause modulation of the optical signal that is not related to the sample optical properties. To verify the high-resolution imaging capability of our system, which utilizes a bent SNOM probe and normal force feedback, and study the cause of optical contrast in the near-field image, we collected optical transmission images of cultured human breast cells using both constant-gap scanning and constant-height scanning.

Constant-gap scanning is performed with tip feedback engaged and is utilized in SNOM to achieve near-field imaging. Constant-height scanning is performed with the height control disengaged; the height of the tip and sample remain constant. In our experimental setup, the tip aperture was used as the light source in both constant-height and constant-gap imaging. Constant-height scanning requires that the tip be retracted to the maximum height of the sample to avoid collision between the tip and sample. In this experiment, the maximum height of the cell is 17.5μm. Therefore, constant-height scanning produces far-field optical images because the cell surface is outside of the near-field imaging region. Like other far-field imaging techniques, constant-height scanning images are free from near-field topographic artifacts and are also diffraction-limited by the numerical aperture of the imaging objective (0.45 for this study). Theoretically, aperture-SNOM should not allow far-field imaging because all far-field light is confined within the probe.[25] However, scattering by features on the SNOM probe can cause a small percentage of the near-field light to be transformed into far-field light. In this study, a SNOM probe with a 100nm aperture was used and the wavelength of the excitation and detection light was 488nm. Near-field light transmitted through the cell was detected. The resulting images (Figure 17) show high correlation between the constant-gap and constant-height images, while the constant-gap image is higher-resolution than the constant-height image. The increased resolution in the constant-gap image verifies that we successfully achieve high-resolution near-field imaging of thick biological samples. Line profiles (Figure 17d) show that the darker regions in the near-field light correspond to large changes in topography. Therefore, it is possible that the attenuation of light in these regions is caused by topographic artifacts. However, these dark regions are also present in the far-field light, which is immune to the effect of topographic artifacts. Therefore, we conclude that these regions represent effects of the optical properties of the sample and the near-field transmitted signal is free from topographic artifacts.

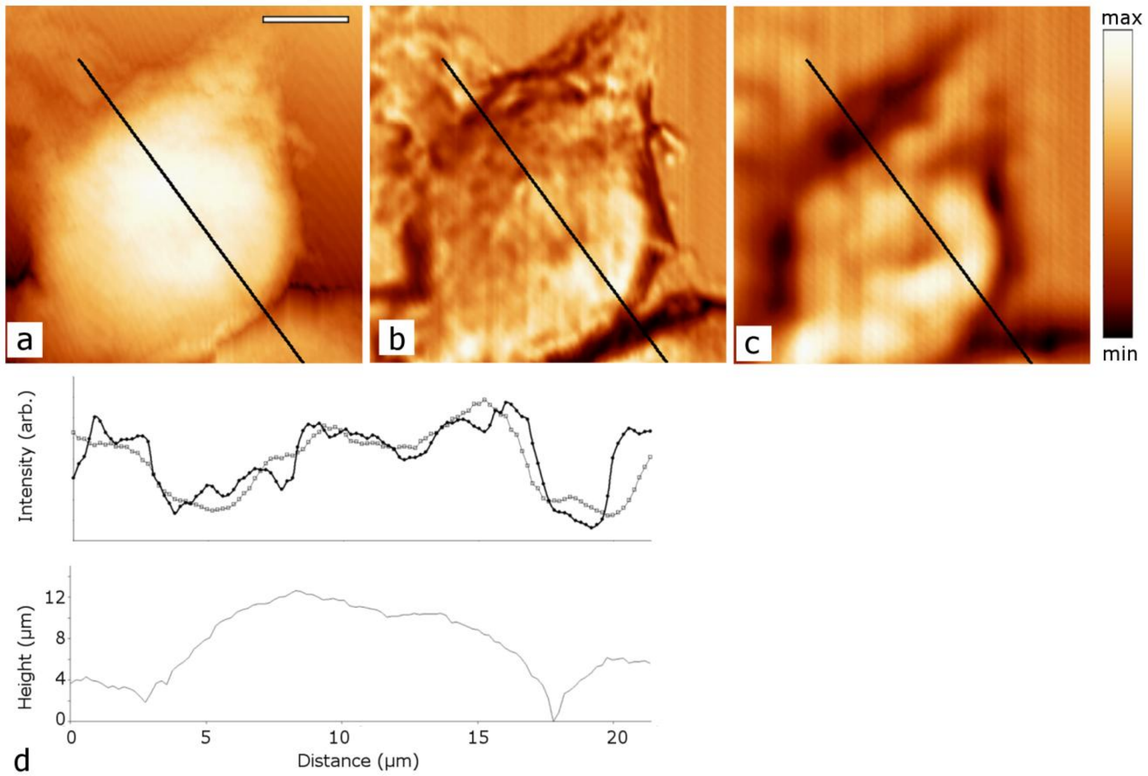

Figure 17 SNOM topography (a), constant-gap near-field (b) and constant-height far-field transmitted light (c) images. Maximum height in the topography image is 17.5µm. Profiles along the black lines are shown in (d) with the height profile on the bottom and the light intensity profiles on the top. Thick black line represents constant-gap near-field light and grey line represents constant-height far-field light. SNOM images collected at a resolution of 159nm^2 per pixel with a 100nm aperture and 488nm light wavelength. Scale bar, 5µm.

There are two possible causes of light attenuation in the darker regions of the transmitted near-field and far-field images. One possible cause is absorption by the membrane. At the cell boundaries, the membrane cross-section is thickest and therefore its effect is greater. The other possible cause for transmitted light attenuation is spectral refraction due to the surface angles. To identify the cause of the contrast, we calculated the surface angle image and the absorption coefficient image from the topography and constant-gap images (see Methods section). Comparing the resulting images (Figure 18) to the transmitted light images (Figure 17b-c) reveals that both the surface angle and absorption images resemble the transmitted near-field and far-field light images. Therefore, neither optical phenomenon can fully account for the light attenuation. Instead, the attenuation is due to a combination of the two effects.

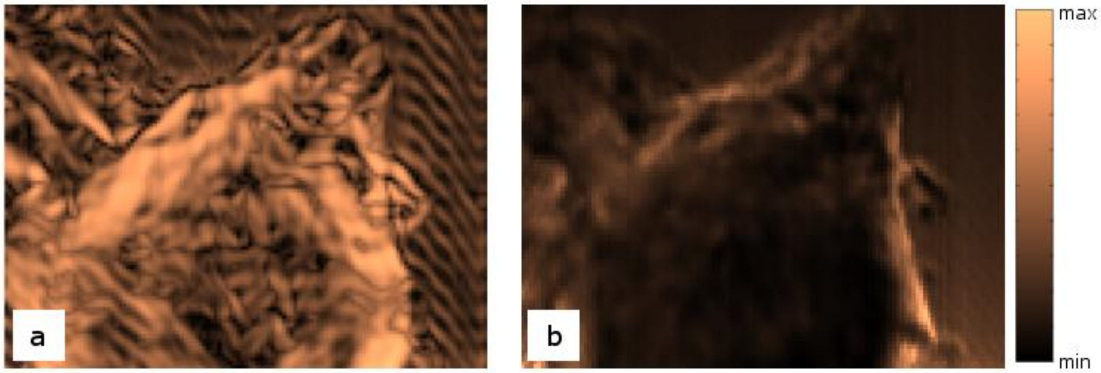

Figure 18 Surface angle (a) and absorption coefficient (b) images calculated from SNOM constant-gap near-field transmission and topography measurements.

4.3.2 SNOM Transmission Imaging of Unlabeled Nanoparticles

To determine the contrast that iron oxide nanoparticles provide with near-field transmission imaging, we imaged unlabeled magnetic iron oxide nanoparticles dried on a glass substrate. In this study, a SNOM probe with a 50nm aperture was used to increase the resolution of the near-field optical measurement. The wavelength of the excitation and detection light was 488nm. Near-field light transmitted through the sample was detected. The unlabeled magnetic iron oxide nanoparticles were diluted with purified deionized water to a concentration of 15.7µg/mL and sonicated for 5 minutes. Agglomeration of the particles was unavoidable because the surface charge density on the uncoated iron-oxide nanoparticles is low. Therefore the electrostatic repulsion is not sufficient to prevent agglomeration and agglomerates consisting of tens of nanoparticles are formed.[162] Our collected SNOM images (Figure 19) reveal iron oxide nanoparticle agglomerates that look like bright spots surrounded by dark rings in the transmitted near-field light. These bright spots are approximately 300nm-wide, as measured in the transmission profile, which is in agreement with an agglomerate of ten nanoparticles.

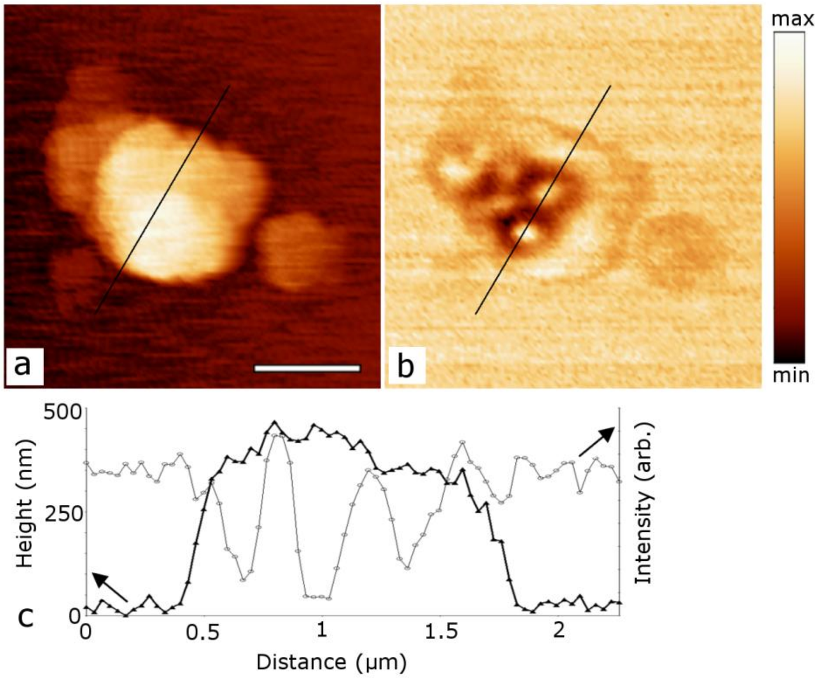

Figure 19 SNOM topography (a) and transmitted near-field light images of iron oxide nanoparticles immobilized on a glass substrate. Maximum height in the topography image is 513nm. Profiles along the black lines are shown together in (c). SNOM images collected at a resolution of 29nm^2 per pixel using a 50nm aperture and 488nm light wavelength. Scale bar, 1µm

4.3.3 Detecting FITC-Labeled Nanoparticles in MCF-7 Cells

Once we determined image formation in SNOM imaging of cells, we were prepared to detect FITC-labeled iron oxide nanoparticles in the MCF-7 cells. In this study, a 150nm aperture SNOM probe was used and near-field light that was transmitted through the sample was detected. For both fluorescence and transmission images, the excitation wavelength was 488nm. In transmission images, a narrow band-pass filter was used to isolate 488nm as the detection wavelength. In fluorescence images, all 488nm-wavelength light was blocked by a narrow notch filter and all the light wavelengths were detected excluding 488nm and wavelengths longer than 650nm (to exclude optical AFM feedback). Fluorescence and transmitted near-field light images of the MCF-7 cells with the FITC-labeled iron oxide nanoparticles are shown in Figure 20. Bright regions in the fluorescence image are at the edges of the cell, indicating that the iron oxide nanoparticles are located mostly at the edges of the cell. This finding is in agreement with confocal imaging, which found most iron oxide nanoparticles near the membrane of the cell when incubated for 30 minutes, the incubation time used for this study.[158] Thus, we conclude that nanoparticles can be identified in biological cells using our SNOM system. Comparing the fluorescence and transmitted near-field images reveals that the bright regions are correlated. This indicates that the iron oxide nanoparticles can be identified in the cells without fluorescence labels by increased transmission compared to the surrounding cell and substrate. We propose this increase in transmitted light is due to an increase in scattering of the incident near-field light by the small (~20nm diameter) iron oxide core of the F3-conjugated nanoparticles. In SNOM, scattering of evanescent waves is required to convert them into propagating waves that reach the detector. Therefore, forward scattering by small particles increases the intensity of light reaching the detector.

The fluorescence and transmitted near-field light images in Figure 20 also provide new insight into image formation with transmission SNOM imaging of cells. The dark regions in the near-field images are somewhat correlated, although the transmission image shows more dark regions than the fluorescence image. Although fluorescence is predominantly an isotropic phenomenon, spectral refraction is directional. Therefore, spectral refraction only affects the transmission image. Thus absorption by the cell membrane is responsible for the dark regions that are seen in the fluorescence image while spectral reflection is responsible for the additional dark regions in the transmission image.

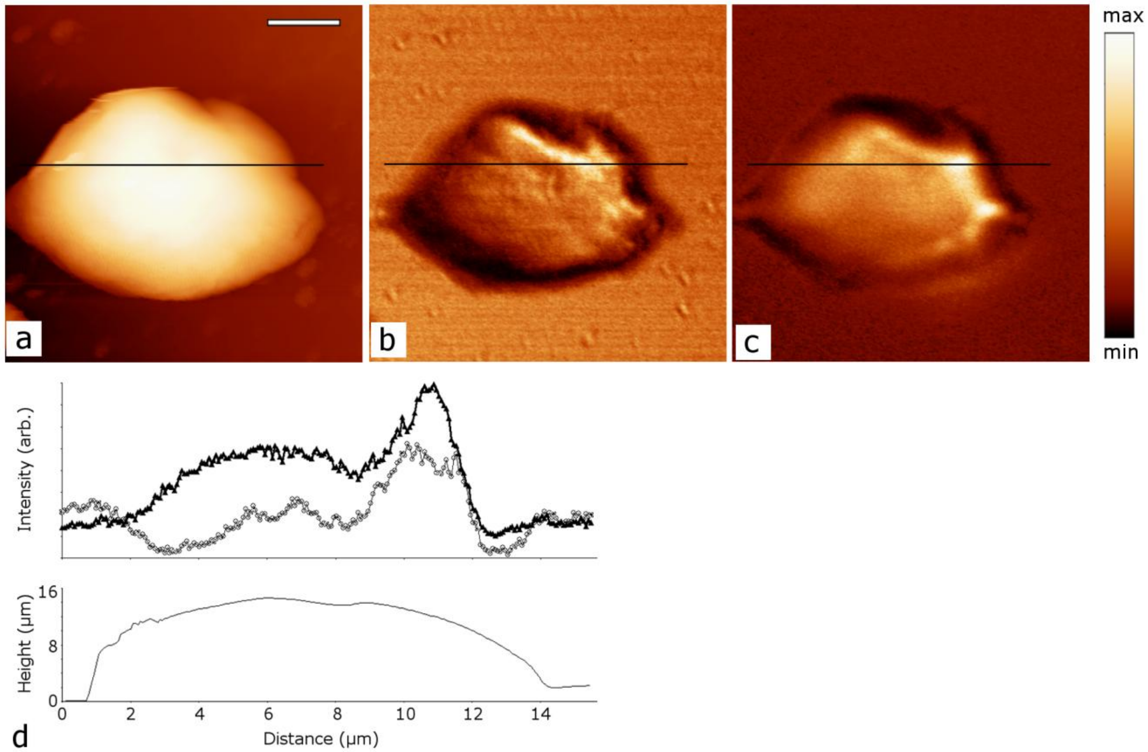

Figure 20 SNOM topography (a) and near-field transmitted (b) and fluorescence optical (c) images of MCF-7 cells containing FITC-labeled iron oxide nanoparticles. Maximum height in the topography image is 16μm. Profiles along the black lines are shown in (d) with the height profile on the bottom and the light intensity profiles on the top. The thick black line represents fluorescence and the grey line represents transmitted light. SNOM images collected at a resolution of 71.5nm^2 per pixel. Scale bar, 4μm.

4.3.4 Detecting Unlabeled Nanoparticles in MCF-10A Cells

The ultimate goal of SNOM imaging of cells and nanoparticles is label-free detection of the nanoparticles within the cells to provide feedback for nanoparticle design and synthesis. A 50nm-aperture SNOM probe was used in this study to provide the maximum imaging resolution and the imaging wavelength was 488nm. Figure 21 shows simultaneous topography (Figure 21a) and transmitted near-field (Figure 21b) images of MCF-10A cells incubated with unlabeled magnetic iron oxide particles for 24 hours. Regions A and B show interesting features in the near-field transmission image, dark circles surrounded by bright rings. These features are not present in images of cells without nanoparticles (Figure 17). Comparing the topography and near-field transmission images in these regions, we find that these features are not correlated to any topographic features, ruling out the possibility that topographic artifacts are the cause of the contrast. Therefore, we conclude these features are caused by unlabeled iron oxide nanoparticles taken into the cell. The approximate diameter of the dark regions of 800nm, while the diameter of the dark regions and bright rings is approximately 1.5-3µm. TEM imaging of iron oxide nanoparticles within MCF-10A cells indicates that large agglomerations of the nanoparticles are formed within 1-3µm vesicles during the uptake process.[159] These large agglomerations would tend to absorb or back-scatter light at the center, as opposed to the forward scattering of dispersed nanoparticles. This phenomenon explains why unlabeled nanoparticles within the cell are identified as bright regions with a dark spot in the middle, as compared to unlabeled nanoparticles isolated on a substrate (Figure 19), which are identified as bright regions.

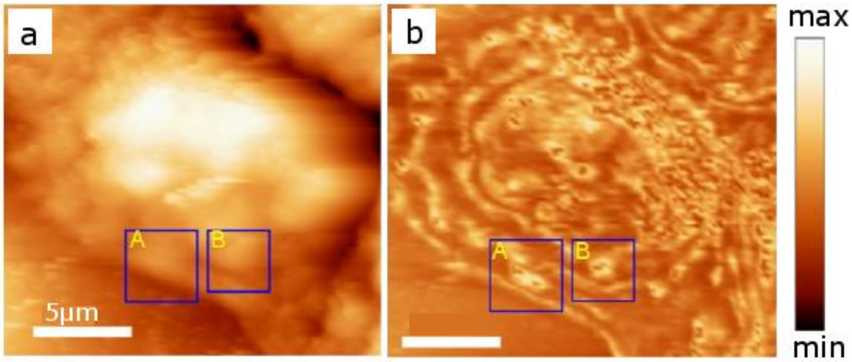

Figure 21 SNOM topography (a) and transmission optical images (b) of MCF-10A cells incubated with magnetic iron oxide nanoparticles for 24 hours. SNOM images collected using a 50nm aperture and 488nm light wavelength. Maximum height in the topography image is 829nm.

4.4 Conclusion

In this work, we have demonstrated successful high-resolution SNOM transmission imaging of cultured cells and shown that the SNOM transmission image is free from topographic artifacts. Attenuation in the transmitted near-field and far-field light is caused by increased absorption of the light in the membrane cross-section at the cell edges and spectral refraction due to surface angle. Further, we have described the scattering contrast of iron oxide nanoparticles incubated with cells. By detecting the signal from fluorescence labels attached to the nanoparticles and comparing it to the near-field transmitted light, we have discovered that F3-conjugated dextran-coated iron oxide nanoparticles near the MCF-7 cell membrane can be detected by looking for regions which are brighter than the surrounding cell. High-resolution SNOM imaging of MCF-10A cells incubated with unlabeled, unmodified iron oxide nanoparticles found that iron oxide nanoparticles were identified as bright regions with a dark center. This dark center is due to back-scattering and absorption in the center of the large nanoparticle agglomeration in the vesicle, formed during the cellular uptake process. This indicates that, while iron oxide nanoparticles can always be identified near the cell surface by bright spots in the SNOM transmission image, large nanoparticle agglomerations will also have dark centers. Therefore, label-free detection of iron oxide nanoparticles in cell requires some knowledge about the dimensionality of the iron oxide formation within the cell.

In this study, we have shown that SNOM can be used to identify iron oxide nanoparticles based on transmission, therefore demonstrating the ability of SNOM to detect iron oxide nanoparticles near the membrane of a cell without requiring any additional labels. This study expands the capabilities of SNOM by developing the abilities to image thick biological samples and to detect inorganic nanoparticles within organic cells. This work also contributes to nanomedicine by introducing SNOM as new powerful tool for studying the efficacy of drug delivery nanoparticles in terms of uptake and selectivity.

5 Near-Field Optical Metrology of Human Tissue

5.1 Introduction

The use of histological stains to study tissue has been practiced for over 200 years. Histological stains are the foundation upon which much of our knowledge of cell biology and histology has been built and are the primary method for tissue diagnostics today. However, over the past 150 years there have been incredible developments in diagnostic imaging technology that introduce the possibility of tissue diagnostics without requiring histological stains or other tissue labels. The benefits of label-free tissue diagnostics justify the study of the intrinsic properties of tissue. The processing required to stain tissue for diagnosis introduces artifacts (e.g. shrinking and tearing) and takes a long time. In many clinical settings, conclusive pathologic diagnosis of tissue is postponed for days due to the time required for tissue processing. This delay means that another surgery is required if a positive margin (cancer cells on the outside edge of the excised tissue) is found in pathologic evaluation. In breast conservation surgeries, positive margins are found in as many as 20%-55% cases.[163] Frozen section analysis (FSA) is currently the only rapid-processing method available with the capability of reporting pathologic diagnosis while a surgery is still ongoing. Because of its capability to reduce additional operations, FSA is widely used in pathologic evaluation of surgical resection margins. However, this method suffers from inaccuracies due to processing artifacts and inconsistent staining, limiting its sensitivity to 78%-91%.[164] Because label-free tissue diagnostics requires no tissue processing, the tissue sample contains no artifacts and can be studied immediately. Additionally, by removing the need for the labels themselves, label-free tissue diagnostics is cheaper and more sustainable. Hematoxylin is a natural stain that is used in the Hematoxylin and Eosin (H&E) tissue-staining protocol that is the gold standard for pathologic diagnosis. Because Hematoxylin is obtained from logwood trees, a limited natural resource, its availability and price vary drastically. Between 2007 and 2008, the price of Hematoxylin quadrupled due to insufficient supply and increasing demand, causing pathology laboratories and stain manufacturers to search for alternatives.[165] Although the shortage only applies to Hematoxylin currently, all other histological stains are also vulnerable to shortage. Therefore, label-free diagnostics is a desired way to ensure a cost-effective method that does not depend on limited natural resources and therefore is sustainable well into the future.

Label-free tissue diagnostics is divided into three major research fields: vibrational spectroscopy, light scattering microscopy, and autofluorescence microscopy. Light scattering microscopy measures variations in the index of refraction and morphology of the tissue by detecting elastically scattered light.[166] Autofluorescence microscopy detects endogenous flourophores which are located primarily in the mitochondria, lysosomes, and extracellular matrix.[167] The two major vibrational spectroscopy techniques are Raman and Fourier transform infrared (FTIR) spectroscopy. While both of these techniques measure the vibrational modes of biomolecules, they differ significantly. FTIR spectroscopy measures the absorption spectrum of tissue by irradiating the sample with light at multiple wavelengths and measuring the light absorption. Raman spectroscopy is performed by irradiating the sample with monochromatic light and measuring the wavelength offset of inelastically scattered light. In this work, we focus on light scattering microscopy for label-free diagnostics.

Label-free tissue diagnostics requires detailed knowledge about the intrinsic optical properties of tissue. Many studies have been performed on the scattering of light from cells, both theoretical[168–170] and experimental.[171–176] These studies focus on the effects of the internal morphology of the cells and variations in refractive indices on light scattering. However, it has been demonstrated that surface morphology greatly affects scattering from the sample.[177,178] Because surface structure can change between different samples of the same tissue, it is necessary to measure the surface structure as well as optical scattering to extract the intrinsic optical properties of tissue.

SNOM is uniquely capable of illuminating the relationship between topography and scattering from tissue. In Table 3, SNOM is compared the methods commonly used to study tissue. While confocal microscopy can measure optical reflection and transmission through the sample, it cannot measure surface structure. Conversely, while AFM can measure the sample topography, it cannot measure the optical properties of the sample. SEM measures topography qualitatively by indicating differences in surface structure but cannot measure actual height and is subject to imaging artifacts, such as electron leakage at edges.[179] Although SEM is capable of resolving very small features, it requires the tissue to be evenly coated with metal and cannot provide any optical information. Only SNOM measures both the optical properties and topography of the sample.[180]

Table 3 Comparison of tissue imaging methods

	Measures Optical Reflection/Transmission (resolution)	Measures Morphology (resolution)	Requires Tissue Processing
Dual-optical SNOM	Yes (50-150nm)	Yes (variable, depends on height)	No
Confocal Microscopy	Yes (250nm)	No	No
AFM	No	Yes (10nm)	No
SEM	No	Qualitative (0.1nm)	Yes

The goal this work is to develop SNOM for measuring the intrinsic optical properties of tissue to contribute to label-free tissue diagnostics. We develop and characterize a novel dual-optical SNOM system and utilize it to study the intrinsic optical properties of human breast epithelial tissue at different hydration states. Specifically, we investigate the effect of surface structure and index of refraction on the scattering of light. Next, we quantify image formation in reflection SNOM through modeling and theoretical analysis to provide the foundation for more sensitive SNOM measurements of tissue optical properties in future label-free diagnostics applications.

5.1.1 Dual-Optical SNOM

Our custom SNOM simultaneously records the transmitted and reflected light as well as the measured sample topography. Dual transmission and reflection imaging has been demonstrated in other SNOM systems in the past,[181–183] but this is the very first system where the optical images are recorded simultaneously and analyzed jointly to extract information about the optical properties of the sample. By comparing SNOM reflection and SNOM transmission images from sequential scans, Kim et. al. were able to extract information from the sample that could not have been detected by just reflection or transmission alone, demonstrating the compounding power of combining SNOM reflection information with SNOM transmission information.[184] Because our system collects these signals simultaneously, we improve upon sequential imaging by removing the position shift that can occur between sequential images and ensuring that the exact same scanning parameters (e.g. tip path) are used with both images. Another benefit of dual-optical SNOM imaging is that it collects both transmission and reflection information in half the time required for a sequential system. Because the time required to obtain one set of information can be well over 1 hour, depending on the scan size and speed, this time reduction greatly improves the efficiency of the SNOM technique. For this study, the optical setup is the same for both the reflection and transmission imaging paths, ensuring extremely high correlation between the experimental parameters used to collect the two optical images.

5.1.2 Scattering in Image Formation

Unlike far-field imaging techniques, near-field imaging is sensitive to only the permittivity of the sample, not the index of refraction.[2] When the permittivity of the surface increases, scattering of the near-field light also increases, resulting in an increase of the far-field intensity collected by the imaging optics.[185] This dependence on scattering to turn near-field light into propagating light causes near-field imaging to be very sensitive to scattering. Once the near-field light is transformed into far-field light, it becomes sensitive to index of refraction. In thick samples, transmitted near-field light is transformed into far-field light, which is sensitive to the index of refraction. Reflection occurs at the sample surface so only near-field light forms the reflection image regardless of the sample thickness. Therefore, reflected near-field light measures the permittivity of the sample surface, while transmitted near-field light measures the index of refraction of the sample. The index of refraction depends on the relative permittivity ε_r and relative permeability μ_r ,

$$n = \sqrt{\varepsilon_r \mu_r.} \tag{49}$$

We assume that the relative permeability does not change in our sample at our imaging wavelength, 488nm. Therefore, the near-field reflection and transmission image formation caused by intrinsic optical properties of the sample is due to variations in the refractive index at the surface (reflection) and throughout (transmission) the sample. Increased index of refraction results in increased collected far-field light intensity.

5.1.3 Optical Properties of Tissue

As light passes through tissue and cells, it interacts with the scattering components of the cell or tissue. These components either scatter light because of their refractive index or because of their morphology. The scattering components of the cell and their refractive indices and dimensions are given in Figure 22 and Table 4.

Figure 22 Scattering components of the cell. (1) Nucleus (2) Mitochondria (3) Cytoplasm (4) Membrane

Table 4 Refractive indices and dimensions of scattering components of the cell

		Refractive Index	Ref.	Dimensions	Ref.
1	Nucleus	1.39	186	3-10μm	175
2	Mitochondria	1.42	168	1-4μm x 0.3-0.7μm	175
3	Cytoplasm	1.37	186	N/A	
4	Membrane	1.46	187	5-10nm	172

5.1.4 Custom Dual-optical SNOM System

To achieve simultaneous acquisition of the reflected and transmitted near-field light, we customized our SNOM system. In our custom dual-optical SNOM, near-field light that has been transformed into far-field light through interactions with the sample is detected by the reflection and transmission optics in the microscope heads (Figure 23). Both microscope heads are equipped with 50x long working-distance objectives (N.A. 0.45), identical filter sets, and similar avalanche-photo diode detectors. The inverted microscope head (transmission optics) uses an Olympus SLMPLN50X objective and the upright microscope head (reflection optics) objective is a Nikon Japan L Plan SLWD. The filter sets each contain two 600nm short-pass filters (Andover 600FL07-25) to block the atomic-force feedback laser and a 488nm narrow-bandpass filter (Semrock LL01-

488-25) to remove autofluorescence from the tissue and fixative. A schematic of the entire custom dual-optical SNOM system is shown in Figure 24.

In most aperture-SNOM setups, the plane of the aperture is horizontal. However, in our setup, the plane of the aperture is at an angle, approximately 20-23° from horizontal (Figure 25a). This angled geometry allows us to measure the axial reflection from the sample and also uniquely allows us to predict topographic artifacts in our near-field images. The theoretical height (Figure 25b) and optical topographic artifact signals (Figure 25c) for our angled tip differ from those obtained with a standard horizontal tip. The asymmetric topographic artifact produced by our tip is at a higher resolution than the surface geometry and is a different shape than the sample geometry. Therefore, this artifact is easier to identify than the artifact produced by a flat tip, which is approximately the same resolution as the sample surface and has a shape similar to the sample geometry.

Images of a calibration sample taken with our custom dual-optical SNOM (Figure 26) show that the reflection signal exhibits features caused by topography variations in the sample surface (peaks and valleys at the rising and falling trough walls). These topographic artifacts are not present in the transmission image. Therefore, we expect topography artifacts to affect only reflection image formation.

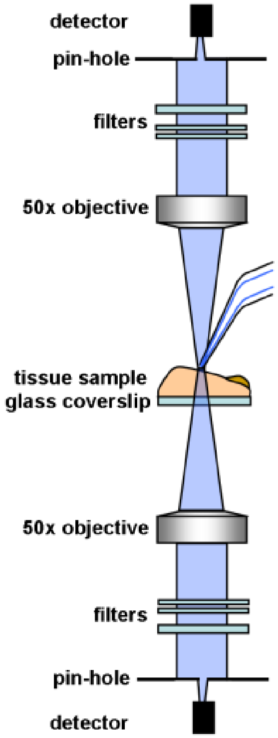

Figure 23 Schematic of the optical collection path of our dual-optical SNOM.

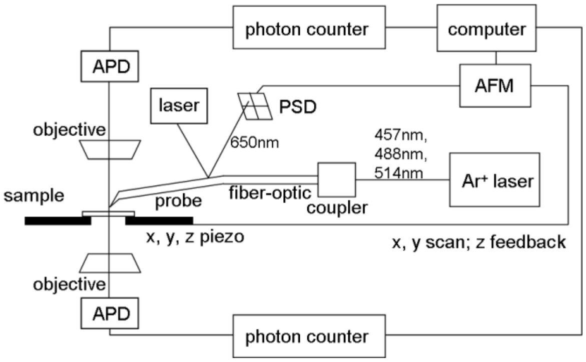

Figure 24 Schematic of our dual-optical SNOM system in aperture-SNOM setup.

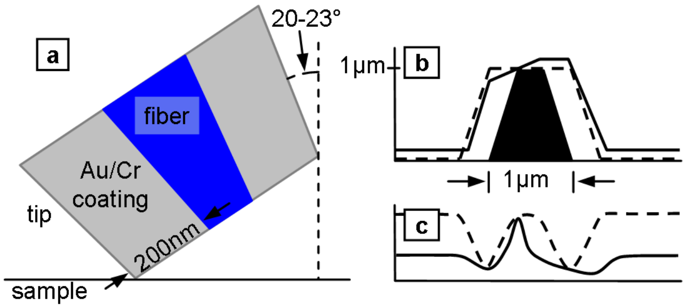

Figure 25 Angled SNOM tip geometry (a). Tip scanning profile (b) for a horizontal tip (dashed line) and our angled tip (solid line) over a 1µm-tall feature. The near-field illumination (c) caused by variation in tip-sample gap.

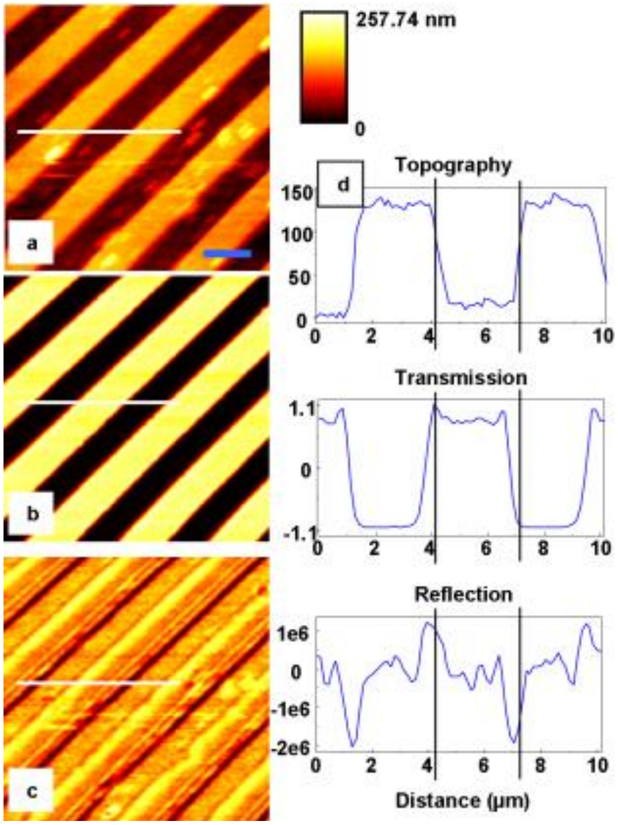

Figure 26 Simultaneous topography (a), near-field transmitted light (b), and near-field reflected light (c) images of a calibration sample taken with our custom dual-imaging SNOM. Scale bar, 3µm. The calibration sample is a metallic mask on a quartz substrate. The line profiles of the three simultaneous images were obtained along the white lines shown in the 2D images. Black vertical lines in the line profiles (d) denote regions correlating to surface trench walls.

5.1.5 Effect of 3D Topography on Image Formation in Reflection SNOM of Tissue

As the SNOM probe scans the surface, different regions of the tip touch the surface due to variations in the surface angle (Figure 27). This leads to a convolved surface that does not exactly match the original surface, with the geometry of the tip greatly affecting the convolved profile. The intensity of near-field light leaving the aperture is approximately uniform in all directions (limited to the half-sphere below the plane of the aperture) but decays rapidly with distance from the aperture. Therefore, the amount of near-field light coupled into the surface is determined by the minimum distance between the aperture and surface, or smallest radius of the half-sphere that represents the emitted light which reaches the surface. Variation in the aperture-surface distance leads to variation in the intensity of light coupled into the sample surface. This modulation of the intensity of near-field light interacting with the surface can easily be mistaken as contrast caused by the optical properties of the sample.

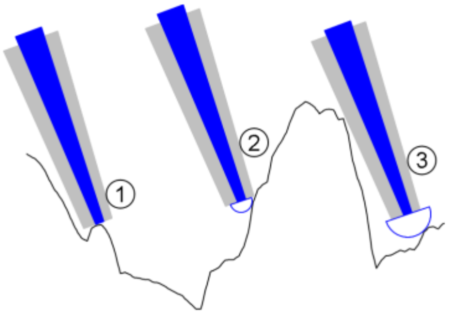

Figure 27 Diagram showing SNOM tip scanning a surface with large topography variations and resulting aperture-surface distance (blue half-circles). In position 1, the tip touches the surface near the aperture, resulting in extremely short aperture-surface distance. In position 2, the leading edge of the tip is touching the surface, resulting in an aperture-surface distance shorter than the distance from the center of the aperture to the edge of the tip. In position 3, the tip touches the surface at the bottom plane of the tip, resulting in a large aperture-surface distance.

5.2 Methods

5.2.1 Human Breast Tissue Acquisition

We collected tissue samples from breast tissue removed during a breast-reduction surgery of an anonymous patient at Loma Linda University Medical Center. The tissue was stored in neutral-buffered 10% formalin (575A-40, Medical Chemical Corporation, Torrance, CA) before the samples were collected. We cut a small specimen from a region of the breast tissue that contained mostly epithelial tissue, embedded the specimen in FSC22 frozen section compound, froze to -32°C, and cut into 5-µm-thick-sections using a cryostat-microtome. We mounted the sections onto prepared coverslips and stored them in formalin at room temperature.

The coverslips used were No. 1 (130-160µm thickness) borosilicate-glass (0111560, Marienfeld GmbH & Co.KG, Lauda-Königshofen, Germany) and we prepared them by soaking them in 1M hydrochloric acid at 80°C for 5 minutes, rinsing with deionized (DI) water then sonicating in DI water (2 changes), 70% ethanol, and 95% ethanol for 5 minutes each. To coat the coverslips, we soaked them in 1mg/mL poly-L-lisine (P4707, Sigma, St. Louis, MO), covered the container, and agitated the container for 30 minutes at room temperature. Finally, we removed the coverslips from the liquid, rinsed them with DI water (10 changes), let them air-dry in a sterile tissue culture hood, and stored them in a sealed container. All water used in this protocol was purified with a Milli-Q A10 purifier (Millipore, Billerica, MA).

To prepare the desiccated tissue sample, we removed the tissue from the formalin and allowed it to sit in a sealed container for over a week before imaging. After SNOM imaging, we collected unlabeled brightfield transmission images in an Eclipse E600 microscope (Nikon, Melville, New York) using a 50x objective (Nikon) and a digital camera (Spot RT, Diagnostics Instruments, Inc., Sterling Heights, MI). Attempts to stain the tissue with H&E were unsuccessful because the stains did not show adequate differentiation between the nuclei and the cytoplasm and the tissue structure was altered severely in the staining process.

For non-desiccated tissue sample imaging, immediately before the tissue was imaged we removed the tissue from the formalin, dipped the tissue in two changes of phosphate buffered saline (D8537, Sigma-Aldrich, St. Louis, MO), and then dipped the tissue in DI water. We let the tissue dry for 15 minutes and then began SNOM imaging in air, completing imaging within 1 hour of removing the tissue from the formalin. As soon as SNOM imaging was completed, we stained the sample with Gill No. 2 Hematoxylin

(GHS216, Sigma-Aldrich) and Eosin Y (HT110116, Sigma-Aldrich) and mounted it onto a standard microscope slide. We collected images of the H&E-stained tissue using the same microscope and setup utilized to collect the brightfield images of the desiccated tissue.

The tissue used to quantify image formation in reflection SNOM imaging of tissue was prepared by sputter-coating desiccated tissue with a mixture of gold-palladium (40:60) four times, each time placing a different corner at a 45° angle to the source, for 50 seconds each time.

5.2.2 Image Processing

SNOM images were collected using Quartz Software (Cavendish Instruments Ltd.), which is bundled with the MV-1000 scanner. Images were converted to matrices using WSxM 4.0 Develop 11.2.[160] These matrices were imported to Matlab (Mathworks, Natick, MA) for display and processing. Line profiles were created using a custom Matlab script. Using another custom Matlab script, we registered the H&E-stained images to the SNOM images by manually selecting landmarks and calculating the linear transformation of the H&E-stained image.

The mean and variance of the SNOM samples were calculated using standard Matlab functions, which are based on the equations:

$$x_{mean} = \frac{1}{n}\sum_{i=1}^{n} x_i \tag{50}$$

$$x_{var} = (x^2)_{mean} - (x_{mean})^2 \tag{51}$$

5.2.3 Scanning Simulation

To simulate the tip scanning over the sample surface, we developed a custom algorithm using Matlab. In this script, we first defined the bottom edge of the tip then at each calculation point (pixel from the source image), we had the algorithm lower the tip until any point on the tip reached a point on the sample surface. This convolution method has been used before to determine the quality of AFM measurements.[188] The tip geometry is defined as a 150nm-wide aperture with 200nm metal coating, resulting in a tip surface 550nm-wide. The tip is either oriented vertical (tip surface horizontal) or 20° from vertical.

To calculate the smallest aperture-surface distance, we compare the original surface to the convolved surface. The tip-scanning diagram in Figure 27 shows that the x,y-coordinates of the portion of the surface with the smallest aperture-surface distance can be offset from the x,y-coordinates of the aperture. Therefore, for every point in the convolved surface, we measure the distance to the aperture for each point on the original surface within the half-sphere region representing the allowed distribution of light. The minimum distance to the aperture, which is measured as the spherical radius ($r^2=x^2+y^2+z^2$), is then recorded for that point on the convolved surface.

5.3 Results

5.3.1 Analysis of Light Scattering from Human Tissue

The purpose of this study is to compare near-field reflection, near-field transmission, and topography images collected using our custom dual-optical SNOM to reveal the cause of variation in scattering from human breast epithelial tissue due to dehydration. By comparing simultaneously-acquired topography and optical SNOM images, we separate the effects of morphology from the tissue's intrinsic optical properties.

5.3.1.1 Desiccated tissue

Simultaneous SNOM images, obtained with a 150nm aperture SNOM probe at 488nm excitation and detection wavelengths, and a brightfield transmission image of the desiccated tissue are shown in Figure 28. SNOM images were collected by mapping the 10.1μm^2 region into 256x256 pixels with an 8μs dwell time per pixel. The brightfield transmission image (Figure 28d) shows refraction of the broad-spectrum light due to the sample's surface morphology (Figure 28a). This effect of surface morphology is also shown in the SNOM transmission image (Figure 28b), but with higher resolution. For our system, where λ=488nm and NA=0.45, the far-field resolution limit (Equation 27) is 542nm. The resolution in the SNOM reflection image, measured using full width half maximum (FWHM) as shown in the reflection line profile, is 197nm, just less than 150nm, the theoretical resolution for imaging with a 150nm aperture (Equation 29). This represents a 64% improvement over far-field resolution. However, the resolution in the

SNOM transmission image is only 354nm. This decrease in resolution is due to two phenomena: scattering within the tissue and minimum feature size.

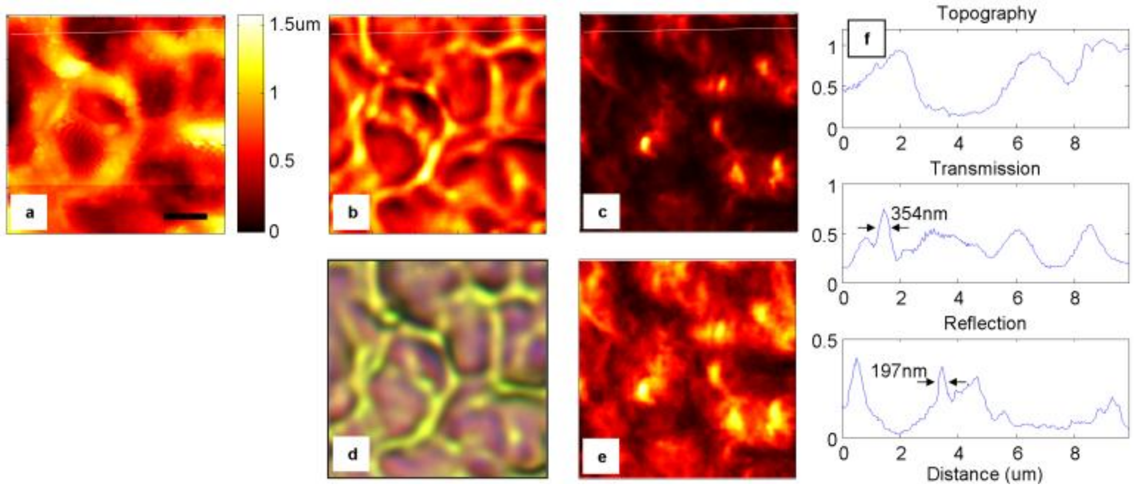

Figure 28 Simultaneous topography (a), transmitted near-field light (b), and reflected near-field light (c) along with transmitted brightfield light (d) and scaled reflection (e) images of unlabeled human breast epithelial tissue. The line profile (f) along the white lines in the SNOM images shows resolution using FWHM of reflection and transmission peaks uncorrelated with topography. SNOM images collected at a resolution of 39.4nm^2 per pixel with an 8µs dwell time per pixel. Scale bar, 2µm.

Because our sample exhibits large topographic variations, it is necessary to address the problem of topographic artifacts. The maximum height variation in the tissue sample is 1.6µm. This requires that the tip be scanned along the surface in constant-gap mode to keep the surface in the near-field region. Constant-gap mode is subject to topographic artifacts due to variations in the gap between the aperture and the sample surface as the tip is scanned over the sample.[21,189,190] One way to verify that the constant-gap optical image is not dominated by artifacts is by confirming that variations in the optical image are uncorrelated to topography variations.[189] Line profiles from the SNOM images of desiccated tissue (Figure 28f) show transmission and reflection signals that are uncorrelated with the topography. However, the near-field reflection image (Figure 28c) exhibits intensity peaks that are correlated to valleys and falling slopes (when measured left to right) in the topography (Figure 28a). The peaks in the falling slopes are exponentially more intense than the peaks in the valleys. Results from multiple scans of the surface where the detector position was changed very slightly show the location of these peaks changing between scans. This phenomenon has been seen experimentally and modeled theoretically for samples exhibiting topographic variations as small as 180nm. It is a topographic artifact arising from variations in the tip-sample gap and indicates a sharp, undamaged scanning tip.[191] To reduce the effect of these topographic artifacts in the reflection image, we calculate a scaled reflection image using

$$R_{scaled} = \log(R + 0.1) \tag{52}$$

where R is the reflection signal, also scaled so that the minimum value is 0 and the maximum value is 1. The logarithmic transform given by Equation 52 decreases contrast at higher intensities and increases contrast at lower intensities. Because the topographic artifacts at the falling slopes are exponentially brighter than the true optical signal, they fall within the higher-intensity region, where contrast is decreased. The true optical signal falls within the lower-intensity region, where contrast is increased. Because this transformation does not invert the contrast in the image, the rule that increased scattering by the sample causes increased image intensity is maintained. Where the topography indicates presence of tissue in the SNOM images of desiccated tissue, the scaled reflected signal (Figure 28e) diminishes. Therefore, we conclude that the scaled reflection image is primarily formed by the true optical signal and the effect of the topographic artifacts at the falling slopes is greatly attenuated compared to the original reflection image.

A 3D representation of the SNOM images (Figure 29b) allows for more detailed evaluation of the effects of topographic artifacts. The white arrows show regions where transmission (ridge, upper arrow) and reflection (valley, lower arrow) deviate from any patterns correlating the optical signals to topography. The transmission signal exhibits peaks where the topography indicates ridges (upper white arrow), at the top of the rising/falling slopes as well as along the flat surface of the ridge. The scaled reflection signal is bright both at the valleys, and partway up the rising and falling slopes (lower white arrow). However, topographic artifacts would cause increased transmission/reflection only at the top of the rising slope. Therefore, artifacts do not dominate our SNOM images of tissue, despite the large topographic variations. Furthermore, the change in index of refraction of the surface is measured even where tip-surface convolution causes the measured topography to deviate from the true sample surface.

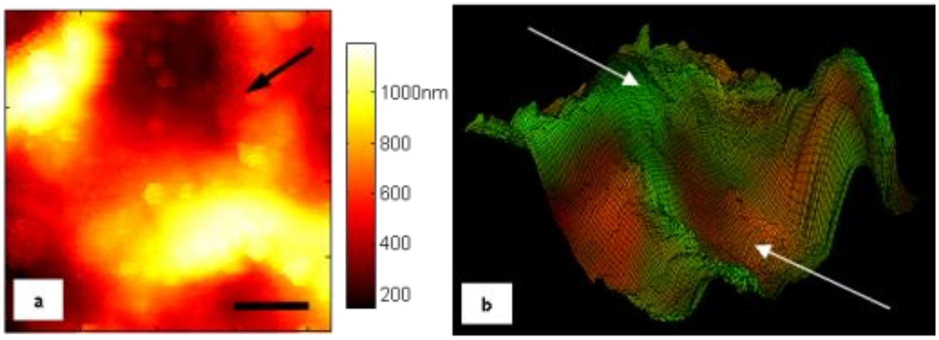

Figure 29 Small region from tissue SNOM images. Topography is represented as intensity (a) and as a 3D surface (b). The black arrow in (a) shows the viewing angle for the 3D surface. Scale bar, 1µm. Scaled reflected near-field light is represented on the 3D surface as a color overlay (red) along with transmitted near-field light (green). In the 3D view, the grid shape indicates the surface topography.

5.3.1.2 Non-desiccated tissue

Simultaneous SNOM images of the unstained tissue, obtained with a 150nm aperture SNOM probe at 488nm excitation and detection wavelengths, and brightfield transmission images of the same tissue stained with H&E are shown in Figure 30. SNOM images were collected by mapping the 57.5µm^2 region into 390x390 pixels with a 7µs dwell time per pixel. The maximum height variation is 3µm. This height variation is double the variation in the desiccated sample, and accordingly the topographic artifacts are more apparent in the reflection image. The effect of these artifacts is not seen in the transmission image (Figure 30b) and is reduced in the scaled reflection image (Figure 30e).

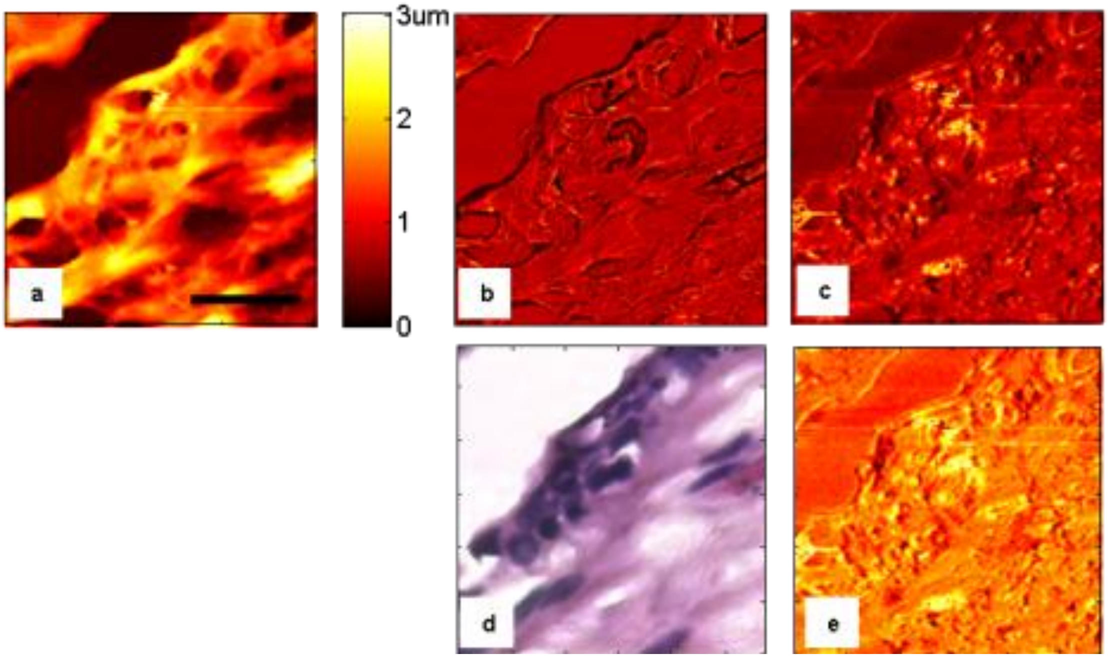

Figure 30 Simultaneous topography (a), transmitted near-field light (b), and reflected near-field light (c) images of unlabeled human breast epithelial tissue compared to brightfield image of the same region after H&E staining (d) and scaled reflection image (e). SNOM images collected at a resolution of 147.5nm^2 per pixel with a 7µs dwell time per pixel. Scale bar, 20µm.

5.3.1.3 Discussion

Comparing SNOM images of the desiccated and non-desiccated tissue reveals a contrast inversion between the near-field reflection images. Regions where topography indicates tissue in the non-desiccated sample are brighter than regions corresponding to bare glass. Conversely, darker regions in the reflection image of the desiccated tissue correspond to areas where topography indicates tissue. To determine the effect of internal morphology and refractive indices on the contrast, the glass, cytoplasm, and nuclear regions of the SNOM images must be studied separately. Inspecting the SNOM images of non-desiccated tissue by eye, even when zoomed into a small region and the nuclei are outlined (Figure 31), it is difficult to tell the difference between the nuclei and the rest of the tissue. However, average intensity values calculated from 2.36µm^2 regions corresponding to glass, cytoplasm, and nuclei (Figure 31d) indicate variations in the reflected and transmitted light from the different regions (Table 5). Because H&E staining of the non-desiccated tissue is not possible, the tissue components cannot be differentiated in the SNOM images. Even so, interesting conclusions can be drawn from average intensity values calculated from 1.18µm^2 regions corresponding to the substrate and tissue (Table 6). The regions used in the calculations are shown in Figure 32.

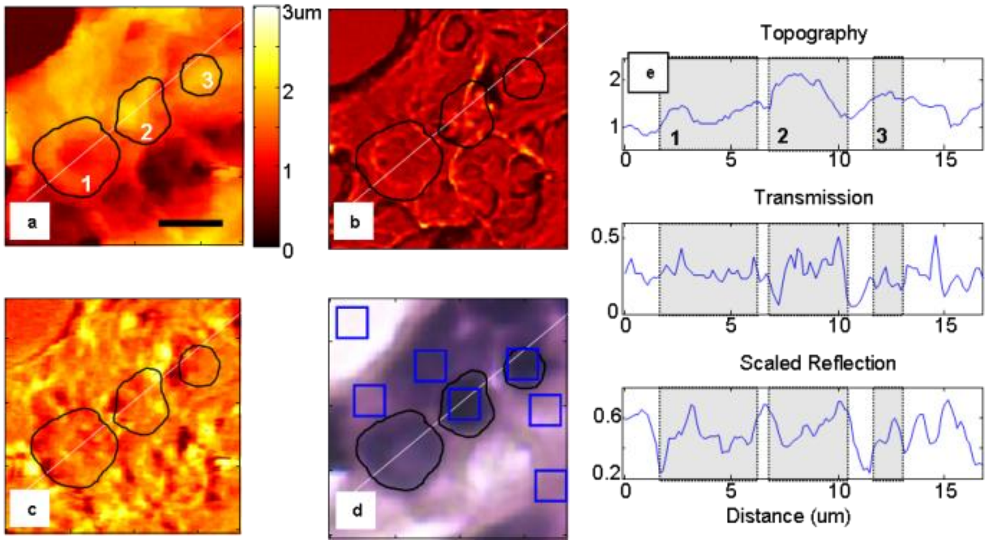

Figure 31 Simultaneous SNOM topography (a), transmission (b) and scaled reflection (c) images and brightfield image of the same region after H&E staining (d). Scale bar, 5µm. Nuclei are denoted by black outlines and are portrayed as grey regions in the line profiles (e). Regions used for measuring statistical values are outlined with blue rectangles in H&E-stained image.

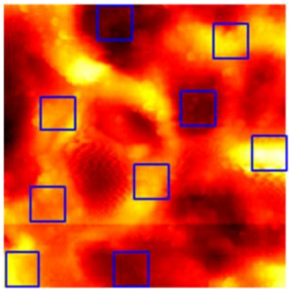

Figure 32 Regions used for measuring statistical values of desiccated tissue outlined with blue rectangles over SNOM topography image.

Table 5 Measured statistical values from 2.36µm^2 regions in SNOM images of non-desiccated tissue

	Transmission (mean)	Reflection (mean)	Topography (mean, nm)	Topography (variance, nm^2)
Glass	0.2619	0.4436	359	338
Cytoplasm	0.2453	0.5500	1128	90825
	0.2301	0.4971	1678	3720
	0.2485	0.5455	1735	6740
Nucleus	0.2883	0.5676	1741	18132
	0.2677	0.4857	1807	24648
	0.3070	0.5250	1872	39211

Table 6 Measured statistical values from 1.18µm^2 regions in SNOM images of desiccated tissue

	Transmission (mean)	Reflection (mean)	Topography (mean, nm)	Topography (variance, nm^2)
Glass	0.4521	0.5108	195	1586
	0.3252	0.4453	281	1489
	0.4357	0.3563	319	1257
Tissue	0.5577	0.2958	832	4328
	0.4130	**0.2156**	**990**	**16992**
	0.5682	0.2323	910	7006
	0.5557	0.1898	927	6480
	0.4493	**0.2579**	**1086**	**11571**
	0.2653	**0.1015**	**1258**	**40677**

Scattering in tissue depends on the tissue surface morphology, tissue internal morphology (packing and geometry of small scatterers), and variations in refractive indices.[177,192] Tissue surface morphology is measured by the topography variance. The mean reflected and transmitted near-field light from the regions measured in the non-desiccated tissue (Table 5) are not related to either the variance of the topography, therefore we conclude that tissue surface morphology does not affect the scattering from the non-desiccated tissue. In the desiccated tissue, the mean near-field transmission does depend on the topography variance for high variance (indicated in bold, Table 6). For low variance, transmission is independent of topography variance. To focus on the effect of refractive indices and internal tissue morphology, the regions where transmission is dependent on topography variance (bold, Table 6) are excluded from the following discussion.

Average intensity measurements from the non-desiccated tissue (Table 5) indicate that the nucleus and cytoplasm reflect more light than the substrate. However, the indices of refraction of the tissue components (cytoplasm: n=1.37, nucleus: n=1.39, membrane: n=1.46, Table 4) are closer to the index of refraction of the surrounding air (n=1 [24]) than the glass coverslip (n=1.52, from manufacturer). According to SNOM image formation theory, this should lead to less scattering from the tissue than from the glass. The index of refraction of water (n=1.33 [24]) is actually closer to the index of refraction of the surrounding air than the tissue components. Therefore, less light would scatter from the water than the tissue, as observed in the SNOM images. We conclude that some of the water used in the rinsing step immediately preceding imaging of the non-desiccated sample was still present on the hydrophilic poly-L-lysine-coated glass slide during imaging. This thin film affects the near-field reflection image, which is sensitive to refractive indices of the surface, but does not affect the near-field transmission image, which is sensitive to refractive indices throughout the depth of the sample.

The results in Table 5 indicate that more light is transmitted through the nucleus than through the glass while less light is transmitted through the cytoplasm. The nucleus and cytoplasm have very similar refractive indices when compared to glass or water. Also, the surface roughness, quantified from the variance of the topography (Table 5), of these regions is very similar. Therefore, this variation in transmission is due to internal morphology. Scattering in non-desiccated tissue cytoplasm is caused by small organelles, such as mitochondria, which predominately backscatter due to morphology. In contrast, the scatterers in the nucleus are evenly distributed, resulting in forward scattering.[171] In the desiccated tissue, transmission is increased and reflection is decreased in the tissue compared to the substrate (Table 6), therefore both the nucleus and cytoplasm cause forward-scattering. Because the nucleus is composed mostly of nonvolatile proteins, it is not affected by desiccation.

Therefore, mitochondria are evenly distributed in the cytoplasm, which is caused by dense packing of the mitochondria in the desiccated tissue and results in reduced scattering in desiccated tissue compared to non-desiccated tissue. Far-field optical studies have found that desiccated tissue scatters less than non-desiccated tissue[192,193] and that compressed tissue, where mitochondrial are tightly packed in the cytoplasm, also scatters less than non-compressed tissue.[192] When combined, these studies suggest that dense packing of the mitochondria in desiccated tissue causes the reduction in backscattering.

5.3.2 Quantifying Image Formation in SNOM Reflection Imaging of 3D Samples

To extend the capability of dual-optical SNOM to more sensitive measurements of the intrinsic optical properties of tissue, image formation in the reflection SNOM image needs to be well understood. Therefore, in this study we quantify image formation in the reflection image using modeling and theoretical analysis. The tissue sample used in this study is coated with a homogeneous gold-palladium film to remove any variations in optical properties of the sample. This allows us to identify and characterize topographic artifacts in the reflection SNOM image. In this study, we focus on the two factors that cause topographic artifacts: the path of the SNOM probe as it is scanned over the surface and the distance between the aperture and the sample surface.

We used AFM measurements of the tissue surface with a 50nm vertical AFM tip as the ‘actual’ sample surface. Although SEM measurements of the surface are higher resolution and do not display even the minimal tip-sample convolution found in the AFM measurement, electron leakage at the sample edges, a well-documented SEM imaging artifact, emphasized the edges, turning the edges into ‘ridges’ in the images and resulting in an inaccurate tip-sample convolution model.[179] We imaged the same region of the tissue with SNOM, AFM, and SEM. We then registered the AFM and SEM images to the SNOM images using our custom Matlab registration algorithm described previously (Figure 33).

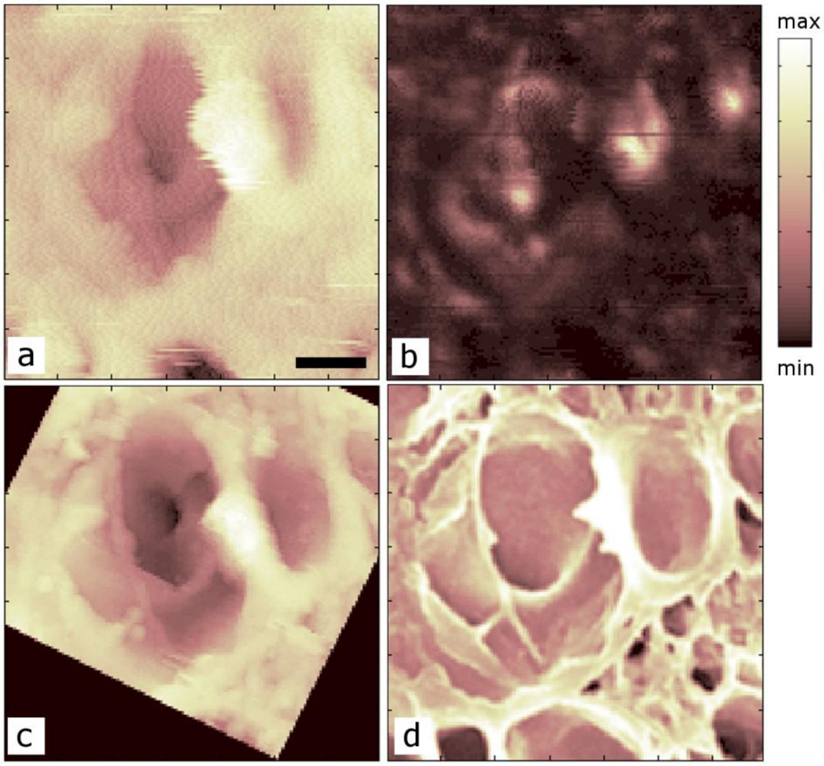

Figure 33 Simultaneous SNOM topography (a) and reflection (b) images of gold-palladium coated tissue. AFM topography measured by 50nm AFM tip (c) and SEM (d) images that have been registered to SNOM images. Scale bar, 1µm. Maximum height in the SNOM topography image is 3.67µm and maximum height in the AFM topography image is 2.5µm. The height difference is due to different zero-points.

The tip-sample convolution model and aperture-surface distance results were obtained from the AFM measured topography for a 20° SNOM probe and a vertical SNOM probe (Figure 34). The convolved surface obtained with the 20° SNOM probe (top row) does not vary much from the convolved surface obtained with the vertical SNOM probe (bottom row) except at the trailing edges of the registered image. Because of the abrupt and long drop from the AFM image to the flat background set at a height of 0, a very large aperture-surface distance is calculated at the trailing edge of the AFM image (618nm). However, within the AFM image, the maximum aperture-surface distance is 360nm. Therefore, the contrast of the calculated aperture-surface distance for the 20° probe (Figure 34c) was adjusted to 360nm at maximum for better comparison with the results from the vertical probe.

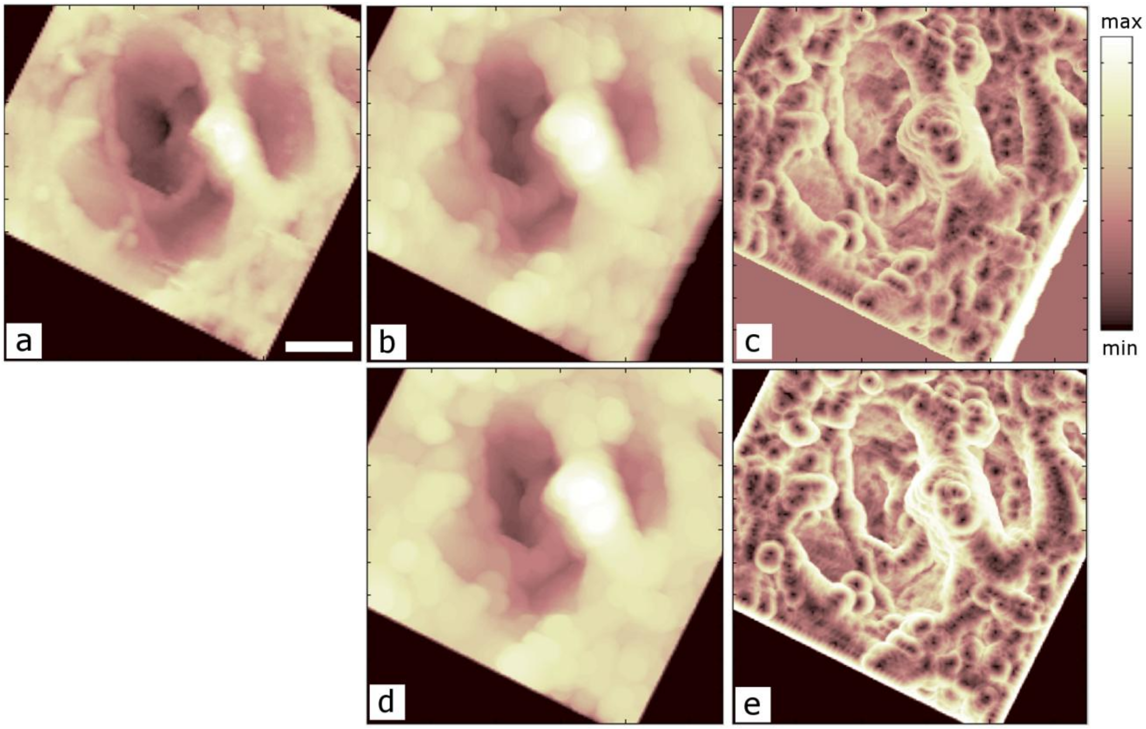

Figure 34 Convolution model results. Original AFM topography (a) and modeled SNOM tip path and resulting aperture-surface gap for a tip at 20° from vertical (b,c) and vertical tip (d,e). Scale bar, 1μm. Maximum height in the original and modeled topography images are all 2.5μm. Maximum aperture-surface distance for the 20° tip (c) is adjusted from the value for the trailing edge of the registered AFM image (618nm) to the maximum value within the AFM image (360nm). Maximum aperture-surface distance for the vertical tip (e) is 275nm.

To compare the results of our model to the measured reflection image, we zoom into a small region within the tissue exhibiting large topographic variations (Figure 35). Because the reflection image exhibits sharp intensity peaks, we have scaled it using Equation 52 to reduce the effect of the sharp peaks, allowing us to view all variations in the reflection signal (Figure 35f). Comparing the line profiles, we find that the peaks in the reflection signal correlate to regions where the slope of the SNOM probe is negative and the aperture-surface gap is large. Regions where the aperture-surface gap is large but the SNOM path slope is positive or zero do not show much variation in the reflection image. Therefore, we conclude that variation in aperture-surface gap isn't causing topographic artifacts alone but appears to explain artifacts when combined with the surface angle.

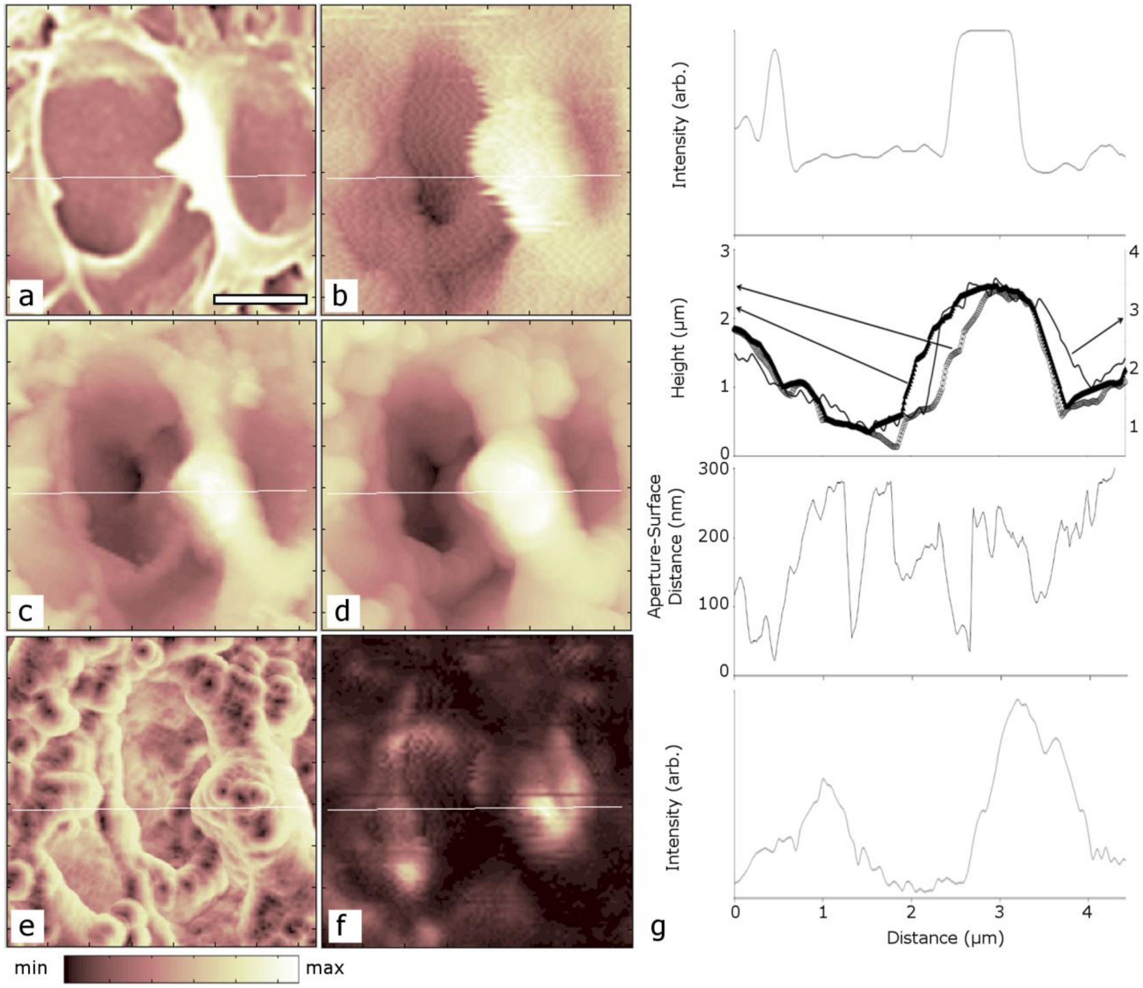

Figure 35 Convolution model results zoomed into a small region. SEM (a), SNOM measured topography (b), AFM measured topography (c), and modeled SNOM tip path (d). Calculated aperture-surface distance (e) and SNOM measured reflection (f). Scale bar, 2μm. Maximum height in the original and modeled topography images are all 2.5μm. Profiles along the white lines are shown in (g) in the same order as the images, with axes from top to bottom representing SEM, topography, aperture-surface distance, and SNOM reflection. In the topography height profiles, the thin black line represents the SNOM topography, the thick grey line represents the AFM topography, and the thick black line represents the model topography.

5.3.3 Discussion

In this work, we have described image formation in dual-optical SNOM imaging of tissue with a bent, angled SNOM probe as well as a horizontal probe. An angled probe offers the benefit of decreasing the impact of topographic artifacts and making artifacts easier to identify. We found that the topographical artifacts in the reflection signal for our angled tip are heavily dependent on surface angle and affected by the aperture-surface distance only on falling edges. Our qualitative analysis of the reflection SNOM image through joint analysis of the near-field reflection, near-field transmission, and topography images of human breast epithelial cells in the previous study found intensity peaks in the reflection SNOM image that correlate to falling slopes which were exponentially more intense than the peaks in the valleys. In that study, we attributed those peaks to topographic artifacts. This quantitative study confirms that those peaks were indeed artifacts. Through theoretical modeling and simulation, we have quantitatively described image formation in reflection SNOM imaging of tissue, which allows prediction and interpretation of artifacts in reflection SNOM imaging of thick biological samples, a necessary step for increasing the sensitivity of dual-optical SNOM imaging of tissue.

5.4 Conclusion

For this study, we built and characterized the performance of a custom dual-optical SNOM. This system uses a non-symmetric SNOM probe, which allows for axial reflection imaging and makes topographic artifacts easier to identify. Our dual-optical SNOM is customized to provide simultaneous reflection and transmission imaging, as well as mapping of the sample topography. Using our dual-optical SNOM, we imaged desiccated and non-desiccated human breast epithelial tissue. By comparing the simultaneous SNOM images, we isolated the influence of morphology and refractive index on scattering from the tissue and explained the cause of the change in scattering from tissue when it is dehydrated. Our results suggest that the reduction in back-scattering from tissue, relative to the glass slide, is caused by both dense packing of the scattering sites in the cytoplasm (morphology) in the desiccated tissue and a thin-film of water adhering to the glass slide (refractive index) in the non-desiccated tissue sample. Dual-optical SNOM imaging allowed us to prove this relationship using only one experimental setup while far-field optical studies would have required multiple experimental setups to separate the effect of morphology from the effect of the intrinsic optical properties of the sample. Additionally, dual-optical SNOM reduces the experimental variables in an experiment by measuring the reflection, transmission, and topography simultaneously, allowing more accurate interpretation of the results.

Because dual-optical SNOM is a novel technique, we investigated optical near-field image formation in dual-optical SNOM of tissue. Analyzing dual-optical SNOM images of the human epithelial breast tissue, we determined that, while some topographic artifacts are present in the reflection image, they do not dominate the SNOM images. We identified these artifacts and reduced their effect through an image transformation process. Additionally, we determined that the transmission SNOM images do not contain topographic artifacts, which is in agreement with our findings on SNOM imaging of cells. To better understand the effect of artifacts in reflection SNOM imaging, we utilized theoretical modeling and simulation to quantitatively describe image formation in reflection near-field SNOM imaging of tissue. Using our tip-sample convolution model and aperture-surface distance calculations, we determined that the topographical artifacts in the reflection signal for our angled tip are heavily dependent on surface angle and affected by the aperture-surface distance only on falling edges. The SNOM tip scanning simulation developed in this work is a powerful tool in reducing topographic artifacts in SNOM imaging of samples with large topographic variations. We can scan any sample with a sharp AFM tip and use our scanning simulation to determine the best SNOM tip configuration to use for smallest aperture-surface gap. Furthermore, we can determine whether variations in tip-surface distance cause topographic artifacts. This capability opens up the possibility for more sensitive SNOM measurements of tissue optical properties for future label-free tissue diagnostics applications.

In this work we have introduced a novel dual-optical SNOM for the investigation of the intrinsic optical properties of unlabeled tissue for label-free tissue diagnostics. This is the very first system where the near-field reflection and transmission images are recorded simultaneously and analyzed jointly to extract information about the optical properties of the sample. To enable accurate interpretation of the simultaneous transmission, reflection, and topographic images collected by our dual-optical SNOM, we described near-field image formation in SNOM imaging of tissue, both qualitatively through joint analysis of the images and quantitatively through modeling and theoretical analysis. We also demonstrated the potential of this dual-optical SNOM for studying the intrinsic optical properties of tissue and contributed valuable information about the intrinsic optical properties of tissue for label-free tissue diagnostics by revealing the cause of the change in scattering from tissue as it is dehydrated.

6 Conclusion

In this dissertation research, we have developed multi-scale optical metrology techniques that bridge the gap between nanotechnology and medicine and industry. We have demonstrated centimeter-scale metrology of CVD graphene for industry, nanoscale metrology of cells and nanoparticles, and nanoscale metrology of unlabeled tissue.

In our review of currently available graphene metrology techniques, we found that they all fall short of meeting the demands of industry. To increase the use of graphene in industry, high-throughput metrology techniques still needed to be developed. To fill this need, we developed a metrology technique based on FQM. Our studies on FQM of graphene found that graphene layers could be identified consistently through the fluorescence intensity of the dye-polymer layer. Each graphene layer quenches the dye fluorescence, leading to reduced fluorescence emission from the dye-polymer layer. We identified the quenching contrast ranges of 1, 2, and 3+ graphene layers and segmented the fluorescence image into graphene regions. Chemical doping decreases the quenching by graphene. Unlike graphene layers, doped graphene quenching contrast is not consistent. Instead, it varies depending on the doping efficacy. We developed and demonstrated a dynamic segmentation algorithm for identification of chemically-doped regions of single-layer graphene. Our graphene metrology technique allows quick and easy identification of graphene layers and chemical doping on arbitrary substrates and is the first reported high-throughput industrial metrology technique for graphene.

Our first application of SNOM for imaging biological samples was focused on cultured cells. First, we compared SNOM to far-field images of cells to demonstrate that we achieve accurate, high-resolution transmission imaging of these biological samples. In this study, we determine that topographic artifacts are not present in transmission SNOM images. Next, we identified iron oxide nanoparticles in the cells through their scattering behavior. We found that the scattering behavior of the iron oxide nanoparticles depends on the nanoparticle architecture and agglomeration. When the iron oxide nanoparticles were coated with dextran, they appeared brighter than the surrounding cell. However, when the iron oxide nanoparticles were unaltered, large agglomerations were formed in the cell, which were brighter than the cell at the edges and darker in the middle. This work introduces SNOM as a new technique for nanomedicine that allows detection of unlabeled nanoparticles within cells for feedback in the treatment nanoparticle development process.

For SNOM investigation of tissue, we developed a custom dual-optical SNOM, which collects topography, reflection, and transmission images simultaneously. This allows highly-correlated, rapid imaging of the tissue sample. In our dual-optical SNOM investigation of scattering from tissue, we determined that dense packing of the scatterers (e.g. mitochondria) in the cytoplasm is the cause of decreased scattering in desiccated tissue. We also studied topographic artifacts produced in dual-optical SNOM and found that, while topographic artifacts are present in the reflection SNOM image, they do not dominate the reflection signal and can be reduced by a simple signal processing step. To improve the accuracy of SNOM imaging of tissue, we developed a convolution model that allows prediction and explanation of topographic artifacts in the SNOM reflection image of tissue. Our work on SNOM imaging of tissue contributes to label-free tissue diagnostics by increasing the knowledge of optical properties of tissue and introducing dual-optical SNOM as a new technique for further study of the intrinsic optical properties of tissue.

This work facilitates the integration of nanotechnology with medicine and industry by enabling high-throughput metrology of graphene for industry, unlabeled nanoparticle detection in cells for nanomedicine, and high-resolution, sensitive, simultaneous topography and optical imaging to study intrinsic optical properties of tissue for label-free tissue diagnostics.

6.1 Future Prospects

The multi-scale optical metrology techniques developed in this dissertation research involve a combination of improvements in imaging methodologies and the incorporation of digital image processing techniques. We predict the future extension of this work will involve further advancement of these digital image processing procedures. Our studies on dual-optical SNOM demonstrated successful detection of useful information from the near-field images with a simple averaging algorithm. Therefore, we expect the sensitivity of this system and its usefulness in nanomedicine and label-free tissue diagnostics to benefit from advanced digital image processing techniques that analyze the SNOM reflection, transmission, and topography images simultaneously.

Through large-area montage image stitching, correction, and segmentation techniques, we augmented FQM with the ability to automatically and dynamically identify CVD graphene layer thickness and chemical doping. Some industrial applications may require additional information about the properties of graphene sheets. Therefore, incorporation of graphene in industry could be improved by the development of additional high-throughput metrology techniques. While a great deal of work has been put into developing graphene imaging methodologies, novel image processing has remained mostly unexplored even though image processing has already benefitted current graphene metrology techniques. Frequency filtering enhanced the atomic contrast of graphene in TEM[33,39] and STM[40] images and simulation allowed determination of density of states in STM images of graphene.[61] To aid in image processing of SPM images, an open-source software package was developed and is widely used.[194] There are many ways image processing can aid in the development of industrial graphene metrology techniques. The minimum contrast variation visible to the human eye is 1-2%,[195] approximately equal to the contrast between graphene layers on glass and copper substrates.[106,107] Therefore, optical reflection metrology on these substrates could be improved by employing image processing techniques to digitally enhance contrast. Furthermore, as industry acceptance of graphene becomes wider and graphene metrology is performed regularly, image processing techniques, such as the segmentation employed in our metrology technique, will become more important for automating these metrology techniques for production-line metrology of graphene. While our metrology technique employed contrast thresholding for segmentation, other metrology techniques could benefit from alternate segmentation techniques, such as boundary detection, region growing, and watershed identification.[195]

Bibliography

1. Betzig, E. & Trautman, J. K. Near-Field Optics: Microscopy, Spectroscopy, and Surface Modification Beyond the Diffraction Limit. *Science* **257**, 189–195 (1992).

2. Greffet, J. J. & Carminati, R. Image formation in near-field optics. *Prog. Surf. Sci.* **56**, 133–237 (1997).

3. Sauer, M. *Handbook of Fluorescence Spectroscopy and Imaging from Single Molecules to Ensembles*. (Wiley-VCH: Weinheim, Germany, 2011).

4. Lakowicz, J. R. *Principles of Fluorescence Spectroscopy*. (Springer: Boston, MA, 2006).

5. Turrell, G. & Corset, J. *Raman Microscopy: Developments and Applications*. (Academic Press: 1996).

6. Dexter, D. L. A theory of sensitized luminescence in solids. *J. Chem. Phys.* **21**, 836 (1953).

7. Robert M. Clegg Fluorescence Resonance Energy Transfer. *Fluorescence Imaging Spectroscopy and Microscopy* 179–252 (1996).

8. Jares-Erijman, E. A. & Jovin, T. M. FRET imaging. *Nat Biotech* **21**, 1387–1395 (2003).

9. Wang, X. F. & Herman, B. *Fluorescence Imaging Spectroscopy and Microscopy*. (Wiley-Interscience: New York, NY, 1996).

10. Velizhanin, K. A. & Efimov, A. Probing plasmons in graphene by resonance energy transfer. *Phys. Rev. B* **84**, 085401 (2011).

11. Swathi, R. S. & Sebastian, K. L. Resonance energy transfer from a dye molecule to graphene. *J. Chem. Phys.* **129**, 054703 (2008).

12. Swathi, R. S. & Sebastian, K. L. Long range resonance energy transfer from a dye molecule to graphene has (distance)(-4) dependence. *J. Chem. Phys.* **130**, 086101 (2009).

13. Velizhanin, K. A. & Efimov, A. Probing plasmons in graphene by resonance energy transfer. *Phys. Rev. B* **84**, 085401 (2011).

14. Swathi, R. S. & Sebastian, K. L. Distance dependence of fluorescence resonance energy transfer. *J. Chem. Sci.* **121**, 777–787 (2009).

15. Hernández-Martínez, P. L. & Govorov, A. O. Exciton energy transfer between nanoparticles and nanowires. *Phys. Rev. B* **78**, 035314 (2008).

16. Persson, B. N. J. & Lang, N. D. Electron-hole-pair quenching of excited states near a metal. *Phys. Rev. B* **26**, 5409–5415 (1982).

17. Synge, E. A suggested method for extending microscopic resolution into the ultra-microscopic region. *Philos. Mag.* **6**, 356–362 (1928).

18. Ash, E. A. & Nicholls, G. Super-resolution Aperture Scanning Microscope. *Nature* **237**, 510–512 (1972).

19. Lewis, A., Isaacson, M., Harootunian, A. & Muray, A. Development of a 500 Å spatial resolution light microscope: I. light is efficiently transmitted through [lambda]/16 diameter apertures. *Ultramicroscopy* **13**, 227–231 (1984).

20. Pohl, D. W., Denk, W. & Lanz, M. Optical stethoscopy: Image recording with resolution lambda/20. *Appl. Phys. Lett.* **44**, 651–653 (1984).

21. Novotny, L., Hecht, B. & Pohl, D. W. Implications of high resolution to near-field optical microscopy. *Ultramicroscopy* **71**, 341–344 (1998).

22. Cançado, L. G., Hartschuh, A. & Novotny, L. Tip-enhanced Raman spectroscopy of carbon nanotubes. *J. Raman Spectrosc.* **40**, 1420–1426 (2009).

23. Gucciardi, P. G. Applications of Scanning Near-Field Optical Microscopy in Life Science. *Applied Scanning Probe Methods XIII* 49–68 (2009).at <http://dx.doi.org/10.1007/978-3-540-85039-7_3>

24. Lide, D. R. *CRC Handbook of Chemistry and Physics*. (CRC Press: 2008).

25. Hecht, B. *et al.* Scanning near-field optical microscopy with aperture probes: Fundamentals and applications. *J. Chem. Phys.* **112**, 7761–7774 (2000).

26. Singh, V. *et al.* Graphene based materials: Past, present and future. *Prog. Mater. Sci.* **56**, 1178–1271 (2011).

27. Maynard, A. D. Don’t define nanomaterials. *Nature* **475**, 31 (2011).

28. Stamm, H. Risk factors: Nanomaterials should be defined. *Nature* **476**, 399 (2011).

29. Bae, S. *et al.* Roll-to-roll production of 30-inch graphene films for transparent electrodes. *Nat. Nanotechnol.* **5**, 574–578 (2010).

30. Dahmen, U. *et al.* Background, status and future of the Transmission Electron Aberration-corrected Microscope project. *Philos. T. Roy. Soc. A* **367**, 3795–3808

(2009).

31. Kisielowski, C. *et al.* Detection of single atoms and buried defects in three dimensions by aberration-corrected electron microscope with 0.5-\AA information limit. *Microsc. Microanal.* **14**, 469–477 (2008).

32. Meyer, J. C. *et al.* Direct Imaging of Lattice Atoms and Topological Defects in Graphene Membranes. *Nano Lett.* **8**, 3582–3586 (2008).

33. Gass, M. H. *et al.* Free-standing graphene at atomic resolution. *Nat. Nanotechnol.* **3**, 676–681 (2008).

34. Meyer, J. C. *et al.* The structure of suspended graphene sheets. *Nature* **446**, 60–63 (2007).

35. Gómez-Navarro, C. *et al.* Atomic Structure of Reduced Graphene Oxide. *Nano Lett.* **10**, 1144–1148 (2010).

36. Rasool, H. I. *et al.* Atomic-Scale Characterization of Graphene Grown on Copper (100) Single Crystals. *J. Am. Chem. Soc.* **133**, 12536–12543 (2011).

37. Girit, C. O. *et al.* Graphene at the Edge: Stability and Dynamics. *Science* **323**, 1705–1708 (2009).

38. Meyer, J. C., Girit, C. O., Crommie, M. F. & Zettl, A. Imaging and dynamics of light atoms and molecules on graphene. *Nature* **454**, 319–322 (2008).

39. Meyer, J. C. *et al.* Experimental analysis of charge redistribution due to chemical bonding by high-resolution transmission electron microscopy. *Nat. Mater.* **10**, 209–215 (2011).

40. Cao, H. L. *et al.* Large-scale graphitic thin films synthesized on Ni and transferred to insulators: Structural and electronic properties. *J. Appl. Phys.* **107**, 044310 (2010).

41. Colby, R. *et al.* Cross-sectional transmission electron microscopy of thin graphite films grown by chemical vapor deposition. *Diam. Relat. Mat.* **19**, 143–146 (2010).

42. Sutter, P., Sadowski, J. T. & Sutter, E. Graphene on Pt(111): Growth and substrate interaction. *Phys. Rev. B* **80**, 245411 (2009).

43. Li, X. *et al.* Large-Area Synthesis of High-Quality and Uniform Graphene Films on Copper Foils. *Science* **324**, 1312–1314 (2009).

44. Chen, S. *et al.* Synthesis and Characterization of Large-Area Graphene and Graphite Films on Commercial Cu–Ni Alloy Foils. *Nano Lett.* **11**, 3519–3525 (2011).

45. Li, X. *et al.* Transfer of Large-Area Graphene Films for High-Performance Transparent Conductive Electrodes. *Nano Lett.* **9**, 4359–4363 (2009).

46. Reina, A. *et al.* Growth of Large-Area Single- and Bi-Layer Graphene by Controlled Carbon Precipitation on Polycrystalline Ni Surfaces. *Nano Res.* **2**, 509–516 (2009).

47. Novoselov, K. S. *et al.* Electric field effect in atomically thin carbon films. *Science* **306**, 666–669 (2004).

48. Geim, A. K. & Novoselov, K. S. The rise of graphene. *Nat. Mater.* **6**, 183–191 (2007).

49. Novoselov, K. S. *et al.* Two-dimensional atomic crystals. *Proc. Natl. Acad. Sci. USA* **102**, 10451 (2005).

50. Reina, A. *et al.* Large Area, Few-Layer Graphene Films on Arbitrary Substrates by Chemical Vapor Deposition. *Nano Lett.* **9**, 30–35 (2009).

51. Paredes, J. I., Villar-Rodil, S., Solís-Fernández, P., Martínez-Alonso, A. & Tascón, J. M. D. Atomic Force and Scanning Tunneling Microscopy Imaging of Graphene Nanosheets Derived from Graphite Oxide. *Langmuir* **25**, 5957–5968 (2009).

52. Schniepp, H. C. *et al.* Functionalized Single Graphene Sheets Derived from Splitting Graphite Oxide. *J. Phys. Chem. B* **110**, 8535–8539 (2006).

53. Stankovich, S. *et al.* Synthesis of graphene-based nanosheets via chemical reduction of exfoliated graphite oxide. *Carbon* **45**, 1558–1565 (2007).

54. Binnig, G. & Rohrer, H. Scanning tunneling microscopy. *Surf. Sci.* **126**, 236–244 (1983).

55. Tersoff, J. & Hamann, D. R. Theory of the scanning tunneling microscope. *Phys. Rev. B* **31**, 805–813 (1985).

56. Stolyarova, E. *et al.* High-resolution scanning tunneling microscopy imaging of mesoscopic graphene sheets on an insulating surface. *Proc. Natl. Acad. Sci. USA* **104**, 9209 –9212 (2007).

57. Ishigami, M., Chen, J. H., Cullen, W. G., Fuhrer, M. S. & Williams, E. D. Atomic Structure of Graphene on SiO2. *Nano Lett.* **7**, 1643–1648 (2007).

58. Amara, H., Latil, S., Meunier, V., Lambin, P. & Charlier, J.-C. Scanning tunneling microscopy fingerprints of point defects in graphene: A theoretical prediction. *Phys. Rev. B* **76**, 155442 (2007).

59. Peres, N. M. R., Yang, L. & Tsai, S.-W. Local density of states and scanning tunneling currents in graphene. *New J. Phys.* **11**, 095007 (2009).

60. Saha, K., Paul, I. & Sengupta, K. Unconventional scanning tunneling conductance spectra for graphene. *Phys. Rev. B* **81**, 165446 (2010).

61. Cockayne, E. *et al.* Grain boundary loops in graphene. *Phys. Rev. B* **83**, 195425 (2011).

62. Zhao, L. *et al.* Visualizing individual nitrogen dopants in monolayer graphene. *Science* **333**, 999–1003 (2011).

63. Chen, X., Wan, H., Song, K., Tang, D. & Zhou, G. Scanning tunneling microscopy image modeling for zigzag-edge graphene nanoribbons. *Appl. Phys. Lett.* **98**, 263103 (2011).

64. Li, G., Luican, A. & Andrei, E. Y. Scanning Tunneling Spectroscopy of Graphene on Graphite. *Phys. Rev. Lett.* **102**, 176804 (2009).

65. Kobayashi, Y., Fukui, K., Enoki, T., Kusakabe, K. & Kaburagi, Y. Observation of zigzag and armchair edges of graphite using scanning tunneling microscopy and spectroscopy. *Phys. Rev. B* **71**, 193406 (2005).

66. Ferrari, A. C. *et al.* Raman Spectrum of Graphene and Graphene Layers. *Phys. Rev. Lett.* **97**, 187401 (2006).

67. Dresselhaus, M. S., Jorio, A., Hofmann, M., Dresselhaus, G. & Saito, R. Perspectives on Carbon Nanotubes and Graphene Raman Spectroscopy. *Nano Lett.* **10**, 751–758 (2010).

68. Ferralis, N. Probing mechanical properties of graphene with Raman spectroscopy. *J. Mater. Sci.* **45**, 5135–5149 (2010).

69. Ferrari, A. Raman spectroscopy of graphene and graphite: Disorder, electron–phonon coupling, doping and nonadiabatic effects. *Solid State Commun.* **143**, 47–57 (2007).

70. Malard, L. M., Pimenta, M. A., Dresselhaus, G. & Dresselhaus, M. S. Raman spectroscopy in graphene. *Phys. Rep.* **473**, 51–87 (2009).

71. Rao, C. N. R., Sood, A. K., Subrahmanyam, K. S. & Govindaraj, A. Graphene: The New Two-Dimensional Nanomaterial. *Angew. Chem. Int. Edit.* **48**, 7752–7777 (2009).

72. Saito, R., Hofmann, M., Dresselhaus, G., Jorio, A. & Dresselhaus, M. S. Raman spectroscopy of graphene and carbon nanotubes. *Adv. Phys.* **60**, 413–550 (2011).

73. Basko, D. M., Piscanec, S. & Ferrari, A. C. Electron-electron interactions and doping dependence of the two-phonon Raman intensity in graphene. *Phys. Rev. B* **80**, 165413 (2009).

74. Casiraghi, C., Pisana, S., Novoselov, K. S., Geim, A. K. & Ferrari, A. C. Raman fingerprint of charged impurities in graphene. *Appl. Phys. Lett.* **91**, 233108 (2007).

75. Das, A. *et al.* Monitoring dopants by Raman scattering in an electrochemically top-gated graphene transistor. *Nat. Nanotechnol.* **3**, 210–215 (2008).

76. Yan, J., Zhang, Y., Kim, P. & Pinczuk, A. Electric Field Effect Tuning of Electron-Phonon Coupling in Graphene. *Phys. Rev. Lett.* **98**, 166802 (2007).

77. Casiraghi, C. *et al.* Raman Spectroscopy of Graphene Edges. *Nano Lett.* **9**, 1433–1441 (2009).

78. You, Y., Ni, Z., Yu, T. & Shen, Z. Edge chirality determination of graphene by Raman spectroscopy. *Appl. Phys. Lett.* **93**, 163112 (2008).

79. Calizo, I., Bao, W. Z., Miao, F., Lau, C. N. & Balandin, A. A. The effect of substrates on the Raman spectrum of graphene: Graphene-on-sapphire and graphene-on-glass. *Appl. Phys. Lett.* **91**, 201904 (2007).

80. Graf, D. *et al.* Spatially Resolved Raman Spectroscopy of Single- and Few-Layer Graphene. *Nano Lett.* **7**, 238–242 (2007).

81. Gupta, A., Chen, G., Joshi, P., Tadigadapa, S. & Eklund, P. C. Raman scattering from high-frequency phonons in supported n-graphene layer films. *Nano Lett.* **6**, 2667–2673 (2006).

82. Ni, Z. H. *et al.* Graphene Thickness Determination Using Reflection and Contrast Spectroscopy. *Nano Lett.* **7**, 2758–2763 (2007).

83. Park, J. S. *et al.* G′G′ band Raman spectra of single, double and triple layer graphene. *Carbon* **47**, 1303–1310 (2009).

84. Cancado, L. G. *et al.* Quantifying defects in graphene via Raman spectroscopy at different excitation energies. *Nano Lett.* **11**, 3190–3196 (2011).

85. Guermoune, A. *et al.* Chemical vapor deposition synthesis of graphene on copper with methanol, ethanol, and propanol precursors. *Carbon* **49**, 4204–4210 (2011).

86. Jorio, A. *et al.* Raman study of ion-induced defects in N-layer graphene. *J. Phys.-Condens. Mat.* **22**, 334204 (2010).

87. Lucchese, M. M. *et al.* Quantifying ion-induced defects and Raman relaxation

length in graphene. *Carbon* **48**, 1592–1597 (2010).

88. Balandin, A. A. *et al.* Superior thermal conductivity of single-layer graphene. *Nano Lett.* **8**, 902–907 (2008).

89. Ghosh, S. *et al.* Extremely high thermal conductivity of graphene: Prospects for thermal management applications in nanoelectronic circuits. *Appl. Phys. Lett.* **92**, 151911 (2008).

90. Jung, N., Crowther, A. C., Kim, N., Kim, P. & Brus, L. Raman Enhancement on Graphene: Adsorbed and Intercalated Molecular Species. *ACS Nano* **4**, 7005–7013 (2010).

91. Calizo, I. *et al.* Raman nanometrology of graphene: Temperature and substrate effects. *Solid State Commun.* **149**, 1132–1135 (2009).

92. Wang, Y. Y. *et al.* Raman studies of monolayer graphene: The substrate effect. *J. Phys. Chem. C* **112**, 10637–10640 (2008).

93. Dong, X. *et al.* Growth of large-sized graphene thin-films by liquid precursor-based chemical vapor deposition under atmospheric pressure. *Carbon* **49**, 3672–3678 (2011).

94. Yu, Q. *et al.* Control and characterization of individual grains and grain boundaries in graphene grown by chemical vapour deposition. *Nat. Mater.* **10**, 443–449 (2011).

95. Ohta, T., Bostwick, A., Seyller, T., Horn, K. & Rotenberg, E. Controlling the Electronic Structure of Bilayer Graphene. *Science* **313**, 951 –954 (2006).

96. Robinson, J. T. *et al.* Properties of Fluorinated Graphene Films. *Nano Lett.* **10**, 3001–3005 (2010).

97. Dreyer, D. R., Park, S., Bielawski, C. W. & Ruoff, R. S. The chemistry of graphene oxide. *Chem. Soc. Rev.* **39**, 228–240 (2009).

98. Park, S. *et al.* Aqueous Suspension and Characterization of Chemically Modified Graphene Sheets. *Chem. Mater.* **20**, 6592–6594 (2008).

99. Roddaro, S., Pingue, P., Piazza, V., Pellegrini, V. & Beltram, F. The Optical Visibility of Graphene: Interference Colors of Ultrathin Graphite on SiO2. *Nano Lett.* **7**, 2707–2710 (2007).

100. Nolen, C. M., Denina, G., Teweldebrhan, D., Bhanu, B. & Balandin, A. A. High-Throughput Large-Area Automated Identification and Quality Control of Graphene and Few-Layer Graphene Films. *ACS Nano* **5**, 914–922 (2011).

101. Casiraghi, C. *et al.* Rayleigh Imaging of Graphene and Graphene Layers. *Nano Lett.* **7**, 2711–2717 (2007).

102. Blake, P. *et al.* Making graphene visible. *Appl. Phys. Lett.* **91**, 063124 (2007).

103. Wang, X. F., Zhao, M. & Nolte, D. D. Optical contrast and clarity of graphene on an arbitrary substrate. *Appl. Phys. Lett.* **95**, 081102 (2009).

104. De Marco, P. *et al.* Rapid identification of graphene flakes: alumina does it better. *Nanotechnol.* **21**, 255703 (2010).

105. Jung, I. *et al.* Simple Approach for High-Contrast Optical Imaging and Characterization of Graphene-Based Sheets. *Nano Lett.* **7**, 3569–3575 (2007).

106. Gaskell, P. E., Skulason, H. S., Rodenchuk, C. & Szkopek, T. Counting graphene layers on glass via optical reflection microscopy. *Appl. Phys. Lett.* **94**, 143101 (2009).

107. Kaplas, T., Zolotukhin, A. & Svirko, Y. Thickness determination of graphene on metal substrate by reflection spectroscopy. *Opt. Express* **19**, 17226–17231 (2011).

108. Treossi, E. *et al.* High-Contrast Visualization of Graphene Oxide on Dye-Sensitized Glass, Quartz, and Silicon by Fluorescence Quenching. *J. Am. Chem. Soc.* **131**, 15576–15577 (2009).

109. Kim, J., Cote, L. J., Kim, F. & Huang, J. X. Visualizing Graphene Based Sheets by Fluorescence Quenching Microscopy. *J. Am. Chem. Soc.* **132**, 260–267 (2010).

110. Kim, J., Kim, F. & Huang, J. X. Seeing graphene-based sheets. *Mat. Today* **13**, 28–38 (2010).

111. Kyle, J. R. *et al.* Centimeter-Scale High-Resolution Metrology of Entire CVD-Grown Graphene Sheets. *Small* **7**, 2599–2606 (2011).

112. Liu, Y., Liu, C. Y. & Liu, Y. Investigation on fluorescence quenching of dyes by graphite oxide and graphene. *Appl. Surf. Sci.* **257**, 5513–5518 (2011).

113. Ramakrishna Matte, H. S. S., Subrahmanyam, K. S., Venkata Rao, K., George, S. J. & Rao, C. N. R. Quenching of fluorescence of aromatic molecules by graphene due to electron transfer. *Chem. Phys. Lett.* **506**, 260–264 (2011).

114. Velizhanin, K. A. & Efimov, A. Probing plasmons in graphene by resonance energy transfer. *Phys. Rev. B* **84**, 085401 (2011).

115. Wang, Y., Li, Z., Wang, J., Li, J. & Lin, Y. Graphene and graphene oxide: biofunctionalization and applications in biotechnology. *Trends Biotechnol.* **29**, 205–

212 (2011).

116. Zhang, M., Yin, B.-C., Tan, W. & Ye, B.-C. A versatile graphene-based fluorescence 'on/off' switch for multiplex detection of various targets. *Biosens. Bioelectron.* **26**, 3260–3265 (2011).

117. He, S. *et al.* A Graphene Nanoprobe for Rapid, Sensitive, and Multicolor Fluorescent DNA Analysis. *Adv. Funct. Mater.* **20**, 453–459 (2010).

118. Liu, M. *et al.* A 'turn-on' fluorescent copper biosensor based on DNA cleavage-dependent graphene-quenched DNAzyme. *Biosens. Bioelectron.* **26**, 4111–4116 (2011).

119. Wu, C., Zhou, Y., Miao, X. & Ling, L. A novel fluorescent biosensor for sequence-specific recognition of double-stranded DNA with the platform of graphene oxide. *Analyst* **136**, 2106–2110 (2011).

120. Chang, H., Tang, L., Wang, Y., Jiang, J. & Li, J. Graphene Fluorescence Resonance Energy Transfer Aptasensor for the Thrombin Detection. *Anal. Chem.* **82**, 2341–2346 (2010).

121. Chen, Q., Wei, W. & Lin, J.-M. Homogeneous detection of concanavalin A using pyrene-conjugated maltose assembled graphene based on fluorescence resonance energy transfer. *Biosens. Bioelectron.* **26**, 4497–4502 (2011).

122. Liu, M., Zhao, H., Quan, X., Chen, S. & Fan, X. Distance-independent quenching of quantum dots by nanoscale-graphene in self-assembled sandwich immunoassay. *Chem. Commun.* **46**, 7909–7911 (2010).

123. Cai, L. *et al.* Butterfly-Shaped Conjugated Oligoelectrolyte/Graphene Oxide Integrated Assay for Light-Up Visual Detection of Heparin. *Anal. Chem.* **83**, 7849–7855 (2011).

124. Chen, J.-L., Yan, X.-P., Meng, K. & Wang, S.-F. Graphene Oxide Based Photoinduced Charge Transfer Label-Free Near-Infrared Fluorescent Biosensor for Dopamine. *Anal. Chem.* **83**, 8787–8793 (2011).

125. Feng, D. *et al.* A graphene oxide–peptide fluorescence sensor tailor-made for simple and sensitive detection of matrix metalloproteinase 2. *Chem. Commun.* **47**, 10680–10682 (2011).

126. Liu, Y., Yu, D., Zeng, C., Miao, Z. & Dai, L. Biocompatible Graphene Oxide-Based Glucose Biosensors. *Langmuir* **26**, 6158–6160 (2010).

127. Chen, Z., Berciaud, S., Nuckolls, C., Heinz, T. F. & Brus, L. E. Energy Transfer

from Individual Semiconductor Nanocrystals to Graphene. *ACS Nano* **4**, 2964–2968 (2010).

128. Klekachev, A. V. *et al.* Electron accumulation in graphene by interaction with optically excited quantum dots. *Physica E* **43**, 1046–1049 (2011).

129. Zedan, A. F., Sappal, S., Moussa, S. & El-Shall, M. S. Ligand-Controlled Microwave Synthesis of Cubic and Hexagonal CdSe Nanocrystals Supported on Graphene. Photoluminescence Quenching by Graphene. *J. Phys. Chem. C* **114**, 19920–19927 (2010).

130. Wojcik, A. & Kamat, P. V. Reduced Graphene Oxide and Porphyrin. An Interactive Affair in 2-D. *ACS Nano* **4**, 6697–6706 (2010).

131. Zhang, X.-F. & Xi, Q. A graphene sheet as an efficient electron acceptor and conductor for photoinduced charge separation. *Carbon* **49**, 3842–3850 (2011).

132. Xie, L. M., Ling, X., Fang, Y., Zhang, J. & Liu, Z. F. Graphene as a Substrate To Suppress Fluorescence in Resonance Raman Spectroscopy. *J. Am. Chem. Soc.* **131**, 9890–9891 (2009).

133. Hall, D. B., Underhill, P. & Torkelson, J. M. Spin coating of thin and ultrathin polymer films. *Polym. Eng. Sci.* **38**, 2039–2045 (1998).

134. Mohajerani, E., Farajollahi, F., Mahzoon, R. & Baghery, S. Morphological and thickness analysis for PMMA spin coated films. *J. Optoelectron. Adv. M.* **9**, 3901 (2007).

135. Walsh, C. B. & Franses, E. I. Ultrathin PMMA films spin-coated from toluene solutions. *Thin Solid Films* **429**, 71–76 (2003).

136. Fan, J. *et al.* Investigation of the influence on graphene by using electron-beam and photo-lithography. *Solid State Commun.* **151**, 1574–1578 (2011).

137. Obraztsov, A. N. Chemical vapour deposition: Making graphene on a large scale. *Nat. Nanotechnol.* **4**, 212–213 (2009).

138. Allen, M., Tung, V. & Kaner, R. Honeycomb Carbon: A Review of Graphene. *Chem. Rev.* **110**, 132–145 (2010).

139. Chen, Z., Lin, Y., Rooks, M. & Avouris, P. Graphene nano-ribbon electronics. *Physica E* **40**, 228–232 (2007).

140. Lin, J. *et al.* Gating of Single-Layer Graphene with Single-Stranded Deoxyribonucleic Acids. *Small* **6**, 1150–1155 (2010).

141. Wang, X. R. *et al.* Room-temperature all-semiconducting sub-10-nm graphene nanoribbon field-effect transistors. *Phys. Rev. Lett.* **100**, (2008).

142. De Arco, L. G. *et al.* Continuous, Highly Flexible, and Transparent Graphene Films by Chemical Vapor Deposition for Organic Photovoltaics. *ACS Nano* **4**, 2865–2873 (2010).

143. Lin, J. *et al.* Heterogeneous Graphene Nanostructures: ZnO Nanostructures Grown on Large-Area Graphene Layers. *Small* **6**, 2448–2452 (2010).

144. Paul, R. *et al.* Synthesis of a Pillared Graphene Nanostructure: A Counterpart of Three-Dimensional Carbon Architectures. *Small* **6**, 2309–2313 (2010).

145. Reina, A. *et al.* Transferring and Identification of Single- and Few-Layer Graphene on Arbitrary Substrates. *J. Phys. Chem. C* **112**, 17741–17744 (2008).

146. Li, H., Zhu, Z., Liu, J., Xie, S. & Li, H. Hollow palladium–cobalt bimetallic nanospheres as an efficient and reusable catalyst for Sonogashira-type reactions. *J. Mater. Chem.* **20**, 4366–4370 (2010).

147. Robinson, J. T. *et al.* Properties of Fluorinated Graphene Films. *Nano Lett.* **10**, 3001–3005 (2010).

148. Guo, S. *et al.* Tuning of Electron Transport in Graphene based Field Effect Devices using Block Co-polymers. *Small* (2012).doi:10.1002/small.201002016

149. Lagarias, J. C., Reeds, J. A., Wright, M. H. & Wright, P. E. Convergence properties of the Nelder-Mead simplex method in low dimensions. *SIAM J. Optim.* **9**, 112–147 (1998).

150. Nelder, J. A. & Mead, R. A simplex method for function minimization. *Comput. J.* **7**, 308–313 (1965).

151. Bondarev, S. L., Knyukshto, V. N., Stepuro, V. I., Stupak, A. P. & Turban, A. A. Fluorescence and Electronic Structure of the Laser Dye DCM in Solutions and in Polymethylmethacrylate. *J. Appl. Spectrosc.* **71**, 194–201 (2004).

152. Arruebo, M., Fernández-Pacheco, R., Ibarra, M. R. & Santamaría, J. Magnetic nanoparticles for drug delivery. *Nano Today* **2**, 22–32 (2007).

153. de Lange, F. *et al.* Cell biology beyond the diffraction limit: near-field scanning optical microscopy. *J. Cell Sci.* **114**, 4153–4160 (2001).

154. Longo, G., Girasole, M. & Cricenti, A. Implementation of a bimorph-based aperture tapping-SNOM with an incubator to study the evolution of cultured living cells. *J. Microsc. (Oxf)* **229**, 433–439 (2008).

155. García-Parajó, M. F. *et al.* Near-Field Fluorescence Microscopy An Optical Nanotool to Study Protein Organization at the Cell Membrane. *NanoBiotechnol.* **1**, 113–120 (2005).

156. Hoppener, C., Siebrasse, J., Peters, R., Kubitscheck, U. & Naber, A. High-resolution near-field optical imaging of single nuclear pore complexes under physiological conditions. *Biophys. J.* **88**, 3681–3688 (2005).

157. Betzig, E. & Chichester, R. J. Single Molecules Observed by Near-Field Scanning Optical Microscopy. *Science* **262**, 1422–1425 (1993).

158. Zhang, Y. *et al.* A Surface-Charge Study on Cellular-Uptake Behavior of F3-Peptide-Conjugated Iron Oxide Nanoparticles. *Small* **5**, 1990–1996 (2009).

159. Zhang, Y. *et al.* Zeta potential: a surface electrical characteristic to probe the interaction of nanoparticles with normal and cancer human breast epithelial cells. *Biomedical Microdevices* **10**, 321–328 (2007).

160. Horcas, I. *et al.* WSXM: A software for scanning probe microscopy and a tool for nanotechnology. *Rev. Sci. Instrum.* **78**, 013705-013705-8 (2007).

161. de Paula, A. M., Chaves, C. R., Silva, H. B. & Weber, G. Absorption Coefficient Imaging by Near-Field Scanning Optical Microscopy in Bacteria. *Appl. Opt.* **42**, 3005–3008 (2003).

162. Salazar-Alvarez, G. *et al.* Synthesis and nonlinear light scattering of microemulsions and nanoparticle suspensions. *J. Nanopart. Res.* **9**, 647–652 (2007).

163. Walls, J. *et al.* Can Preoperative Factors Predict for Residual Malignancy After Breast Biopsy for Invasive Cancer. *Ann. Roy. Coll. Surg.* **77**, 248–251 (1995).

164. Cabioglu, N. *et al.* Role for intraoperative margin assessment in patients undergoing breast-conserving surgery. *Ann. Surg. Oncol.* **14**, 1458–1471 (2007).

165. The Innovator, Summer 2008... The Volatile hematoxylin Market. (2008).at <http://www.anatechltdusa.com/Innovators/InnList.html>

166. Demos, S., Vogel, A. & Gandjbakhche, A. Advances in optical spectroscopy and imaging of breast lesions. *J. Mammary Gland Biol.* **11**, 165–181 (2006).

167. Monici, M. Cell and tissue autofluorescence research and diagnostic applications. *Biotechnol. Annu. Rev.* **11**, 227–256 (2005).

168. Dunn, A. & Richards-Kortum, R. Three-dimensional computation of light scattering from cells. *IEEE J. Sel. Top. Quant.* **2**, 898–905 (1996).

169. Tanev, S., Tuchin, V. & Paddon, P. Light scattering effects of gold nanoparticles in cells: FDTD modeling. *Laser Phys. Lett.* **3**, 594–598 (2006).

170. Tanev, S., Tuchin, V. & Paddon, P. Cell membrane and gold nanoparticles effects on optical immersion experiments with noncancerous and cancerous cells: finite-difference time-domain modeling. *J. Biomed. Opt.* **11**, 064037 (2006).

171. Mourant, J. *et al.* Mechanisms of light scattering from biological cells relevant to noninvasive optical-tissue diagnostics. *Appl. Opt.* **37**, 3586–3593 (1998).

172. Beuthan, J., Minet, O., Helfmann, J., Herrig, M. & Müller, G. The spatial variation of the refractive index in biological cells. *Phys. Med. Biol.* **41**, 369–382 (1996).

173. Drezek, R. *et al.* Light scattering from cervical cells throughout neoplastic progression: influence of nuclear morphology, DNA content, and chromatin texture. *J. Biomed. Opt.* **8**, 7–16 (2003).

174. Liang, X. J., Liu, A. Q., Lim, C. S., Ayi, T. C. & Yap, P. H. Determining refractive index of single living cell using an integrated microchip. *Sens. Actuators A Phys.* **133**, 349–354 (2007).

175. Mourant, J. *et al.* Light scattering from cells: the contribution of the nucleus and the effects of proliferative status. *J. Biomed. Opt.* **5**, 131–137 (2000).

176. Tang, S., Sun, C. H., Krasieva, T., Chen, Z. & Tromberg, B. Imaging subcellular scattering contrast by using combined optical coherence and multiphoton microscopy. *Opt. Lett.* **32**, 503–505 (2007).

177. Lu, J. Q., Hu, X. H. & Dong, K. Modeling of the rough-interface effect on a converging light beam propagating in a skin tissue phantom. *Appl. Opt.* **39**, 5890–5897 (2000).

178. Ma, X. Y., Lu, J. Q. & Hu, X. H. Effect of surface roughness on determination of bulk tissue optical parameters. *Opt. Lett.* **28**, 2204–2206 (2003).

179. Castle, J. & Zhdan, P. Characterization of surface topography by SEM and SFM: Problems and solutions. *J. Phys. D Appl. Phys.* **30**, 722–740 (1997).

180. Edidin, M. Near-field scanning optical microscopy, a siren call to biology. *Traffic* **2**, 797–803 (2001).

181. Jahncke, C. & Hallen, H. A versatile stable scanning proximal probe microscope. *Rev. Sci. Instrum.* **68**, 1759–1763 (1997).

182. Stranick, S., Richter, L. & Cavanagh, R. High efficiency, dual collection made near-field scanning optical microscope. *J. Vac. Sci. Technol. B* **16**, 1948–1952 (1998).

183. Wei, P. K., Hsu, J. H., Fann, W. S. & Tsai, K. T. Dual-optical-mode near-field scanning optical microscopy. *Appl. Opt.* **35**, 6727–6731 (1996).

184. Kim, J., Drachev, V., Yuan, H., Bakker, R. & Shalaev, V. Imaging contrast under aperture tip-nanoantenna array interaction. *Appl. Phys. B-Lasers O.* **93**, 189–198 (2008).

185. Simpson, S. H. & Hanna, S. Scanning near-field optical microscopy of metallic features. *Opt. Commun.* **256**, 476–488 (2005).

186. Brunsting, A. & Mullaney, P. Differential Light-Scattering from Spherical Mammalian-Cells. *Biophys. J.* **14**, 439–453 (1974).

187. Maier, J., Walker, S., Fantini, S., Franceschini, M. & Gratton, E. Possible Correlation Between Blood-Glucose Concentration and the Reduced Scattering Coefficient of Tissues in the Near-Infrared. *Opt. Lett.* **19**, 2062–2064 (1994).

188. Keller, D. & Franke, F. Envelope Reconstruction of Probe Microscope Images. *Surf. Sci.* **294**, 409–419 (1993).

189. Hecht, B., Bielefeldt, H., Inouye, Y., Pohl, D. & Novotny, L. Facts and artifacts in near-field optical microscopy. *J. Appl. Phys.* **81**, 2492–2498 (1997).

190. Bozhevolnyi, S. I. Topographical artifacts and optical resolution in near-field optical microscopy. *J. Opt. Soc. Am. B* **14**, 2254–2259 (1997).

191. Klapetek, P., Valtr, M., Klenovsky, P. & Bursik, J. Characterization of near-field optical microscope probes. *Surf. Interface Anal.* **40**, 482–485 (2008).

192. Tuchin, V. V. *Optical clearing of tissues and blood*. (SPIE Press: 2006).

193. Rylander, C. *et al.* Dehydration mechanism of optical clearing in tissue. *J. Biomed. Opt.* **11**, 041117 (2006).

194. Horcas, I. *et al.* WSXM: A software for scanning probe microscopy and a tool for nanotechnology. *Rev. Sci. Instrum.* **78**, 013705 (2007).

195. Gonzalez, R. C. & Woods, R. E. *Digital image processing*. (Prentice Hall: 2002).